THE MILKY WAY'S MOST LUMINOUS STAR CLUSTERS:
ENGINES OF GALAXY EVOLUTION

by

Mubdi Muhammad Rahman

A thesis submitted in conformity with the requirements
for the degree of Doctor of Philosophy
Graduate Department of Astronomy & Astrophysics
University of Toronto

Abstract

The Milky Way's Most Luminous Star Clusters:

Engines of Galaxy Evolution

Mubdi Muhammad Rahman

Doctor of Philosophy

Graduate Department of Astronomy & Astrophysics

University of Toronto

2012

Massive young star clusters and OB associations ($M > 10^4$ $M_\odot$) dominate the energetic feedback from stars into the interstellar medium. They contain the most massive and luminous stars in the Galaxy, which shape their environments through winds, ionizing flux, radiation pressure, and eventually supernovae, destroying their natal molecular clouds and inflating superbubbles. Few such clusters have been identified in our Galaxy. We systematically investigate the most luminous H II regions, which we identify using the WMAP foreground maps. We find that the 13 most luminous sources produce one-third of the Galaxy's total ionizing luminosity, all with expected powering populations of $M > 4 \times 10^4$ $M_\odot$. These populations are grouped in small numbers of clusters or associations for each WMAP source. The emission from these regions is dominated by the diffuse component at large radii ($\sim$10-70 pc) indicating a high leaking fraction of ionizing photons. Using 8 μm maps from Spitzer GLIMPSE and published radio recombination line observations, we resolve the large ($> 1°$) WMAP sources into 40 star forming complexes (SFCs) exhibiting shell morphology with evidence of expansion due to a central powering source. We develop a method, based on differential extinction of the galactic disk, to identify the SFC's powering cluster candidates with 2MASS. We identify 22 cluster candidates within the 40 SFCs having extinctions consistent with their distances. With near-infrared spectroscopy

from the New Technology Telescope, we have confirmed the existence of the most massive of these associations, the Dragonfish Association, with $M = 10^5$ $M_\odot$. Of the 50 sampled stars, we identify 2 Luminous Blue Variable candidates, a Wolf-Rayet, and 15 O-type stars, consistent with the yield expected from the candidate contamination rate, verifying the candidate cluster identification method. This investigation doubles the number of massive young star clusters and OB associations known and produces the most complete picture of the upper end of the Galaxy's cluster mass function to date.

"And it is He who placed for you the stars that you may be guided by them through the darknesses of the land and sea. We have detailed the signs for a people who know."

-Al Qur'an, Sura Al-'An'am, Verse 96

(Sahih International Translation)

Acknowledgements

In the name of God; The Most Gracious, the Most Merciful.

To my supervisors, Chris Matzner and Dae-Sik Moon. The both of you have challenged, encouraged, and supported me throughout this process, taking a risk on this student with a crazy idea and helping see it to fruition. For this, I am deeply indebted to the both of you. I hope that one day I will have the opportunity to instill my future students with even a small fraction of what the both of you have taught me.

To Norm Murray and Peter Martin, who have been more than simply committee members to me, but mentors in the truest sense. Beyond an appreciation of the both of you as great scientists, I have an incredible admiration for the both of you as people. Thank you for providing footsteps for me to follow in.

To my mentor, Rosemary McNaughton, whose guidance and inspiration gave me the confidence and direction to chase this dream.

To the many faculty and staff in the department and throughout the University who have helped me along the way, including James Graham, Jonathan Dursi, Jonathan Sievers, Jerry Mitrovica, Stephen Morris, Mike Reid, Chris Loken, Lee Robbins, Stefan Mochnacki, John Percy, Ernie Seaquist, Slavek Rucinski, and Ue-Li Pen.

To my friends and colleagues in the Department, who have been my family throughout this adventure, challenging, encourgaging, and inspiring me on this path, including Jamil Shariff, Ilana MacDonald, Greg Paciga, Gojko Vujanovic, Sherry Yeh, Kaitlin Kratter, Rodrigo Fernandez, Richard Chou, René Breton, Anne-Marie Weijmans, Koraljka Muzic, Mariangela Bonavita, Mike Williams, and Snezana Prodan.

To Reni Barlow and Youth Science Canada, who've given me the venue and support to inspire future generations of scientists as they chase their dreams.

To my students throughout the years, for constantly reminding me of why I became an astronomer. A special thanks to those students I have had the privilege

of supervising: Brent Arsenault, Heidi White and Eve Lee, may you be successful in whatever path you choose.

To my many teachers along the way, who have nurtured my thirst for knowledge and my passion for attaining it.

To the many good friends who've supported me, given me a shoulder to lean on, and believed in my dream even when I was on the verge of losing hope, including Daniel Faber, Carmen Marra, Dan Weaver, Beryl Strawczynski, Kerry Scott, Ahmed Ogunsola, Faraz Siddiqui, Tahbit Chowdhury, Sarah Ingimundson, Alison Davidson, Caroline Whippey, Kartik Madiraju, Anila Madiraju, Shobhit Shanker, Sura Abdul-Razzak, Renee Willmon, Aisha Ahmad, Elena Tsimakouridze, and Alana Harrison.

To Crystal Brasseur, whose memory will always inspire me to follow my passion.

To my sisters, Mahfuza, Deenah and Lina for their continual support and the pride they've had in their little brother who's always had his head in the stars. Finally, I would like to thank my parents; from an early age, they instilled me with the lessons of hard work, perseverance, humility, and quiet confidence that remain with me to this day. Thank you for raising a dreamer of a son and giving him the skills to make them come true.

Contents

List of Tables

List of Figures

Chapter 1

Introduction

Star clusters and associations have long been astronomical "Rosetta Stones": from their initial discovery to the present, clustered groups of stars have served both as landmarks of the structure of the Universe and laboratories for a variety of astrophysical phenomena. From helping us determine the shape and size of the Galaxy to unveiling the details of stellar evolution, star clusters and associations have marked contributions to nearly all fields within astronomy.

In this thesis, we search for the most luminous star clusters and OB associations in the Galaxy. We use radio and infrared observations to identify the locations of the most luminous clusters based on their reprocessed emission and the morphology of their surrounding medium. We then develop a technique to identify candidate clusters and associations in the identified fields, using the method to identify the most luminous OB association in the Galaxy. We use spectroscopic techniques to confirm the existence of the identified association. We then apply the developed technique to all the remaining regions within the original study to double the number of massive, young clusters and OB associations identified in the Milky Way.

In this introductory chapter, we briefly outline the history of stellar cluster and OB association observations in the Galaxy. We then motivate the search for massive clusters and associations both as laboratories of star formation and of feedback into

their surrounding environments.

1.1   Star Clusters & Associations in the Galaxy

1.1.1   Historical Observations

While numerous stellar clusters have been observed as cloudy *nebulae* since Antiquity, Galilei (1610) was the first to use a telescope to resolve many of these groups into their constituent stars. The first discoveries of new star clusters previously unseen by the naked eye were recorded by Hodierna (1656), who was able to resolve M47 and M41 into individual stars with the aid of a telescope (Fodera-Serio et al. 1985). The next few centuries saw the work of Messier (1771) and Herschel (1786) catalog hundreds of new star clusters. Herschel's work made the early morphological distinction between the circular, dense globular clusters and the irregular, sparse open clusters, the former being recognized as older populations. Michell (1767) was the first to infer physical association of the stars in a cluster based on statistical arguments. While the open clusters were inferred to be gravitationally bound, unbound stellar associations were discovered by Ambartsumian (1947), providing the first evidence of ongoing star formation in the Galaxy (Ambartsumian 1954). Further catalogs saw associations of luminous O-type stars discovered across the Galaxy, and named O associations (later OB associations; Blaauw 1964).

Our view of H II regions has been intimately connected to the investigation of stellar clusters and OB associations. The first H II region discovered was the Orion Nebula by Nicolas Claude Fabri de Peiresc in 1610, independent of Galileo's observations of the Orion cluster (Chapin 1957). Grouping the cluster and the nebula as related phenomena is credited to Messier (1771). With the development of spectroscopy, further investigation enabled the detection of line emission from these nebula, specifically Hα and [O II] (Struve & Elvey 1938). Based on these observations, Strömgren (1939)

proposed that O-type stars, either individually or in clusters, were ionizing the gas in these regions, causing the observed line emission. This model proved to be useful for predicting observable phenomena: Kardashev (1959) showed that it was possible to detect hydrogen recombination emission from these regions in the radio. The field opened up with the first detection of hydrogen recombination line emission in the radio by Hoglund & Mezger (1965), which led to searches for H II regions though radio recombination line emission (Mezger & Hoglund 1967), and continuum emission (Westerhout 1958; Mezger & Henderson 1967).

The great advantage of the radio H II region searches was their insensitivity to dust extinction, allowing surveys of the entire Galaxy and determinations of its luminosity function to take place (Smith & Kennicutt 1989; Dupree & Goldberg 1970, and reference therein). Searches for the ionizing clusters powering the H II regions, however, are highly sensitive to the dust extinction since they had been conducted in the visible wavelengths. Consequently, while the census of Galactic H II regions has been treated as nearly complete since the 1970s, the census of the stellar clusters and OB associations powering them is crudely established at best.

1.1.2   The Infrared Revolution: An Embarrassment of Riches

The development of infrared detector technology over the past two decades has dramatically reshaped the field. Astronomical observations in the near-infrared wavelengths (NIR; $1\,\mu m < \lambda < 2.5\,\mu m$), like the visible, are dominated by emission from stellar photospheres. However, the effect of dust extinction is greatly diminished, enabling the detection of stars at much further distances into the Galactic disk than was previously possible.

The advent of large-scale NIR surveys has opened the possibility of finding the stellar clusters and OB associations illuminating the radio identified H II regions. Motivated by the pioneering Two-Micron Sky Survey (Neugebauer & Leighton 1969),

the modern surveys include the Infrared Space Observatory (Kessler et al. 1996), the Deep Near-Infrared Survey of the Southern Sky (Epchtein et al. 1994), and most notably the Two Micron All-Sky Survey (2MASS; Skrutskie et al. 2006). However, in a twist of fate, the surveys have identified too many stars. In 2MASS, ~ 500 million sources have been identified across the sky. With new, more sensitive NIR surveys arriving (Dye et al. 2006; Saito et al. 2012), the number of observed stars is steadily increasing. To find stellar clusters and OB associations with this influx of data, the challenge is now sorting though all point sources not associated with the cluster itself, rather than just visually identifying areas with high concentrations of stars.

In this thesis, we initially seek to identify the most luminous clusters and associations in the Galaxy through their reprocessed emission and the morphology of their surrounding structures. This approach helps overcome the embarrassment of riches that has come with near-infrared surveys.

1.2 Young, Massive Star Clusters as Stellar Nurseries

It has long been established that most stars form in clustered environments (Lada & Lada 2003). Specifically, most ($\sim 90\%$) stars form in OB associations (that are assumed to be gravitationally unbound) with the remainder mostly being born in stellar clusters (that are assumed to be gravitationally bound; Roberts 1957; Miller & Scalo 1978). Both of these objects are formed in giant molecular clouds (GMCs), thus the GMCs host nearly all of the Galaxy's star formation. While the gravitationally-bound stellar clusters remain grouped over long periods ($\sim 10^{7-9}$ yr), the associations fly apart seeding the Galactic disk with its ambient population of stars. To fully understand the process through which stars form, we must probe their natal environments.

The statistical distribution of cluster and association masses provides insight into where the star formation process occurs in the mass spectrum. The canonical value of cluster mass function's spectral index ($dN/dM \propto M^{\alpha}$) is $\alpha = -2$ between 10^2 and 10^5

$M_\odot$ (Lada & Lada 2003; de Grijs et al. 2003). This value indicates that fully half of the total mass of stars form in the most massive half of clusters ($\gtrsim 10^{3.5}$ $M_\odot$). Recently, Murray & Rahman (2010) argue for a slightly shallower value for the spectral index ($\alpha \sim -1.7 - -1.9$) which would imply that the most massive clusters contain the majority of star formation in the Galaxy. In either case, the most massive star clusters and OB associations host a significant fraction, between half to most, of the ongoing star formation in the Galaxy.

A plethora of mysteries linger in our understanding of star formation. While theory provides great insight into a variety of factors that play a role, from turbulence to magnetic fields, it is through the direct observation of the formation process that we can constrain our paradigm of stellar birth. Since the timescales of formation are longer than recorded human history, we require a large sample of regions at a variety of ages to piece together this picture observationally. Consequently, identifying the most luminous young, massive clusters and OB associations establishes this laboratory of star formation.

1.2.1   The Intial Mass Function

Star formation is inherently a statistical process where smaller stars are more likely to be produced than bigger stars. The distribution of stellar mass at the time of birth, known as the stellar initial mass function (IMF), has been well established showing little variation within the Galaxy (Kroupa 2001; Chabrier 2003). Regardless of specific form, the IMF strongly favours the production of low mass stars; the mean mass per star is $\lesssim 1$ $M_\odot$. This indicates that to form any O-type stars (with masses $\gtrsim 16$ $M_\odot$), the total stellar mass of the cluster or association must be very large; only $\sim 0.2\%$ of stars by number are O-type stars. Inversely, this indicates that if a cluster of stars contains even a single O-type star, it is probable that there are an overwhelming number of lower mass stars associated with the cluster.

Despite their relatively small numbers, the O-type star population dominate the total luminosity of a cluster or association; luminosity is a steep function of stellar mass ($dL/dM \sim M^{1.6-3.7}$; Zinnecker & Yorke 2007). This is an especially pronounced effect when only ionizing ($h\nu > 13.6$ eV) luminosity is considered: in a fully sampled cluster or association, half of the total ionizing luminosity is produced by stars with masses $\gtrsim 60$ M$_\odot$ (Murray & Rahman 2010). Consequently, taking into account the total stellar mass, the most luminous clusters and associations at a given age are also the most massive.

As stated by Zinnecker & Yorke (2007), high-mass star formation is not simply a scaled-up version of low-mass star formation. Further, the evolutionary sequence of these most massive stars is exotic in comparison to their lower mass counterparts, involving Wolf-Rayet and Luminous Blue Variable stages (Langer et al. 1994). To be able to probe the formation and evolution of these most massive stars, a large sample is required. Finding the most massive stellar clusters and OB associations will provide a more robust laboratory to test models of massive star formation and evolution than is available with the small sample of such clusters and associations know to date.

1.2.2 Measuring the Star Formation Rate

Massive, O-type stars have extremely short lifetimes; the most massive/earliest O-type stars have main-sequence lifetimes of less than 3.9 Myr (Bressan et al. 1993), in comparison to solar mass stars with lifetimes $\sim$10 Gyr. Because of this, massive stars and the clusters they reside in are effective at tracing recent and ongoing star formation. Specifically, both local and global rates of star formation can be measured using the reprocessed emission coming from these most luminous stars. In fact, most modern measures of the star formation rate are dependent on some form of emission arising from massive stars.

Traditional tracers of extragalactic star formation include the ultraviolet continuum,

hydrogen or forbidden oxygen line, and far-infrared continuum emission (Kennicutt 1998). Due to the substantial dust extinction that prevents many of these tracers from being detected for all but the nearest star forming regions, these methods are not used for global Galactic studies. Rather, radio measurements of H II regions (§1.1.1) have been traditionally used for measuring the Galactic star formation rate (Smith et al. 1978; Murray & Rahman 2010). However, the proximity of objects in the Milky Way as compared to even the nearest galaxies enables alternative measures of the rate, including counting the total number of young stellar objects detected in the infrared (Robitaille & Whitney 2010; Lada et al. 2010).

Recent work by Chomiuk & Povich (2011) has shown a discrepancy between the tracers of star formation: either the Galactic tracers lead to an overestimate or the extragalactic tracers lead to an underestimate. The solution to this discrepancy will likely come from more detailed investigation of Galactic star forming regions, specifically from the detailed study of stellar populations and emission arising from young, massive star clusters and OB associations.

1.3   Feedback produced by Young Massive Star Clusters

Massive star formation is a violent process; as gas accrets into a gravitationally-bound clump and begins forming the protostar, some of the energy from the collapse powers winds and jets pushing outward. As the process of nuclear fusion begins in the star's blistering core, the energy produced inside and from the motions of the falling gas heats the surface, producing a plethora of high energy photons. These photons permeate the surrounding natal medium, ionizing and heating it, causing it to balloon outward. In addition, some of the material from the star itself is launched outward at high speeds producing an energetic stellar wind. With large numbers of these young, massive stars together, as is common in massive stellar clusters and OB associations, the copious energetic photons produced transfer significant amounts of momentum

to their absorbing material pushing it away from the central cluster. Finally, in their last gasp of life, the massive stars detonate in supernovae, injecting excessive energy into their host medium. Collectively, these processes are referred to as "energetic feedback", or more simply, *feedback*.

The massive, young stellar clusters and OB associations, being the largest repository of the massive stars, are the dominant sources of feedback within the Galaxy. It is only through identifying and characterizing the complete Galactic population of young, massive star clusters and OB associations that we can produce a global view of energetic feedback and its effect on the Galaxy's ecology and structure.

1.3.1   Mechanisms of Interaction

The classical model of feedback from massive stars was proposed by Oort (1954) an O-type star ionizing its surrounding medium. Schematically, the mechanism uses H II region gas pressure to inflate a warm bubble of ionized gas into the surrounding medium: the ionizing photons produced by the O-type stars are absorbed by the gas surrounding it. The ionized gas heats up and the pressure increases. Since the ionized gas is no longer in pressure equilibrium with the surrounding, neutral medium, the ionized region expands outward, sweeping up its surroundings into a shell at its border.

However, O-type stars produce more than just ionizing photons; stellar winds produced by the same massive stars have been noted to provide an additional source of feedback through their mechanical interaction with their surrounding medium (Avedisova 1972; Castor et al. 1975). This mechanism uses the high rate of mass loss from O-type stars ($\sim 10^{-6}$ M$_\odot$ yr^{-1}; Puls et al. 1996) to physically push on the surrounding medium. The ram pressure of the winds cause a region of hot, shocked gas to inflate into a bubble. The differing models of this mechanism vary in their size and luminosity predictions. However, the recent work by Harper-Clark & Murray

(2009) indicates that the stellar winds may be dynamically unimportant in the case of an inhomogeneous surrounding medium since the winds are able to leak outside of the shell.

Protostellar outflows have been shown to drive turbulence into the material surrounding a forming star (Matzner 2007; Norman & Silk 1980). While this method is not limited to just the most massive stars, it has been shown to significantly drive turbulence in OB associations, especially at the early stages of cluster formation.

Supernovae are thought to be significant contributors to cluster feedback through their heating and material ejection (McKee & Ostriker 1977; Chevalier 1974). Since supernovae are detonated at the end of the life of a massive star, this mechanism does not act until later in the evolution of a massive cluster and in short, intense bursts. However, for the most massive clusters, large numbers of supernovae can occur in relatively quick succession, all with large amounts of energy being deposited into the interstellar medium.

Most recently, the radiation pressure from young, massive clusters and OB associations has been shown to be a significant contributor to the feedback of these objects into their natal environment (Murray et al. 2010). The radiation pressure is channeled into feedback through the absorption and scattering of photons produced by the central cluster; as the photons are absorbed or scattered, the momentum of the photons is transferred to the absorbing material. Since the primary source of opacity in the interstellar medium is dust, it is primarily the dust to which the momentum is transferred. Krumholz & Matzner (2009) find that while H II gas pressure is likely the driving mechanism for regions with only a handful of massive stars, radiation pressure may dominate for regions powered by massive clusters.

It is likely that each of these mechanisms have their own regime of influence based on the powering cluster's mass (and luminosity), the radial distance from the cluster, and the age of the system. Initial observational studies support this hypothesis (Lopez

et al. 2011), but a systematic study of massive clusters and their surrounding media is necessary to determine the dominant feedback mechanisms and their reach. This highlights the need to identify the Galactic population of young, massive clusters.

1.3.2   Interactions with the Natal Environment

A long standing problem of star formation has been that of inefficiency: what prevents all gas in a giant molecular cloud from turning into stars? Alternatively posed, what prevents gravity from collapsing all gas in a GMC into stars in a free-fall time? Turbulence has been posed as the primary mechanism of support, consistent with the observed CO linewidths of Galactic GMCs (Zuckerman & Evans 1974). Numerical and analytic studies indicate that gas accretion onto the cloud is a possible driving source of the required turbulence (Vázquez-Semadeni 2011; Goldbaum et al. 2011). However, massive stars and the clusters in which they reside have been attributed to dominate the support and destruction of GMCs (Matzner 2002). GMCs being the birthplaces of these massive clusters, feedback from the clusters will directly act on the molecular gas. The identification of the Milky Way's most luminous clusters and OB associations will open new sites for the investigation of the feedback of the clusters into their natal environment.

1.4   Thesis Outline

In this thesis, we seek to identify the most luminous young, massive clusters and OB associations in the Galaxy. We examine 13 of the 14 most luminous free-free sources in the Galaxy from Murray & Rahman (2010), responsible for 1/3 the total ionizing luminosity, to identify coherent complexes of star formation in Chapter 2. In Chapter 3, we search for the central powering OB association of the most luminous complex from the previous chapter, the Dragonfish Nebula. We conduct spectroscopy on

sources within the previously identified candidate association to confirm the existence of the most luminous OB association in the Galaxy in Chapter 4. Refining the method of Chapter 3, we use it to find candidate clusters/associations in all the remaining complexes in Chapter 5. We summarize our conclusions in Chapter 6 and discuss future directions.

Chapter 2

Star Forming Complexes in the Spitzer Glimpse Survey

A preliminary version of this chapter was published as:

"A New Sample of Very Massive Star Forming Complexes in the Spitzer GLIMPSE Survey"

Rahman, M., & Murray, N., 2010, The Astrophysical Journal, 719, 1104

2.1   Chapter Overview

We examine the thirteen most luminous sources in the WMAP free-free map using the Spitzer GLIMPSE and MSX surveys to identify massive star formation complexes, emitting one-third of the Galactic free-free luminosity. We identify star forming complexes by a combination of bubble morphology in $8\,\mu$m emission and radio recombination line radial velocities. We find 40 star forming complexes associated with our WMAP sources, and determine unique distances to 31. We interpret the bubbles as evidence for radial expansion. The radial velocity distribution for each source allows us to measure the intrinsic speed of a complex's expansion. This speed is consistent with the size and age of the bubbles. The high free-free luminosities,

combined with negligible synchrotron emission, demonstrate that the bubbles are not driven by supernovae. The kinetic energy of the largest bubbles is a substantial fraction of that measured in the older superbubbles found by Heiles. We find that the energy injected into the ISM by our bubbles is similar to that required to maintain the turbulent motion in the gas disk inside 8 kpc. We report a number of new star forming complexes powered by massive ($M_* > 10^4 M_\odot$) star clusters. We measure the scale height of the Galactic O stars to be $h_* = 35 \pm 5\,\mathrm{pc}$. We determine an empirical relationship between the $8\,\mu\mathrm{m}$ and free-free emission of the form $F_{8\,\mu\mathrm{m}} \propto F_{\mathrm{ff}}^{1.1}$. Finally, we find that the bubble geometry is more consistent with a spherical shell rather than a flattened disk.

2.2 Introduction

The most massive star clusters ($M_* > 10^4\ M_\odot$), referred to as *super star clusters*, have been regularly observed in extragalactic star forming complexes (Ho 1997), but until recently such massive clusters have evaded detection in our own Galaxy. This has largely been due to the heavy dust obscuration within our own Galactic disk. These clusters are home to the most massive stars in the Galaxy, including the vast majority of O and B stars. The stars in turn produce most of the ionizing luminosity and stellar winds that inject energy and momentum into the interstellar medium (ISM), blowing bubbles and producing shell structures. Over the last decade a number of young, massive clusters have been found in the Galaxy, including the Arches and Quintuplet clusters near the Galactic centre region (Figer et al. 1999), Westerlund 1 (Clark et al. 2005), and RSGC 1, 2, & 3 (Figer et al. 2006; Davies et al. 2007; Clark et al. 2009), either by directly imaging the stars, or by the stellar radio emission.

Another possible method of locating these young, massive star forming complexes is to look for the environmental effects caused by such clusters, such as H II regions, or shell and bubble structures. These effects can be observed in wavebands where

extinction through the Galactic plane becomes less of an issue, such as the radio and infrared. Extensive surveys of H II regions both in the northern and southern sky have been conducted with limited success in finding these massive star forming complexes (for a recent census, refer to Conti & Crowther 2004).

In Murray & Rahman (2010, hereafter MR10), we used the Wilkinson Microwave Anisotropy Probe (WMAP) maximum entropy method free-free foreground emission map (Bennett et al. 2003; Gold et al. 2009) to determine the star formation rate in the Galaxy. WMAP is uniquely positioned for global Galactic star formation studies, with its high sensitivity, all-sky, multi-frequency coverage that allows for the robust separation of the synchrotron, dust, and free-free emission that are produced by the Galaxy. We found that the 18 most luminous regions (located within 14 WMAP sources) produce over one-third the total ionizing luminosity of the Galaxy, implying that one-third the total number of O stars reside in these regions. These sources contain bubble structures having radii ranging from 5 to 100 pc. Most of the ionizing photons from the embedded stellar population escape the bubble and ionize the surrounding material, creating the Extended Low-Density regions (ELD; Lockman 1976; Anantharamaiah 1985a;b). Examination of the Spitzer Galactic Legacy Infrared Midplane Survey Extraordinaire (GLIMPSE) 8 μm images shows that many known H II regions appear on shells or walls of bubbles. These known H II regions are generated either by the illumination of swept up material by the central cluster, or by star formation triggered in the swept up material. In either case, the ionizing luminosity of the WMAP source is larger than that given by summing the total emission from all of the H II regions in the area.

Further, a large number of the known H II regions in a WMAP source had not previously been associated with one another, a result of their disparate radial velocities. The range of radial velocities had been translated into different distances along the line of sight. We, on the other hand, interpret the differences in radial velocity as the

result of bubble expansion; the H II regions lie on shells, with velocity differences of order $15 \, \mathrm{km \, s^{-1}}$, consistent with the expected expansion speed of a bubble in the ISM, e.g., Harper-Clark & Murray (2009).

In this chapter we analyze the most luminous WMAP sources using the GLIMPSE and MSX surveys, and previously known H II region velocities. We describe our procedure for associating the H II and $8 \, \mu$m emission using an intrinsic expansion velocity criteria in §2.3. We discuss the general properties of the star forming complexes (which we define in §2.3.1) in §2.4. We discuss each of the star forming complexes in depth in §2.5. In §2.6, we determine the scale height of O stars in the Galactic disk, quantify the relationship between the $8 \, \mu$m and free-free emission, discuss the expansion of the star forming complexes as a turbulent driving mechanism of the Galaxy's molecular gas, and comment on the three-dimensional geometry of observed bubble structures. Finally, we summarize our results in §2.7.

2.3 Data Analysis

In MR10, we divided the total flux of the WMAP regions along a given line of sight based on various distance determinations (radio recombination lines, molecular absorption lines, and stellar distances). Using this division, one-third of the Galactic free-free emission arises from 14 discrete WMAP sources. These sources contain more than one-third of the O star population of the Galaxy.

Here we investigate in more detail, using additional radial velocities, the 13 most luminous free-free sources in the Galaxy from MR10 (we exclude the Galactic Centre region since it is well studied already).

A number of well-known massive star forming regions are not included in our sample, including the Carina region, NGC 6357 and Cygnus OB2. These regions, identified in MR10, have lower ionizing luminosities than the regions we investigate in this study. The WMAP sources are highly confused, so not every complex identified

in this chapter will be home to a super star cluster, but we expect that each of the WMAP sources we consider will contain at least one complex that may be home to a super star cluster with a mass greater than those found in Carina, NGC 6357, and Cygnus OB2.

Each of the WMAP sources are fit by ellipses, with major axes between ∼2 to 5 degrees; sizes, positions and fluxes are given in Table 2.1. These sources are confused (contain multiple star forming complexes) as a result of the large beam size of the WMAP satellite. The WMAP free-free map is presented in Figure 2.1, indicating the location of each of the thirteen sources.

We use published radial velocity measurements together with GLIMPSE 8 μm images to better resolve and classify these star forming complexes. This improves on our use of the catalogue of Russeil (2003) in MR10. In other words, we classify star forming complexes on the basis of kinematic distances (as determined through radial velocities towards known H II regions) and morphology seen in the 8 micron bands.

We carried out a SIMBAD search for H II regions within each of the WMAP sources and compiled the associated hydrogen recombination line velocities.

Our morphological analysis was primarily conducted using the 3.1 by 2.4 degree Band 4 mosaic images from GLIMPSE (Benjamin et al. 2003). In many cases, these mosaics were insufficiently large to encompass the entire WMAP sources from MR10. In these cases, adjacent images were mosaicked together using the Montage package. In cases where the sources were outside the GLIMPSE coverage, we substituted Band A mosaics from MSX (Price et al. 2001).

We use the 8 micron band because it is dominated by polycyclic aromatic hydrocarbon (PAH) emission, which Cohen & Green (2001) have shown to trace the free-free emission reasonably well. The physical origin of this relationship stems from the effects of ultraviolet radiation, presumably coming from a massive star or massive stellar cluster. The high-energy UV photons ionize the region, giving rise to free-free emission. Lower energy ultraviolet photons excite PAH molecules, causing them to

emit in one of many vibrational modes. Specifically in the GLIMPSE Band 4 and MSX Band A wavelength ranges, these vibrational modes are C-C stretching at 7.6 μm, and C-H in-plane bending at 8.7 μm (Allamandola et al. 1989). However, higher energy extreme ultraviolet photons destroy the molecules rather than excite them (Voit 1992), so areas with sufficient high-energy ultraviolet flux should produce little PAH emission. This would result in a lack of PAH emission close to a UV source, with substantial emission coming from outside the radius where extreme UV photons are able to penetrate. However, small dust grains located throughout the H II region will also be emitting in the 8 μm band, so, while no PAH emission is expected, warm dust continuum emission should be present. This leads to warm dust emission dominating the 8 μm band towards the centres of H II regions, while PAH emission dominates at greater distances (Povich et al. 2007). Consequently, we use the 8 μm GLIMPSE and MSX images as tracers of the presence of massive stars through this work. We find a surprisingly strong relationship between the 8 μm emission and free-free emission, which we discuss in §2.6.2.

2.3.1 Definition of Star Forming Complexes

We define star forming complexes (SFCs) as subsets of WMAP sources having similar radial velocities (± 15 km s^{-1}), copious 8 μm emission in Spitzer and/or MSX images, and finally, morphologies that are consistent with physical association, e.g., bubble, shell, or finger/pillar structures. In other words, star forming complexes are regions identified by features correlated both in space and in velocity.

To determine the location and size of each of the star forming complexes we overlaid the positions and velocities of the known H II regions onto the 8 micron mosaics of the region and visually inspected the result. An example classification based on morphology and velocity is shown in Figure 2.2.

To associate each of the H II regions with a specific SFC, the H II region must

satisfy a number of criteria; not only do each of the identified H II regions have to fall within the velocity criteria, but they must also be positionally coincident with a morphological feature. In most cases, we identify known H II regions as bright areas of $8\,\mu$m emission, usually on the shells or in the centre of identified regions. In addition, the distribution of velocities along any given sight-line within a specific WMAP source exhibit a natural grouping of velocities of less than or equal to $\pm 15\,\mathrm{km\,s}^{-1}$, indicating that our velocity criteria has an empirical basis in addition to its theoretical motivation.

We note that some confused galactic sight-lines have a velocity separation between spiral arms of less than $20\,\mathrm{km\,s}^{-1}$, and thus our velocity criteria may confuse H II regions associated with different spiral arms with an overlapping SFC. However, the distributions of H II region velocities are heavily centre weighted and thus small degree of contamination will not greatly affect the mean v_{LSR} and kinematic distance of the SFC. In addition, these regions often demonstrate complicated structure in position and velocity space, and the measured H II region velocities may also be attributed to turbulent motions within the SFC, expansion of sub-regions within the SFC, or the SFC as a whole. Consequently, we view the measured expansion velocities as an upper limit.

Having determined the size and location of a star forming complex, we calculated a median velocity from the measured velocities. A kinematic distance was then determined using the Clemens (1985) Galactic rotation curve. In cases where the kinematic distance is ambiguous, we used published absorption line data, where available, to determine if the complex is at the "near" or "far" distance.

In the next section, we describe each of the "star-forming complexes". In the supplemental online material, we present tables of each of the known H II regions with positions and velocities that are associated with each of the star forming complexes.

Table 2.1. WMAP Source List

Name	l (deg)	b (deg)	$smaj$ (deg)	$smin$ (deg)	PA (deg)	S_{ff} (Jy)	Luminosity Rank	Notes
G10	10.4	-0.3	0.61	0.44	-21.2	86	12	W31
G24	24.5	0	1.96	0.83	-7.2	1377	10, 11	W41, W42
G30	30.5	0	2.27	0.95	2.7	1585	3, 8	W43
G34	34.7	-0.2	0.92	0.57	6.1	285	6	⋯
G37	37.6	0	0.8	0.71	-59.9	244	13	W47
G49	49.3	-0.3	0.99	0.55	-13.5	458	9	W51
G283	283.9	-0.6	1.37	0.78	-32.1	848	15	NGC 3199, RCW49, Partial GLIMPSE Coverage
G291	291.2	-0.7	1.04	0.75	-31.1	688	14	NGC 3603, NGC3576, No GLIMPSE Coverage
G298	298.4	-0.4	0.91	0.73	-37.3	313	5	⋯
G311	311.6	0.1	1.72	0.93	6.5	766	16	⋯
G327	327.5	-0.2	1.55	0.83	-10.7	943	17	⋯
G332	332.9	-0.3	1.56	0.93	-3.3	1787	7	⋯
G337	337.3	-0.1	2.58	1.2	-8.9	2239	2, 4	⋯
⋯	359.9	-0.1	1.2	0.51	-3	1105	1	Galactic Centre region, exluded from analysis

Note. — The luminosity rank indicates the ranking of the source with respect to the ionizing luminosity produced, with multiple ranks indicating sources that were divided in MR10. The free-free flux is measured in the W band at 90 GHz from the WMAP Free-Free Foreground Emission Map (Murray & Rahman 2010).
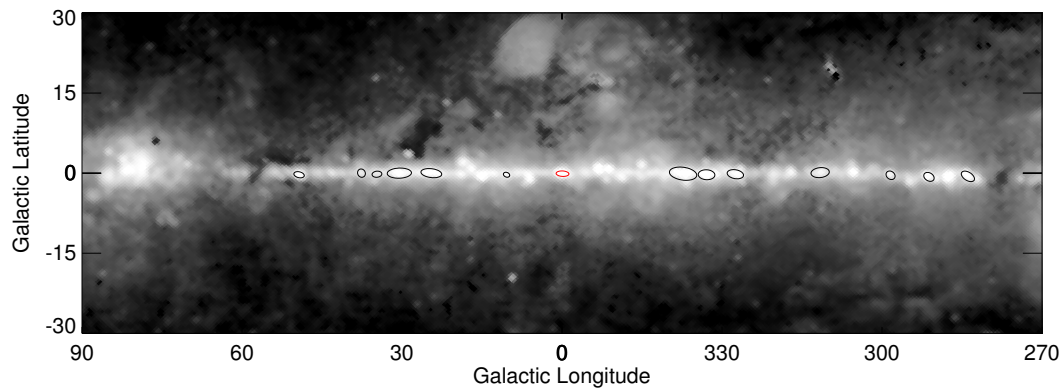
Figure 2.1: The WMAP free-free foreground emission map with the target sources indicated with black ellipses. The Galactic Centre region, which has been excluded from this work, is indicated in red. The map is described in MR10. (A colour version of this figure is available in the online journal.)

2.4   Properties of Star Forming Complexes

The combined analysis of the WMAP sources with the GLIMPSE image mosaics and the H II region velocities yields 40 star forming complexes. Ten of the thirteen WMAP sources harbor multiple star forming complexes; sources within the inner third of the Galaxy are found to be especially confused, with multiple SFCs. However, as already noted, combining morphology from the 8μm emission with the velocities of known H II regions allows for a reasonably clear view of the physical separations of the star forming complexes.

These star forming complexes have mean radii between an arcminute and a degree, and distances between 3 and 17 kiloparsecs. The angular sizes translate into physical radii between 3 to 75 parsecs. The Galactic distribution of the star forming complexes is presented in Figure 2.3.

The majority of known H II regions in the star forming complexes lie in shell-like structures traced by $8\,\mu$m emission in the Spitzer or MSX images. Most of the remainder are found in the centre of the SFC.
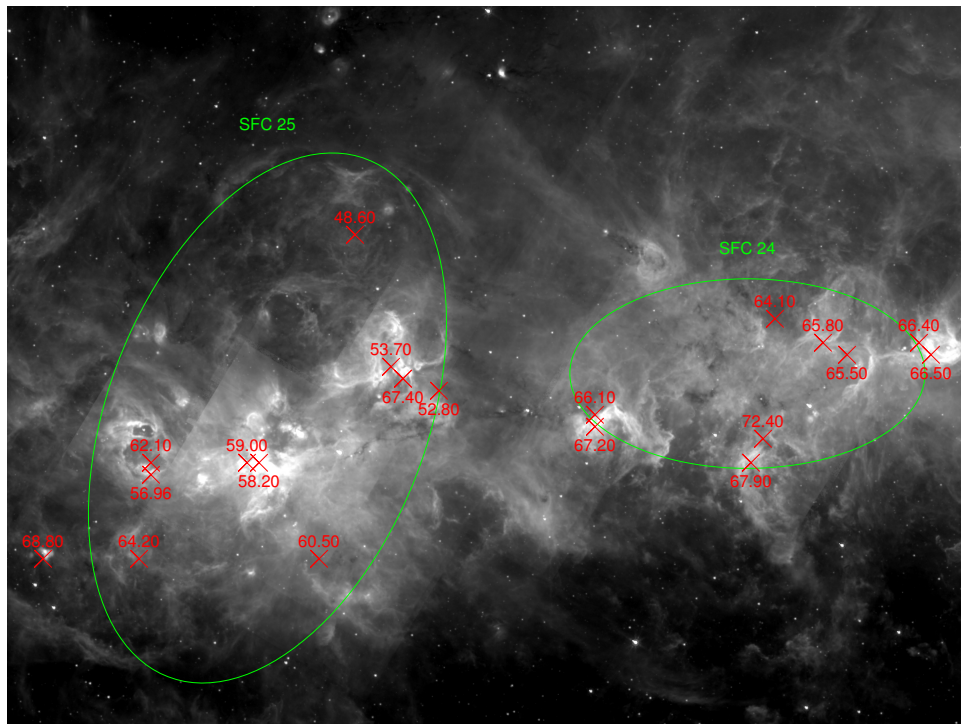
Figure 2.2: A Spitzer GLIMPSE image of the G49 WMAP source with the two star forming complexes indicated with the green ellipses and the H II region velocities indicated with the red crosses. (A colour version of this figure is available in the online journal.)

We interpret those H II regions lying on shell-like structures in one of two ways. In many cases it is clear that the H II region is simply swept up shell material illuminated by a central cluster. In other cases, however, the shell material is illuminated by young stars resulting from triggered star formation in the swept up shell, as described by Elmegreen (1998). In some cases, the triggered stars are blowing their own bubbles in the shell.

In many cases, we find a low level of emission towards the centre of the bubble or shell structure; we interpret this as the evacuation of the material from the interior of the bubble.

Although a comprehensive search for known H II regions was conducted over each of the WMAP sources, not every emission feature in the 8 micron GLIMPSE image is associated with a radial velocity determination. In some cases, particularly bright $8\,\mu$m features in the GLIMPSE mosaics are not coincident with any radial velocity measurements, indicating that we are potentially missing star forming complexes within the WMAP sources. We identify these complexes in the description of each of the WMAP sources, and we suggest that further radial velocity measurements would be instructive. This does add an uncertainty in determining the true stellar population of such regions and we comment where this is the case. In some cases we believe that a significant star forming region has not been identified due to a lack of conclusive H II data.

We present our SFCs in Table 2.2 with the columns as follows: column (1) the catalogue number, columns (2) and (3) the position of the sources in Galactic coordinates, columns (4) and (5) the semimajor and semiminor axes of the complexes in arcminutes, column (6) the position angle of the complex, column (7) the median velocity in km s^{-1}, columns (8) and (9) the measured and corrected half-spread of velocities in km s^{-1} where sufficient H II regions are identified as associated with the star forming complex, column (10) the distance to the complex in kiloparsecs, column (11) the mean

radius of the source in parsecs, column (12) the dynamical age of the complex given the velocity spread, and column (13) the reference that resolves the distance ambiguity (where applicable). In cases where the kinematic distance ambiguity remains, we indicate the properties resulting from both distances in columns (10), (11), and (12). We refer to complexes from this table as "SFC" followed by the catalogue number hereafter.

We present 8 micron images from GLIMPSE or MSX for each of the WMAP sources in Figures 2.4 to 2.16. On each of these images, the location and size of the WMAP source is indicated with a dotted ellipse, and the location of SFCs is indicated by a solid (red, in the online copy) ellipse. Each of these images is presented with a logarithmic stretch to highlight fainter morphological features.

While individual velocities towards H II regions may be known with great precision (generally to better than $\pm\,1\,\mathrm{km\,s^{-1}}$), velocities to the entire complexes are determined with much less accuracy; the H II regions are randomly distributed (in angle) around sources. Further, some of the SFCs are associated with a very limited number of radial velocities measurements. In either case, the maximum error in the mean source velocity is constrained by our selection criteria that a complex have a velocity spread: $2\Delta v_{\mathrm{m}} \leq 30\,\mathrm{km\,s^{-1}}$. This maximal velocity error corresponds to an error in the kinematic distances of approximately 30%.

To estimate the half-velocity spread, Δv_{m}, we first require that a SFC have multiple velocity measurements available. Next, we require that there be a spread in the measured velocities greater than $3\,\mathrm{km\,s^{-1}}$; otherwise we suspect that what appear to be multiple velocity measurements are actually measurements of the same H II region (the Galactic coordinates are often not sufficiently precise to discriminate between physically different versus apparently different sources). Given a complex that satisfies these two criteria, we define the *measured* Δv_{m} as half the difference between the maximum and minimum radial velocity.

This parameter must be corrected for sampling effects; it is unlikely that the maximum and minimum velocity of an expanding complex will be found in a random selection of H II regions. Further, since most of the known H II regions appear on the edges of (presumably expanding) shells, the component of the expansion velocity projected onto the radial velocity is expected to be smaller than unity. Thus the measured half-velocity spread would generally be an underestimate of the actual expansion velocities of the complexes.

We correct the half-velocity spread by a geometric factor found by running a Monte Carlo simulation modeling the difference between the observed half-velocity spread and the actual expansion velocity with a given number of velocity observations. The mean correction factor is 2.0, 1.4 and 1.2 for 5, 10 and 15 velocity measurements respectively. The error on this factor ranges from a factor of 2 for 5 velocity measurements, to 15% for 15 measurements. The *corrected* half-velocity spreads, Δv_c, are also given in Table 2.2. For complexes where less than 5 velocity measurements are available, no correction factor is applied as the Monte Carlo simulation shows that the result is unreliable. These complexes do not have a corrected half-velocity spread presented. The measured half-velocity spreads for these complexes should be treated as lower limits of the expansion velocity.

The dynamical age, τ_{dyn}, of the system is determined by dividing the mean radius of the complexes by the half-velocity spread. The dynamical ages of all of the complexes are below 10^7 years, consistent with the existence of massive main-sequence stars producing large amounts of ionizing luminosity.

The true age of each of these systems is an undetermined quantity but the selection criteria for these complexes imposes some constraint on the ages. Specifically, these complexes are selected as the most luminous in free-free emission, indicating the presence of massive O stars, specifically those with short main-sequence lifespans. In MR10 we showed that the total ionizing luminosity of a cluster with a standard initial

stellar mass function rapidly decreases after the cluster reaches an age of 4 Myrs. This indicates that the majority of the ionizing luminosity in a young cluster is quenched even before the late-O stars evolve off the main sequence.

In SFCs where a discernible, closed bubble is illuminated with free-free or $8\,\mu$m emission, an upper limit to the true age exists; a closed, fully illuminated bubble indicates the existence of a central ionizing source, which presumably is also blowing the bubble. This allows us to put an upper limit on the age of 4 Myrs, the lifetime of the most massive stars that produce the majority of ionizing photons in the Galaxy. In SFCs with only a diffuse bubble structure there is an ambiguity; the bulk of the ionizing luminosity may come from a central cluster, or it may come from star clusters that have been triggered along the shell of the region evacuated by a central cluster. In the latter case, it would be incorrect to constrain the age of the complex to be less than 4 Myrs. This circumstance is particularly relevant when searching for a central stellar cluster; if the age cannot be constrained to under 4 Myr, the most massive stars in the central cluster have already evolved off the main sequence, leaving more evolved objects rather than bright, blue main-sequence objects.

2.4.1   Bubbles

In many of these complexes, we observe bubbles at a variety of scales. Some bubbles essentially enclose the associated star forming complexes, while smaller bubbles often lie in the walls of larger bubbles. Many of the smaller bubbles are listed in Churchwell et al. (2006), but the larger bubbles, with radii larger than 10′, have not been previously catalogued.

In MR10, we find that each of the WMAP sources that we have selected require ionizing luminosities of $Q_0 > 10^{51}$ s^{-1}, consistent with young stellar populations with $M > 10^4$ M$_\odot$. Such massive clusters may drive superbubbles, a notion supported by the fact that the largest bubbles we find have mean radii approaching 50 pc.

We present a list of bubbles associated with each of the star forming complexes in Table 2.3. The columns are as follows: column (1) the catalogue number, columns (2) and (3) the positions of the bubbles in Galactic coordinates, columns (4) and (5) the semimajor and semiminor axes of the bubbles in arcminutes, column (6) the position angle of the bubble, column (7) the associated star forming region from Table 2.2, column (8) the mean radius of the bubble in parsecs using the distances to the associated star forming complexes, column (9) the morphology classification flag of the bubble, and column (10) the GLIMPSE bubble catalogue number from Churchwell et al. (2006). Where the kinematic distance ambiguity has not been resolved, the mean radius of both the near and far distances are indicated. The morphology classification flag is C if a nearly closed or complete shell is visible in the GLIMPSE 8 micron image, or B if the bubble appears to be broken or blown-out. The GLIMPSE bubble catalogue number is indicated where the bubble has a similar position, size and shape to the source indicated in Churchwell et al. (2006).

2.4.2   H II Region Radial Velocities

Finally, we list the individual H II region velocities for each of the identified star forming complexes in Table 2.4, available as an online supplemental table. The columns are as follows: column (1) the associated star forming complex from Table 2.2, column (2) the name of the H II region, columns (3) and (4) the positions of the complex in Galactic coordinates, column (5) the velocity of the complex with respect to LSR in km s^{-1}, and column (6) the reference from which the velocity was taken.
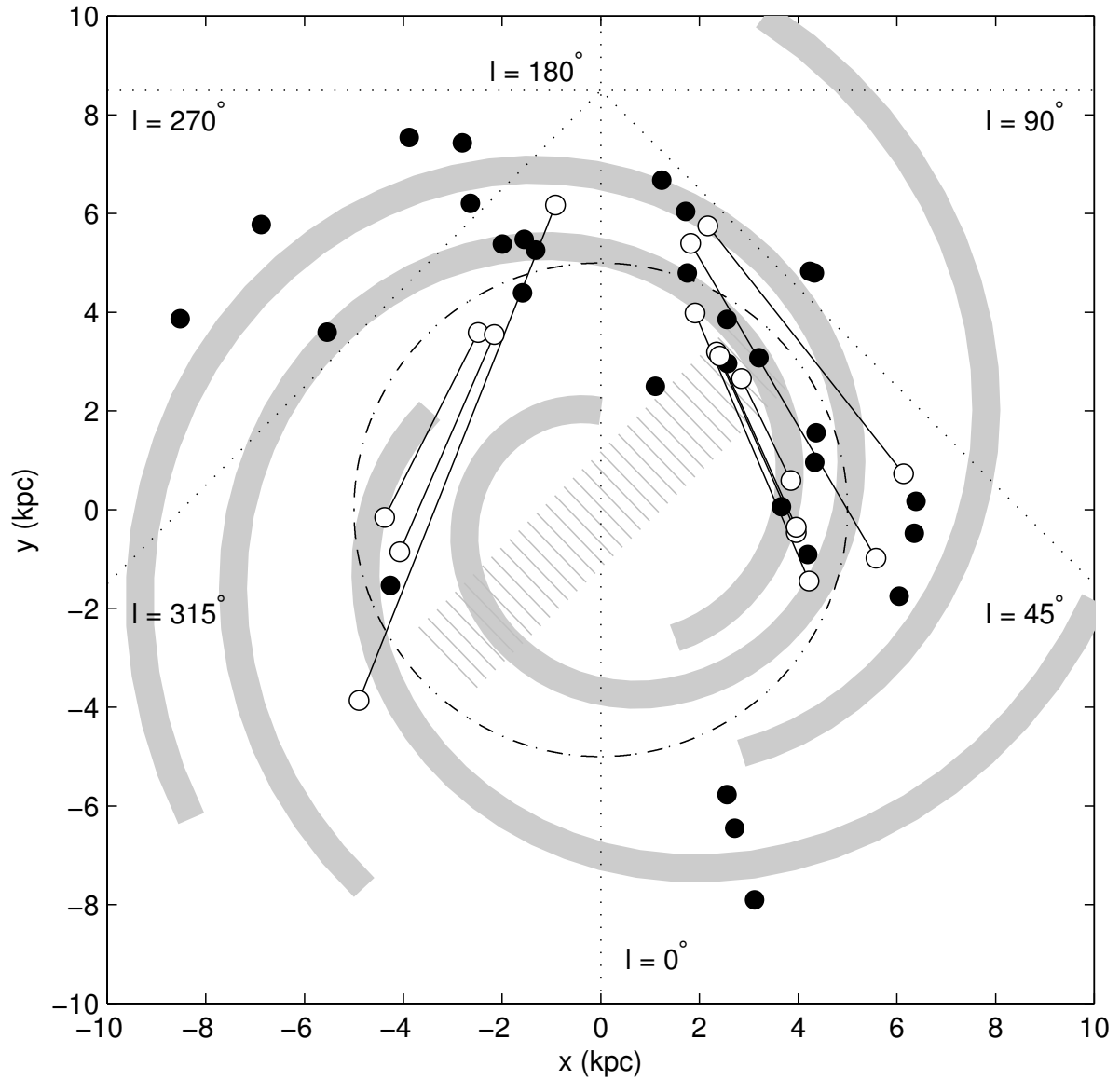
Figure 2.3: The Galactic distribution of the Star Forming Complexes identified in this analysis. The filled circles indicate sources for which a unique distance has been determined, while open circles represent sources for which the kinematic distance is ambiguous. Both the near and far distances of these sources are presented with lines connecting the two. The dash-dotted circle indicates the radius within which half the total ionizing luminosity of the Galaxy is produced (from MR10). The spiral arms (solid grey lines) overlaid are taken from Nakanishi & Sofue (2006), and the Galactic central bar (dashed grey line) is taken from Benjamin et al. (2005).

2.5 Individual WMAP Sources

2.5.1 G10 including the W31 region

This WMAP source is dominated by four seemingly disparate star forming complexes (see Figure 2.4), although SFC 1 and 2 may be associated as they are both in W31 (Westerhout 1958). We begin with a discussion of these two complexes.

SFC 1 and 2 contain the brightest $8\,\mu$m emission, although there is a significant 8 micron background over this entire WMAP source that we cannot clearly attribute to any of the 4 complexes. In addition to being in W31, SFC 1 and 2 are also linked by their close angular proximity and similar radial velocities. We treat them as separate complexes as they are each enclosed by their own shell structures. The high surface brightness 8μm emission located in the centre of each of SFC 1 and 2 is indicative of a young central cluster that has not had time to evacuate its environment. This is consistent with the short dynamical time determined for SFC 1. Strong molecular line emission is found by Kim & Koo (2002), who conclude that there are active interactions between the forming stellar clusters and their parent molecular clouds. They also assume a closer distance, associated with the expanding 3 kpc arm of the Galaxy (with a distance of 6 kpc from LSR), but they do note that there is evidence that the complex is at the further distance. Assuming the near distance, they estimate star cluster masses of 1.22×10^4 M$_\odot$ for SFC 1 and 3.11×10^3 M$_\odot$ for SFC 2.

The radio nebula G10.0-0.3 and associated soft gamma repeater are coincident with SFC 1 with a distance of 14.5 kpc, consistent with our distance (Corbel et al. 1997; Vasisht et al. 1995). Further, there exists a luminous blue variable with a total mass (single or binary) exceeding 190 M$_\odot$ consistent with the further distance (van Kerkwijk et al. 1995; Eikenberry et al. 2004). The complex also contains a soft-gamma repeater (Kulkarni & Frail 1993). Corbel & Eikenberry (2004) suggests that W31, specifically SFC 1, may be separable along the line of sight into a component in the 3 kpc spiral

arm, and a component at 14.5 kpc. We find this to be consistent with SFC 1 being a massive young star forming cluster at a distance of 14.5 kpc, with shell-like structure evident in the north-west and south-east edges of the region. Adjusting the values of Kim & Koo (2002) for the further distance, clusters of masses 7.1×10^4 M$_\odot$ and 1.8×10^4 M$_\odot$ are required for SFC 1 and 2 respectively.

SFC 3 and 4 are distinctly separated from SFC 1 and 2 as they both have substantially different radial velocities; the difference in velocities being $60 \, \text{km} \, \text{s}^{-1}$ and $15 \, \text{km} \, \text{s}^{-1}$ respectively. We view SFC 3 as a smaller, closer star forming complex than 1 and 2. SFC 4, however has the morphology of a blown out bubble. The distance to this region, 16.7 kpc, implies a large bubble size of 46 pc. The strong $8 \, \mu$m illumination on the northwest side of the complex is potentially a triggered star forming complex from the expansion of the now blown out bubble. However, the bubble structure is illuminated along the shell in all but the south (in the proposed area of blowout), indicating that a central ionizing source still exists within the bubble that is illuminating the southeast side; the interior of the bubble appears evacuated. We infer that the central cluster is still sufficiently young to possesses ionizing stars.

At the location $(l, b) = (10.7, -0.16)$, there appears to be a hole in the background level of $8 \, \mu$m emission. There are no known H II regions within this hole, suggesting that this is an extinction effect. If this is an extinction effect at 8 microns, the column towards this complex must be particularly large. We suspect that this is an infrared dark cloud (IRDC). In 2MASS (Skrutskie et al. 2006), there does not appear to be any significant void of background stars, indicating that this IRDC is sufficiently distant to have no effect on the local field star population, but is closer than the source of the $8 \, \mu$m background in this region. More detailed study of this object is required to establish its existence, let alone determine its physical properties.
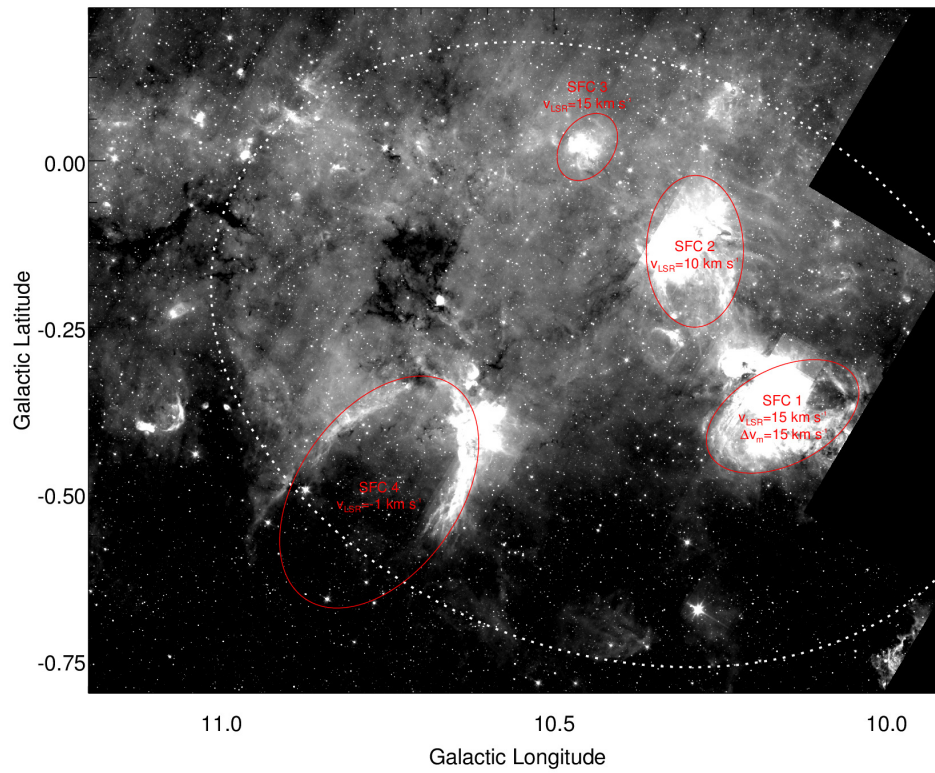
Figure 2.4: The 8μm GLIMPSE Image of the star forming complexes in G10. For each star forming complex, the v_{LSR} and v_{m} (where available) are indicated.

2.5.2   G24 including the W41 and W42 Regions

WMAP source G24 (Figure 2.5) encompasses a particularly complicated region. It is one of the largest WMAP sources (spanning nearly 4 degrees in the Galactic plane) and contains both W41 and W42 (Westerhout 1958).

SFC 5 encompasses the supernova remnant W41. In the one square degree region surrounding W41, velocity measurements suggest the H II regions are caused by confusion of spatially separated H II regions (Leahy & Tian 2008), consistent with the 4 spiral arms along the line of sight in this direction. We find SFC 6 associated with one of the overlapping components. There is a second known supernova remnant, G22.7 -0.2 (van den Bergh 1978), also within SFC 5.

In addition to SFC 5 and 6, we identify 6 additional star forming complexes within this WMAP source. For a number of these complexes, specifically SFC 7, 9, and 12, the kinematic distance ambiguity remains. SFC 7 and 8 are easily distinguished by the presence of H II regions along their perimeters. There is a lack of strong central $8\,\mu$m illumination in both of these star forming complexes, indicating that their centres have been evacuated. In addition, the rims of SFC 7 and 8 are not particularly bright in $8\,\mu$m emission, indicating that the hypothesized shell has dispersed or that the central cluster is no longer emitting ionizing radiation. Either circumstance implies that these two complexes are older (> 4.5 Myr) and that the majority of the observed $8\,\mu$m and free-free emission is provided by triggered regions on the perimeter.

SFC 9 contains only a single H II region velocity in its centre, but exhibits a clear bubble morphology. SFC 10 is a much larger region, with a mean radius of 43 pc. While the brightest $8\,\mu$m regions lie towards the southwest side of the region, the north and eastern edges are defined by a clear shell structure. There is a H II region on the northern shell that has a similar velocity to those of the brighter regions to the southwest. In addition, there appears to be a central component to the $8\,\mu$m emission in this complex at $(l,b) = (24.8°, 0.1°)$.
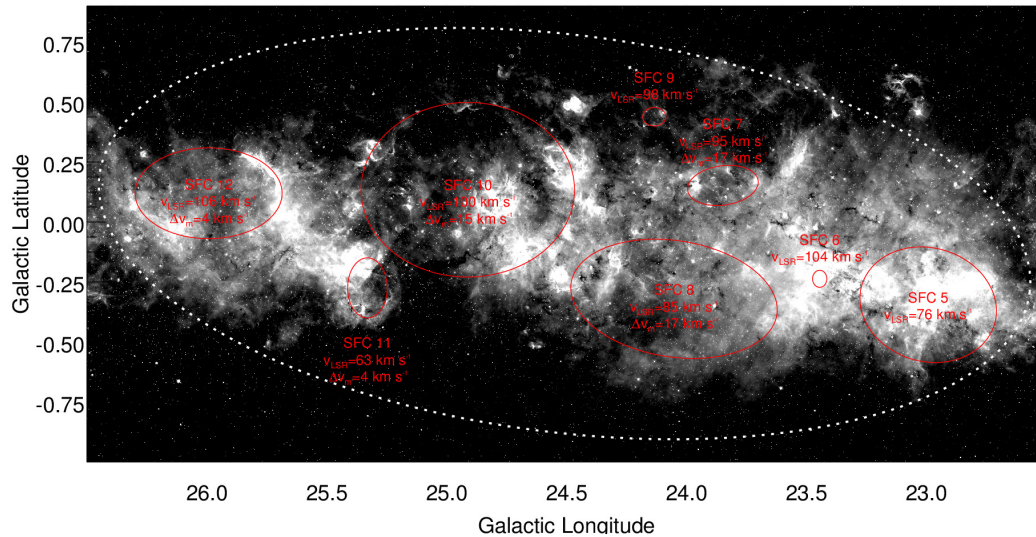
Figure 2.5: Same as Fig. 2.4, except the G24 regions are shown.

SFC 11 is associated with the W42 radio source but also includes an extended shell structure to the south and west of the original radio source with consistent velocity measurements along the shell. Lester et al. (1985) argue for the near galactic distance on the basis that there is minimal extinction towards the source in sulphur forbidden line emission, disregarding the known absorption velocities. Independent of the central source distance for the W42 region, an associated H II region at (l,b) = (25.41°, -0.25°) is also determined to be at the near kinematic distance (Kolpak et al. 2003), hence we adopt this distance. Blum et al. (2000) find a central cluster with a single O5-6.5 star, indicating that this is comparable to a cluster a few times the mass of Trapezium, rather than something particularly massive.

SFC 12 is a more extended complex outlined by a shell morphology its western edge. This bright 8 μm emission is associated with 2 similar H II region velocities. The overall size and shape of the complex is suggested by the shell-like structure visible in the southeastern edge, but additional H II velocity measurements are required to ensure this structure is associated with the known H II regions.

2.5.3   G30 including the W43 region

While G30 is also a large complex ($\sim$ 4° along the major axis, Figure 2.6), it is reasonably simple. We identify 6 star forming complexes within this WMAP source, SFC 13-18, but two are clearly dominant; SFC 17 associated with W43, and SFC 14.

SFC 17 consists of a bright central region with a shell outlined by a series of H II regions all at similar velocities. W43, located at (l,b) = (30.75°, -0.02°), lies inside SFC 17. This central region has been identified as a ministarburst region with the detection of a cluster of Wolf-Rayet and OB stars, undergoing a second generation of star formation through the submillimeter observations of massive young stellar objects (Motte et al. 2003; Lester et al. 1985; Blum et al. 1999). We identify a much larger shell surrounding this complex at similar radial velocities to the central complex. There is no obvious bubble associated with this SFC.

SFC 16, at (l,b) = (30.54°, 0.02°), is projected completely inside and is much smaller than SFC 17. However, SFC 16 is distinguished by a significantly different radial velocity (44 vs. 99 km s^{-1}), and consequently, a significantly different distance (11.9 kpc as compared to 6.3 kpc).

SFC 14 is located at a similar velocity to SFC 17, but is separated on the sky by an angle of $\sim$ 0.6° and it is located at the far distance (8.7 kpc) while SFC 17 is located at near distance (6.3 kpc). SFC 14 resides in the same 8 micron background as SFC 17. It is known to be forming stars, as it contains a hot molecular core and is associated with a molecular cloud (Olmi et al. 2003; Pratap et al. 1999).

The remainder of the star forming complexes within this WMAP source are low brightness sources in 8 μm emission and are not expected to contribute significantly to the total young stellar population.
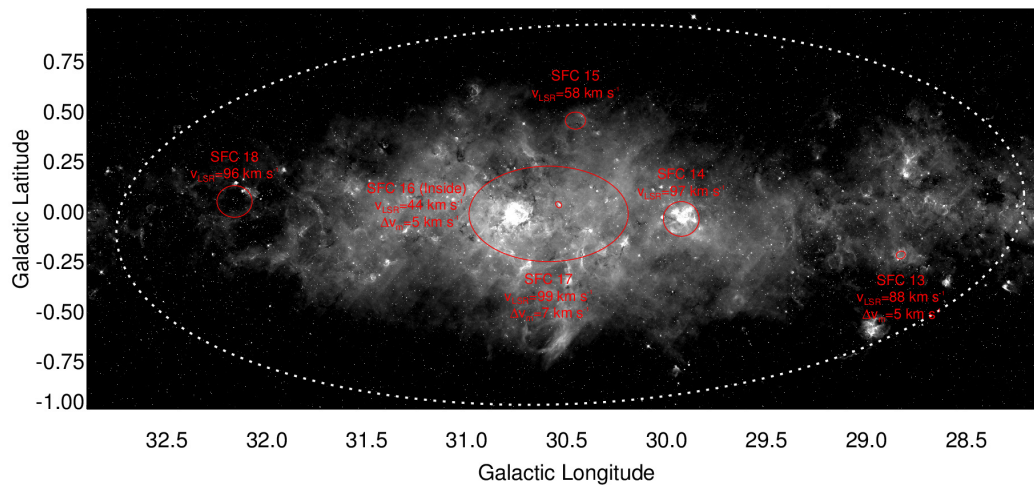
Figure 2.6: Same as Fig. 2.4, except the G30 regions are shown.

2.5.4 G34

We identify 3 well separated star forming complexes in G34, SFCs 19, 20 and 21 (Figure 2.7). The dominant complex is SFC 19, coincident with the majority of the background $8\,\mu$m emission in this area. At the heart of this star forming complex is the cometary H II region G34.3+0.2 (Reid & Ho 1985). Outside the inner 10 arcminutes of the radio source, we find three bubble structures (identified as bubbles 22, 23 and 24), indicating that this complex is composed of more than just the single O7V star assumed by Rodríguez-Rico et al. (2002).

SFC 21 is suggested primarily by its morphology, as only two H II region velocities are identified. The most prominent structure is on the east, where we identify a number of bubble-like objects. Our primary motivation in associating this large diffuse region together is the existence of structure all along the perimeter of the bubble, following the shell of the structure on the east. It is also possible that this complex consists of two separate star forming complexes, on the east and the west, but in that case it is unclear where the boundary between the two would be.
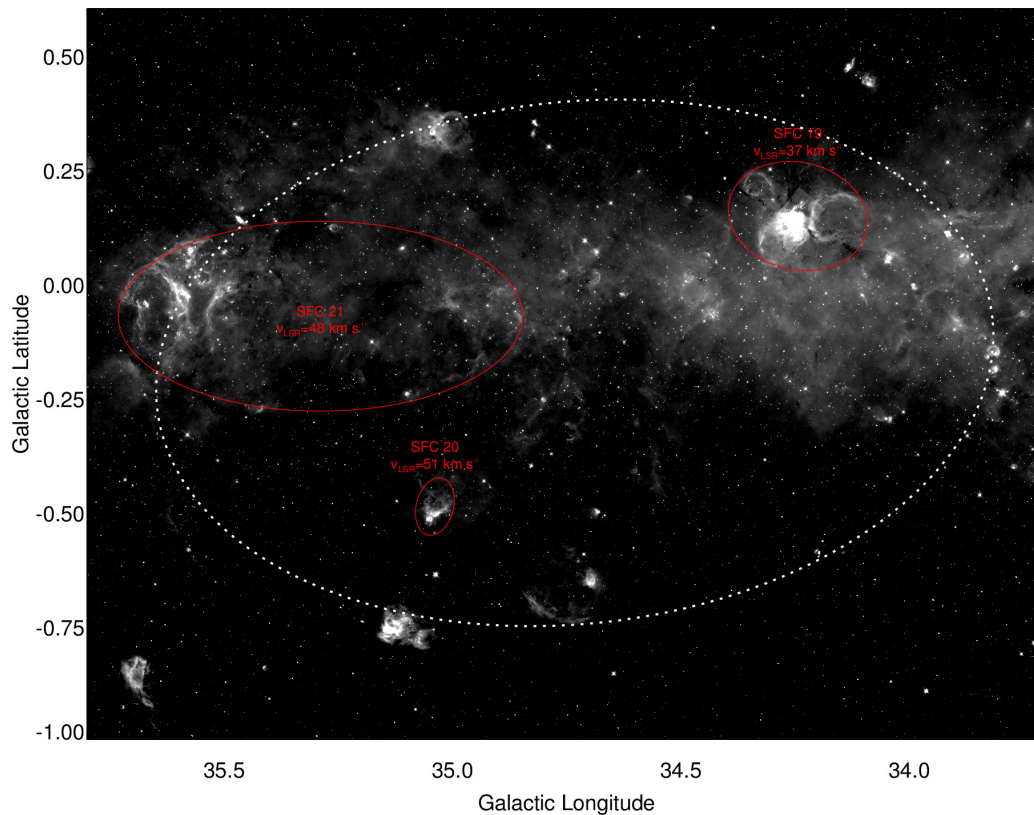
Figure 2.7: Same as Fig. 2.4, except the G34 regions are shown.

In MR10, this WMAP source was assigned a distance of 10.5 kpc taken from Russeil (2003); this is consistent with our present estimate to the distance to SFC 21. However, from the 8 μm emission evident in the Spitzer image, the majority of the free-free emission may well be coming from SFC 19, located at a distance of only 2.2 kpc. This would reduce the ionizing luminosity of the region dramatically.

2.5.5   G37 including the W47 region

Two star forming complexes have been identified in this WMAP region, both at similar velocities and exhibiting ring structure. SFC 22, which includes W47, is the larger source (Figure 2.8). There are 14 known H II regions, located in the upper half of

the bubble. While the southern shell is more diffuse, we do not classify this bubble as blown out, as a wall is still visible in the $8\,\mu$m emission. Much diffuse $8\,\mu$m emission is visible outside this region but specifically towards the brighter regions on the northern shell, implying that the majority of the emission is due to the triggered regions on the shell wall rather than a central source. This suggests that the complex is old. The uneven illumination of the shell structure further supports this assessment. W47, located on the northeastern shell of SFC 22, has not been extensively studied in the literature.

SFC 23 has similar radial velocities, but we are unaware of any resolution of the kinematic distance ambiguity in this case. A nearly circular shell structure is visible with a gap on the southeastern wall.

2.5.6 G49 including the W51 region

The complex containing WMAP source G49 is a well studied area owing to the presence of W51 (Figure 2.9). We identify two star forming complexes within this source. The chaotic structure in the $8\,\mu$m emission indicates that these complexes are particularly active and young. This chaotic structure makes it difficult to determine the actual shape and size of the star forming complexes. In the case of SFC 25, the shape is motivated by shell structure on the northwestern edge. For SFC 24, the shape is motivated by the distribution of H II regions. In both cases, we suspect that the true extent of the star forming complexes may be larger. The distances to these complexes are similar, 5.6 kpc for SFC 24 and 5.7 kpc for SFC 25. These distances are consistent with the distance of 5.1 kpc determined through trigonometric parallax to W 51 IRS2 (Xu et al. 2009). Ultimately, we have separated these complexes into two due to the separation of known H II regions into two clusters on the sky. The two complexes have previously been separated in the literature, where SFC 24 is labelled W51B and SFC 25 is W51A.
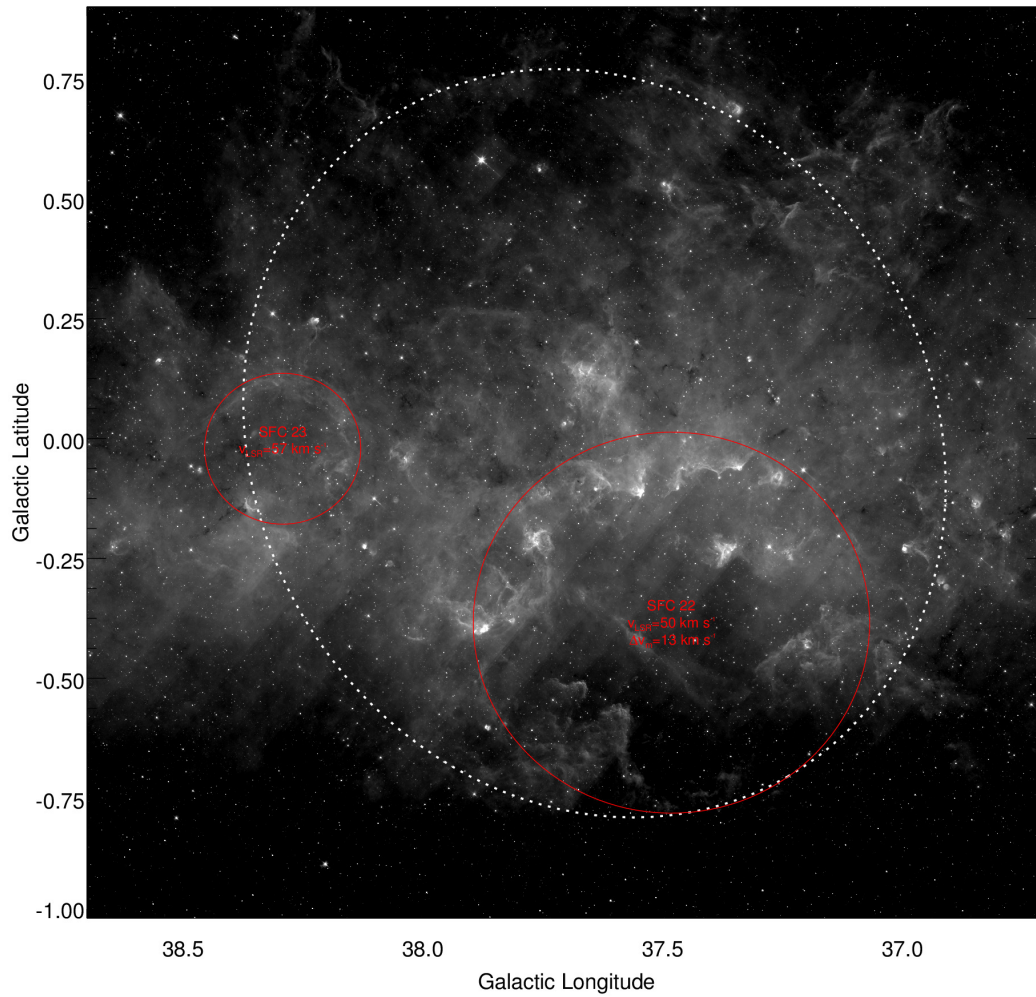
Figure 2.8: Same as Fig. 2.4, except the G37 regions are shown.

W51 is a well known star formation region (Kang et al. 2009). Conti & Crowther (2004) separate SFC 25 into W51A and W51 West, placing them at a similar distance of 5.1 kpc. They determine an ionizing luminosity for both these sources of $Q_0 = 1.01 \times 10^{51}$ from ground based observations of the free-free flux. For SFC 24, they determine an ionizing luminosity of $Q_0 = 1.07 \times 10^{50}$. Adjusting for the difference in the presumed distance, the total ionizing luminosity from the three Conti & Crowther sources accounts for a quarter of the ionizing luminosity determined from the entire WMAP source. This is not surprising; as we indicated in MR10, the bulk of the ionizing luminosity leaks beyond the more compact H II region defined by ground-based observations into the extended low density (ELD) region.

Figuerêdo et al. (2008) propose a smaller distance of 2.0 kpc to W51A based on the spectrophotometric distance of a number of O stars observed in the region, in contrast to the extensive kinematic and now trigonometric parallax distances determined. In the spectral classification of their target stars, there were unable to determine the luminosity class and argue for ZAMS based on the presence of ongoing star formation indicating a young region. However we have determined the dynamical age of the system to be two million years, which is sufficient for the most massive of stars to evolve off the main sequence. Further, the difference in the smaller and larger distances corresponds to a difference of 2 in magnitude, which in turn corresponds reasonably to the difference between the K-band magnitudes of a mid-to-late O star from luminosity class V to I (Martins & Plez 2006). Thus a more consistent story is that the identified stars are actually supergiants at the original distance of the source, 5.1 kpc.

2.5.7   G283 including the NGC 3199 and RCW 49 regions

We identify one star forming region, SFC 26, in WMAP source G283 (Figure 2.10). Unlike the complexes closer to the Galactic centre, there is little confusion in this
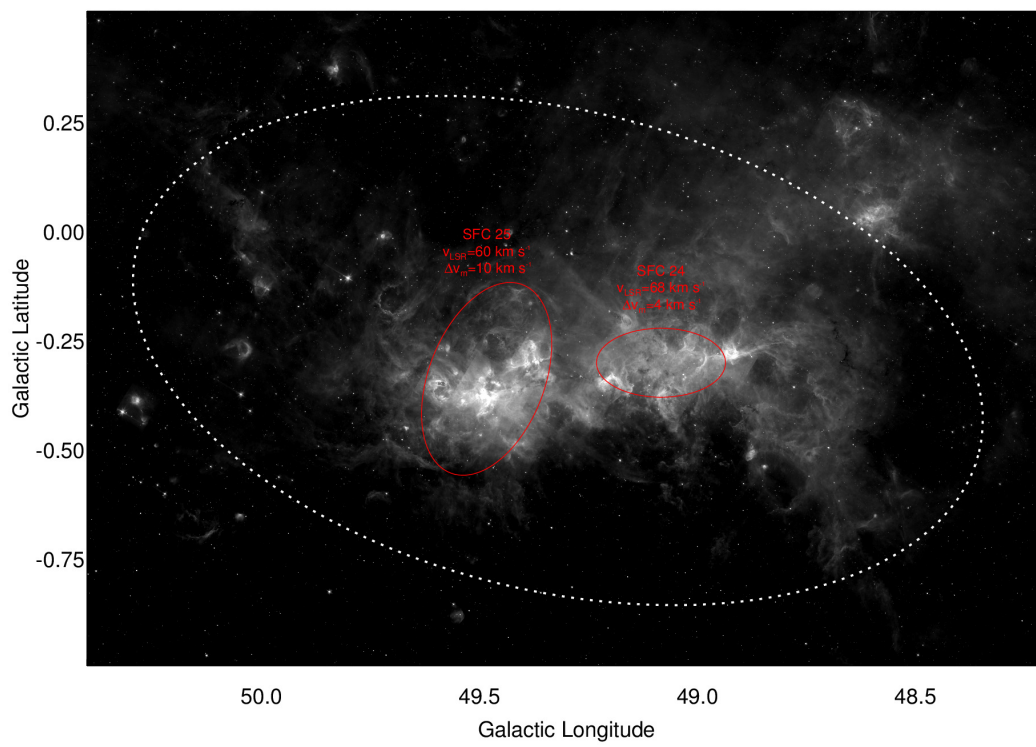
Figure 2.9: Same as Fig. 2.4, except the G49 regions are shown.

source. In fact, SFC 26 is similar in shape and size to the WMAP source. We use the MSX image in this complex as only the eastern edge of this source has been included in the GLIMPSE survey.

SFC 26 is associated with NGC 3199 and RCW 49, both known regions of active star formation. NGC 3199, located towards the southwest of the WMAP source, is associated with the Wolf-Rayet star WR 18 (Deharveng & Maucherat 1974). We know of no in-depth attempt to find a cluster in this region.

RCW 49 is located in the northeast half of the WMAP region and is associated with the brightest patch of $8\,\mu$m emission within the WMAP source. RCW 49 is a well known massive star forming complex with its embedded massive cluster Westerlund 2. For a review of this association, see §2 of Tsujimoto et al. (2007). Extensive surveys of the cluster have been completed in the infrared (Ascenso et al. 2007), and x-rays (Tsujimoto et al. 2007). Ascenso et al. (2007) find a total cluster mass of 7×10^3 M$_\odot$ using a distance of 2.8 kpc as compared to our distance of 4 kpc. This is a factor of four smaller than the estimate of the total stellar mass that we determine for the entire WMAP source using their distance. This indicates that a substantial number of stars associated with Westerlund 2 have evaded detection thus far and/or there is more than one substantial cluster associated with this star forming region.

2.5.8   G291 including the NGC 3603 and NGC 3576 regions

We find two overlapping star forming complexes associated with the WMAP source found at G291; SFC 27 and 28 (Figure 2.11). The separation of these two complexes is motivated by the substantial difference in H II velocities. In SFC 27, the mean velocity is $-22\,\mathrm{km\,s}^{-1}$ and extends to $-16\,\mathrm{km\,s}^{-1}$ while SFC 28 has a mean velocity of $16\,\mathrm{km\,s}^{-1}$ and extends to $9\,\mathrm{km\,s}^{-1}$. Note that the bright region associated with NGC 3576 at $(l,b) = (291.3°, -0.7°)$ in the shell of SFC 27 is projected to lie within SFC 28.
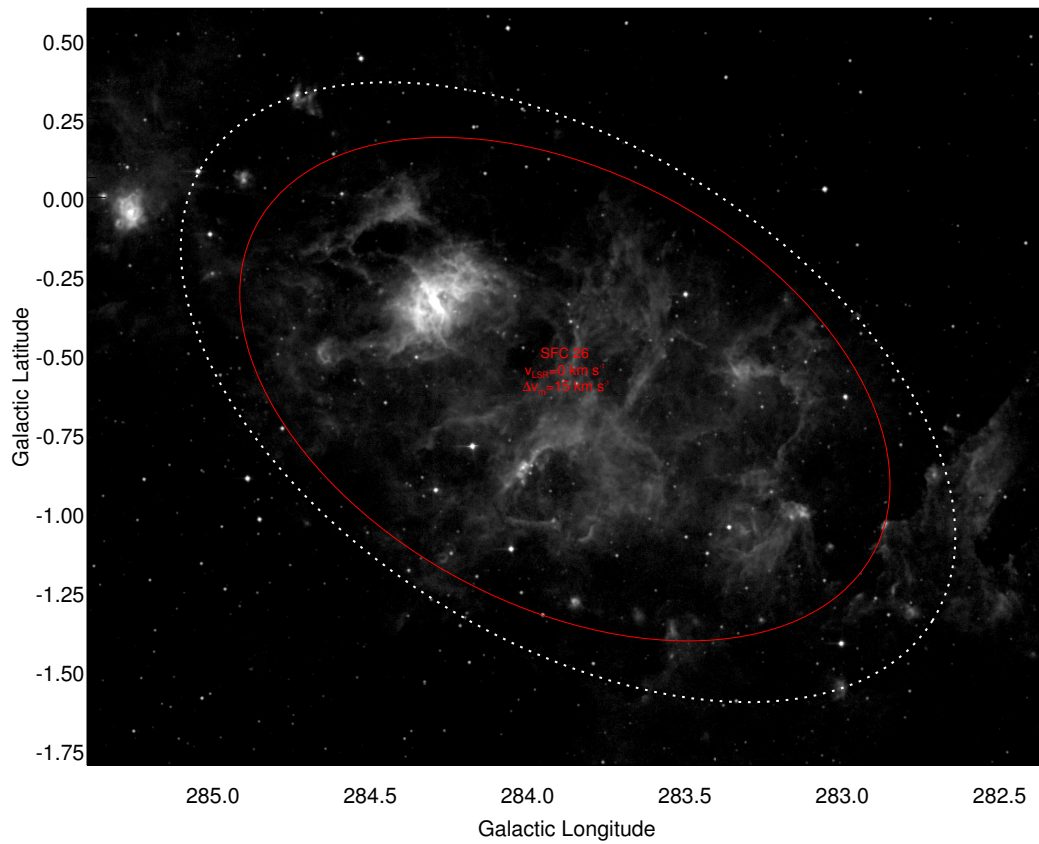
Figure 2.10: Same as Fig. 2.4, except the G283 regions are shown.

Persi et al. (1994) find a young massive cluster embedded in NGC 3576, detecting 40 cluster members with K band photometry. Barbosa et al. (2003) find a number of massive young stellar objects, indicating active star formation. NGC 3576 is located on the shell of the star forming region, suggesting that it may have been induced by a possible central cluster. This is consistent with the small size of the NGC 3576 region, indicating its youth.

SFC 28 is dominated by NGC 3603, located centrally within the region. Morphologically, it appears that material being swept up in the northwestern edge of the shell is triggering further star formation. This appears to also be the case at the location (l,b) = (291.1°, -0.75°), which happens to overlap SFC 27. NGC 3603 is a known massive star forming complex powered by HD 97950, often labelled a "starburst cluster"(for an extensive review see Melena et al. 2008). Conti & Crowther (2004) determine a total ionizing luminosity from NGC 3576 and NGC 3603 of $Q_0 = 3.4 \times 10^{51}$, similar to the ionizing luminosity for the entire WMAP source, $Q_0 = 4.2 \times 10^{51}$.

2.5.9 G298

G298 is an archetypal region of triggered star formation (Figure 2.12). We identify a single star forming complex associated with this WMAP source, SFC 29. In this star forming region, we see an evacuated bubble with a continuous shell in the $8\,\mu$m emission, with elephant trunk structures and three possible locations of triggered star formation on the rim of the bubble; on the northeast, northwest, and southwest. A great deal of $8\,\mu$m emission is coming from north of the source, consistent with UV photons leaking out of the central bubble and illuminating further material, with the majority of material being closer to the galactic midplane.

Conti & Crowther (2004) identify only the northeast and northwest shell regions which they identify at (l,b) = (298.227°, -0.340°) and (l,b) = (298.862°, -0.438°), with a total ionizing luminosity of $Q_0 = 1.5 \times 10^{51}$, which is substantially smaller than the
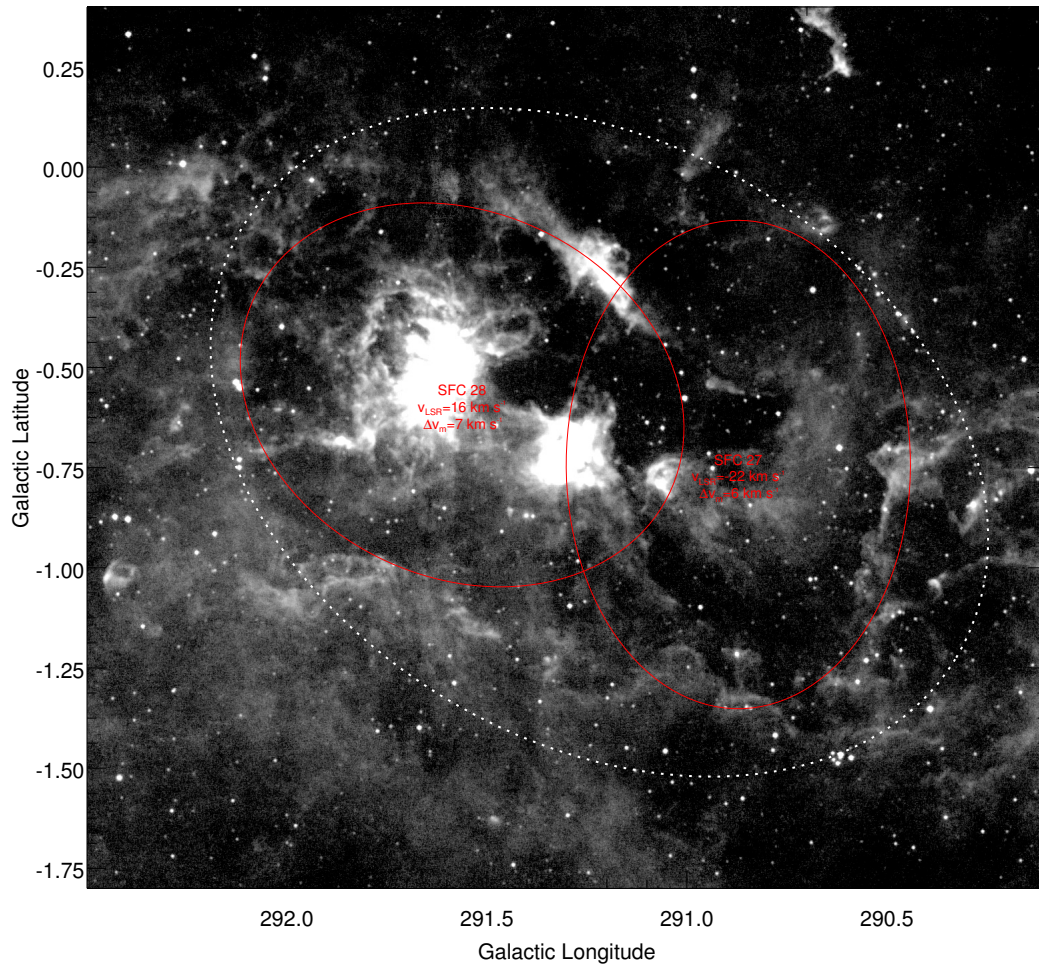
Figure 2.11: Same as Fig. 2.4, except the G291 regions are shown.
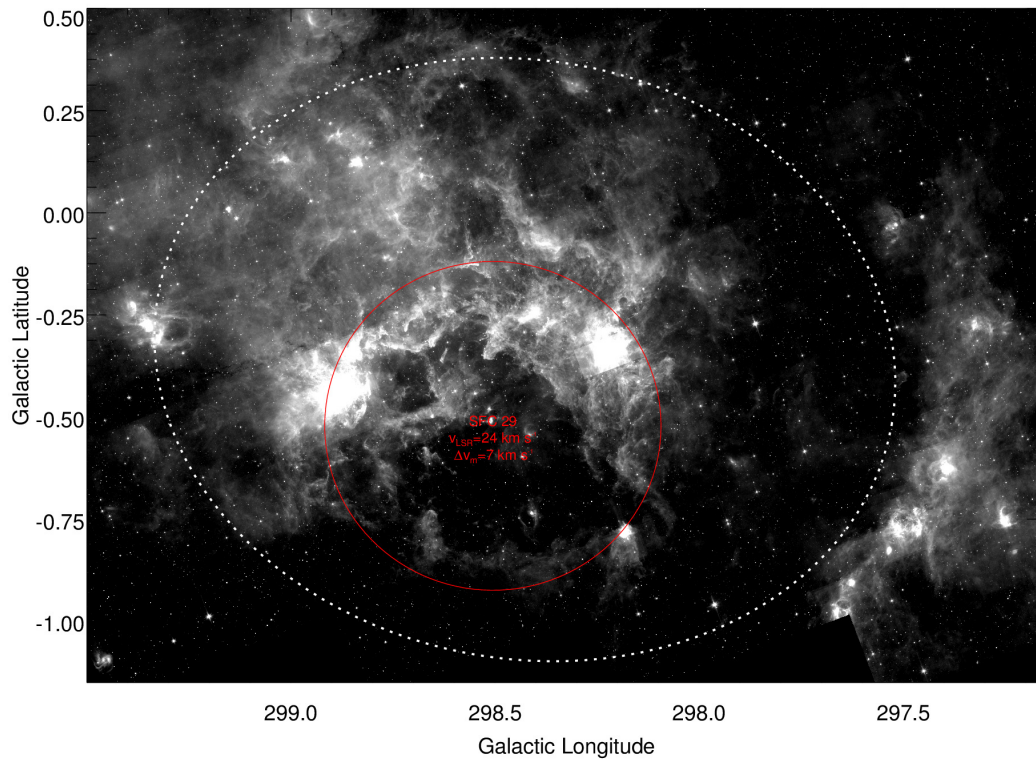
Figure 2.12: Same as Fig. 2.4, except the G298 regions are shown.

value we determine for the entire WMAP source, $Q_0 = 7.7 \times 10^{51}$. This larger ionizing luminosity implies that a truly massive cluster exists in this region, substantially larger than the two sources on the shell. Since this is the single, most luminous SFC in the Galaxy, we name and focus a search for the powering cluster in Chapters 3 and 4.

2.5.10 G311

The WMAP source G311 is a particularly large on the sky, stretching ~ 3 degrees along the Galactic plane, with a substantial $8\,\mu$m emission background (Figure 2.13). As this is a southern galactic plane source, it is not well studied, and we only identify three star forming complexes convincingly, one of which appears to be dominating this area in the sky.

SFC 31 is central to both the WMAP source and the background $8\,\mu$m emission and has a large angular size (nearly 0.5°). Further it is outlined through its shell morphology as well as the presence of multiple known H II regions along the shell. For these reasons, we infer that it is the dominant star forming complex within this WMAP source. SFC 30 is a much smaller region with a similar radial velocity measurement to SFC 31. However, the resolution of the kinematic distance ambiguity places SFC 30 at 3.5 kpc and SFC 31 at 7.4 kpc.

SFC 32 overlaps the southeastern edge of SFC 31, but is defined by H II regions having significantly different radial velocities, placing it much further away (13.6 kpc versus 7.4 kpc). There is a known supernova remnant located on the northwest edge of this shell (G311.5-0.3), which we associate with SFC 32 rather than SFC 31 due to its large distance of ~ 17 kpc derived from a surface brightness-distance relationship (Milne 1979).

The image shows a ridge in the $8\,\mu$m emission continuing from the southeast wall of SFC 31 strongly suggesting that this ridge is associated with the SFC. It is located from $(l,b) = (311.9°, -0.2°)$ to $(l,b) = (312.5°, 0.1°)$. However, there are no measured H II velocities for this feature, so we cannot confirm the association.

2.5.11   G327

All the H II region velocities in G327 lie within $\pm 13\,\mathrm{km\,s^{-1}}$ of each other, so we identify only one star forming region, SFC 33 (Figure 2.14). The morphology revealed by the $8\,\mu$m emission is rather complicated consisting of multiple bubbles. We interpret this complex as an example of cascading star formation; an instance where multiple generations of triggered star formation occur in sequence. We find a large, diffuse shell, outlined by the red ellipse in Figure 2.14, with a number of known H II regions along the wall. Towards the south and the southwest of the shell, there are two additional clear bubble-like structures, identified as bubble 39 and 38 in Table 2.3.
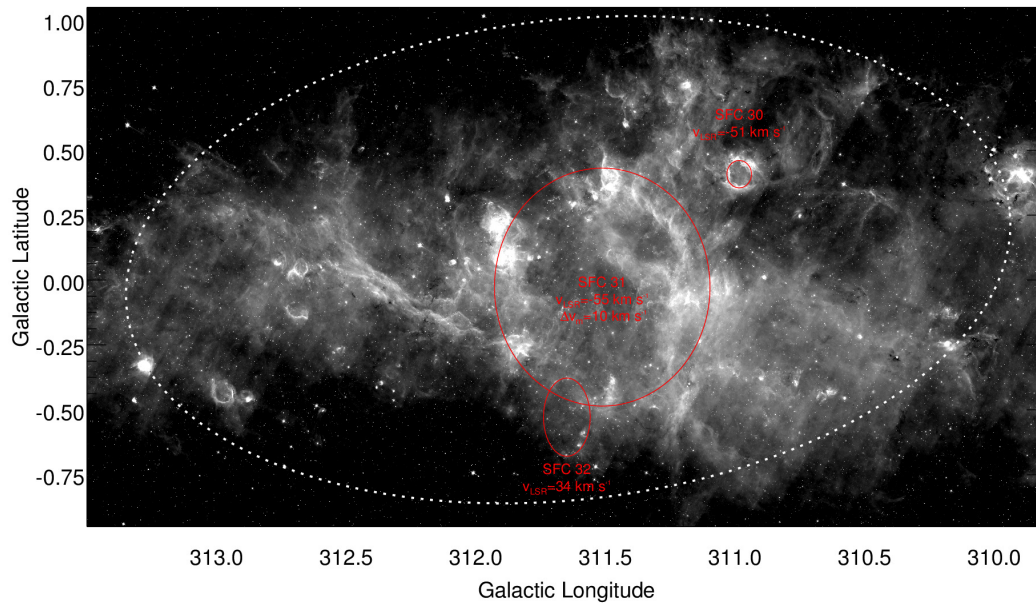
Figure 2.13: Same as Fig. 2.4, except the G311 regions are shown.

These both have additional H II regions visible on their walls. We interpret the largest complex as a shell produced by an older central cluster. We speculate that the two smaller (younger?) bubbles were formed from clusters that were triggered by the original central cluster. These, in turn, are now triggering a third generation of star formation.

A previously identified source, G327.3-0.6 (Wyrowski et al. 2006), lies at the southern edge of SFC 33. This author identifies H II regions, hot cores and cold clumps. There is evidence that G327.3-0.6 was triggered by the expansion of the bubble on the south rim of SFC 33 (Minier et al. 2009).

We suggest that an older massive cluster should exist towards the centre of SFC 33 and may be visible in infrared surveys, as this complex is not particularly distant (3.7 kpc).
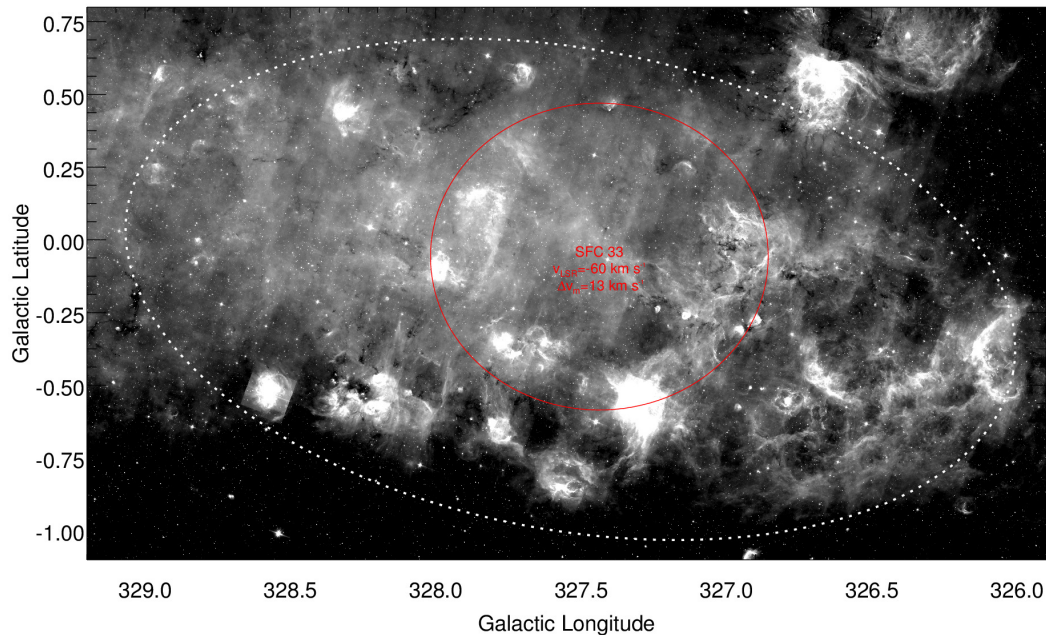
Figure 2.14: Same as Fig. 2.4, except the G327 regions are shown.

2.5.12 G332

G332 is another large WMAP source ($\sim$ 3 degrees) with only two distinct clusters in H II radial velocities (Figure 2.15). SFC 34 is the dominant star forming complex covering the majority of the WMAP source, while SFC 35 is a smaller complex projected to lie in the interior of SFC 34.

The Spitzer image of SFC 34 is dominated by $8\,\mu$m -bright regions along the southeastern edge. The bright southeastern ridge includes RCW 106 right at the southern edge of the complex to the region at $(l,b) = (333.6°, -0.2°)$. Conti & Crowther (2004) find three Giant H II regions associated with this complex, all with distances similar to our derived distance to SFC 34 ($\sim$ 3.4 kpc) with a total ionizing luminosity of $Q_0 = 5.0 \times 10^{50}\,\text{s}^{-1}$. From MR10, we associate an ionizing luminosity of at least $Q_0 = 5.0 \times 10^{51}\,\text{s}^{-1}$ to this SFC, implying that the majority of ionizing photons are escaping the compact H II regions. In addition, interactions between the known H II
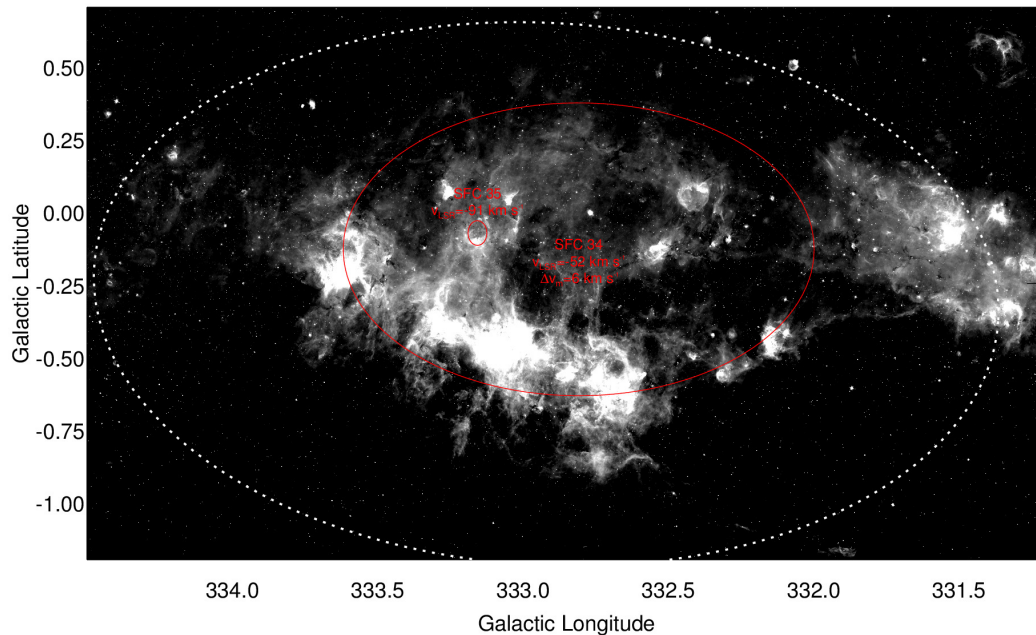
Figure 2.15: Same as Fig. 2.4, except the G332 regions are shown.

regions and its parent molecular cloud have been investigated by Bains et al. (2006).

2.5.13 G337

G337 is the widest WMAP source, spanning over 5 degrees in the Galactic plane (Figure 2.16). Five star forming complexes are identified, SFC 35-40. There is a very prominent background diffuse $8\,\mu$m emission which is difficult to associate with a specific SFC. Each of the star forming complexes are well separated both on the sky and by radial velocities. SFC 36, 38 and 40 lack strong central $8\,\mu$m emission suggesting that they have evacuated their surroundings. In contrast, SFC 37 and 39 show filled morphologies, suggestive of youth. SFC 39 is associated with a pulsar wind nebula and a gamma-ray source (Lemiere et al. 2009).

Table 2.2. Star Forming Complex Parameters

#	l (deg)	b (deg)	smaj (arcmin)	smin (arcmin)	PA (deg)	v_{LSR} (km s^{-1})	Δv_m (km s^{-1})	Δv_c (km s^{-1})	D (kpc)	$<R>$ (pc)	t_{dyn} (Myr)	KDA Ref.
1	10.156	-0.384	7.4	4.3	27	15	15	24	14.5	25	1.0	3
2	10.288	-0.136	6.8	4.4	89	10	...	...	15.2	25	...	3
3	10.450	0.021	3.3	2.4	54	69	...	...	6.1	5	...	1
4	10.763	-0.498	11.7	7.3	55	-1	...	...	16.7	46	...	1
5	22.991	-0.345	17.3	14.2	-16	76	...	...	4.9, 10.8	22, 49	...	...
6	23.443	-0.237	2.1	1.8	90	104	...	...	9.2	5	...	1
7	23.846	0.152	8.9	4.9	8	95	17	27	5.8, 9.8	12, 20	0.4, 0.7	...
8	24.050	-0.321	26.1	14.5	-9	85	17	24	10.3	61	2.6	3
9	24.133	0.438	2.9	2.3	0	98	...	...	5.9, 9.7	4, 7	...	...
10	24.911	0.134	26.7	21.8	0	100	15	21	6.1	43	2.1	3
11	25.329	-0.275	7.5	5.0	90	63	4	8	4.1	7	0.9	7
12	25.992	0.119	18.4	11.4	0	106	4	...	6.5, 8.8	28, 38	7.0, 9.5	...
13	28.827	-0.230	1.4	1.1	22	88	5	...	5.3	2	0.4	4
14	29.926	-0.049	5.4	5.2	0	97	...	...	8.7	13	...	1
15	30.456	0.443	3.0	2.6	0	58	...	...	3.6, 11	3, 9	...	...
16	30.540	0.022	1.0	0.8	-48	44	5	...	11.9	3	0.6	4
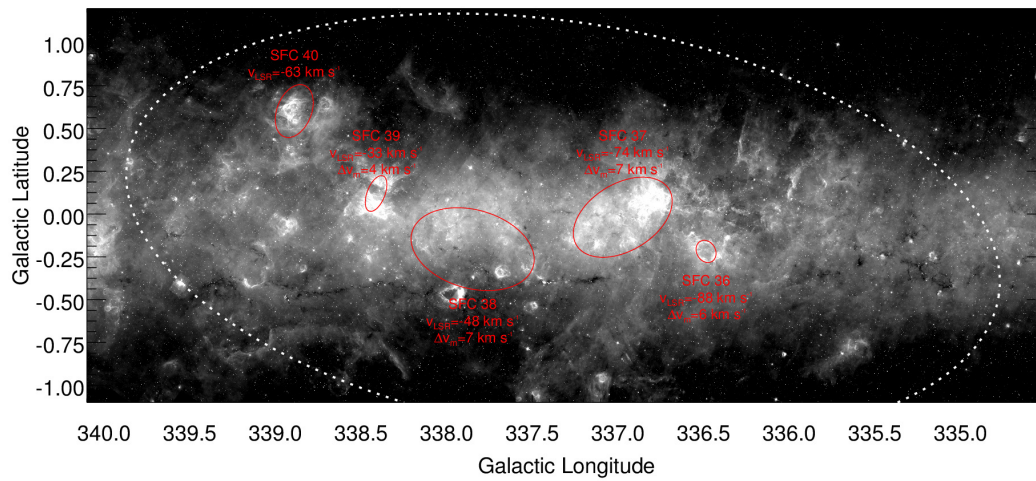
Figure 2.16: Same as Fig. 2.4, except the G337 regions are shown.

Table 2.2 (cont'd)

#	l (deg)	b (deg)	smaj (arcmin)	smin (arcmin)	PA (deg)	v_{LSR} (km s^{-1})	Δv_m (km s^{-1})	Δv_c (km s^{-1})	D (kpc)	$<R>$ (pc)	t_{dyn} (Myr)	KDA Ref.
17	30.590	-0.024	23.9	14.3	0	99	7	8	6.3	35	4.2	2
18	32.162	0.038	5.3	4.7	0	96	...	...	8.2	12	...	2
19	34.243	0.146	9.2	7.1	-13	37	...	...	2.2	5	...	2
20	35.038	-0.490	3.8	2.4	76	51	...	...	3	3	...	1
21	35.289	-0.073	26.6	12.5	0	48	...	...	11	62	...	2
22	37.481	-0.384	24.8	23.8	0	50	13	17	10.5	74	4.4	2
23	38.292	-0.021	9.8	9.4	0	57	...	...	3.5, 9.9	10, 28	...	...
24	49.083	-0.306	8.9	4.7	0	68	4	6	5.6	11	2.0	...
25	49.483	-0.343	13.9	8.0	69	60	10	13	5.7	18	1.4	...
26	283.883	-0.609	66.6	41.3	-28	0	15	20	4	63	3.2	5
27	290.873	-0.742	36.6	25.8	90	-22	6	10	3	27	2.8	...
28	291.563	-0.569	34.4	27.4	-25	16	7	11	7.4	67	6.3	...
29	298.505	-0.522	24.7	24.2	0	24	7	11	9.7	69	6.2	...
30	310.985	0.409	3.2	2.8	90	-51	...	...	3.5	3	...	6
31	311.513	-0.027	27.5	25.0	90	-55	10	13	7.4	56	4.3	6
32	311.650	-0.528	9.0	5.4	90	34	...	...	13.6	29	...	...

Table 2.2 (cont'd)

#	l (deg)	b (deg)	smaj (arcmin)	smin (arcmin)	PA (deg)	v_{LSR} (km s^{-1})	Δv_m (km s^{-1})	Δv_c (km s^{-1})	D (kpc)	$\langle R \rangle$ (pc)	t_{dyn} (Myr)	KDA Ref.
33	327.436	-0.058	34.9	31.7	0	-60	13	17	3.7	36	2.1	6
34	332.809	-0.132	48.6	30.2	0	-52	6	7	3.4	39	5.9	6
35	333.158	-0.076	2.5	1.9	90	-91	⋯	⋯	5.5, 9.7	4, 6	⋯	⋯
36	336.484	-0.219	4.1	3.3	-60	-88	6	10	5.4, 10.2	6, 11	0.6, 1.2	⋯
37	336.971	-0.019	19.0	11.8	31	-74	7	10	10.9	49	5.0	6
38	337.848	-0.205	22.1	13.8	-16	-48	7	9	3.5	18	2.0	6
39	338.412	0.120	6.6	3.1	68	-33	4	4	2.5, 13.3	4, 19	1.0, 4.8	⋯
40	338.888	0.618	10.1	6.9	25	-63	⋯	⋯	4.4	11	⋯	6

References. — (1) Churchwell et al. (1990); (2) Kuchar & Bania (1994); (3) Sewilo et al. (2004); (4) Palagi et al. (1993); (5) Wilson et al. (1970); (6) Caswell & Haynes (1987); (7) Kolpak et al. (2003)

Note. — The KDA Ref indicates the source by which the kinematic distance ambiguity is resolved. In cases where no reference is given, the kinematic distance is either unique or we present the near and far distances.

Table 2.3.   Bubble-like Objects Associated with the Star Forming Complexes

#	l (deg)	b (deg)	smaj (arcmin)	smin (arcmin)	PA (deg)	Associated SF Complex	<R> (pc)	Classification Flag	GLIMPSE Bubble
1	10.316	-0.137	1.6	1.2	50	2	6.1	C	⋯
2	10.763	-0.498	11.7	7.3	55	4	46	B	N2
3	23.703	0.166	0.3	0.3	66	7	0.5, 0.9	C	⋯
4	23.873	-0.114	0.6	0.4	-76	8	1.5	C	⋯
5	23.880	-0.350	0.4	0.3	69	8	1.0	C	⋯
6	23.904	0.070	0.4	0.4	90	7	0.7, 1.2	C	N32
7	24.050	-0.321	26.1	14.5	-9	8	61	C	⋯
8	24.095	0.456	0.8	0.7	-52	9	1.3, 2.1	C	⋯
9	24.133	0.438	2.9	2.3	0	9	4.5, 7.3	B	⋯
10	24.505	0.240	5.4	3.1	-50	10	7.5	B	N35
11	24.840	0.106	4.6	2.1	-64	10	5.9	B	N36
12	25.292	0.296	2.2	1.5	90	10	3.3	B	N37
13	25.323	-0.293	5.4	5.4	0	11	6.4	B	⋯
14	25.992	0.119	18.4	11.4	0	12	28, 38	B	⋯
15	26.112	-0.030	2.4	2.0	0	12	4.2, 5.6	B	⋯
16	28.827	-0.230	1.4	1.1	22	13	1.9	C	N49
17	30.456	0.443	3.0	2.6	0	15	2.9, 9.0	C	⋯
18	30.612	-0.194	11.0	5.8	0	17	15	B	⋯
19	30.736	-0.022	3.0	2.1	-36	17	4.7	C	N52
20	32.098	0.090	1.0	0.8	-43	18	2.1	C	N55
21	32.159	0.039	4.6	4.0	0	18	10	C	⋯
22	34.156	0.145	3.8	2.6	11	19	2.0	B	N61
23	34.296	0.077	2.0	1.9	90	19	1.2	B	⋯
24	34.331	0.213	1.7	1.5	-38	19	1.0	B	N62
25	35.002	-0.130	5.1	3.2	-68	21	13	B	⋯
26	35.032	-0.482	1.6	1.4	54	20	1.3	B	⋯
27	35.259	0.119	0.5	0.4	-28	21	1.5	C	N66
28	35.642	-0.059	5.8	2.9	-75	21	14	C	N68
29	37.481	-0.384	24.8	23.8	0	22	74	B	⋯
30	38.293	-0.015	8.1	7.4	0	23	7.9, 22	B	N71
31	38.352	-0.133	1.0	0.9	0	23	1.0, 2.8	B	N72
32	298.218	-0.323	2.4	1.7	90	29	5.8	C	S181
33	298.527	-0.562	18.5	14.7	-51	29	47	C	⋯

Table 2.3 (cont'd)

#	*l* (deg)	*b* (deg)	smaj (arcmin)	smin (arcmin)	*PA* (deg)	Associated SF Complex	<R> (pc)	Classification Flag	GLIMPSE Bubble
34	310.985	0.409	3.2	2.8	90	30	3.1	C	S137
35	311.487	0.401	2.5	1.7	12	31	4.6	B	S133
36	311.495	-0.013	24.2	17.7	-72	31	45	B	⋯
37	311.916	0.222	2.2	1.4	-73	31	3.9	C	⋯
38	326.882	-0.389	13.1	8.0	-66	33	11	B	⋯
39	327.532	-0.605	14.9	14.1	0	33	16	B	⋯
40	333.158	-0.076	2.5	1.9	90	35	3.6, 6.3	B	⋯
41	336.484	-0.219	4.1	3.3	-60	36	5.8, 11	C	⋯
42	336.778	0.089	2.9	2.4	-20	37	8.4	B	⋯
43	336.853	-0.016	1.6	1.2	82	37	4.5	B	⋯
44	336.887	0.059	2.7	1.6	0	37	6.8	B	⋯
45	336.921	-0.195	2.2	1.9	-70	37	6.4	C	⋯
46	337.153	-0.178	1.8	1.6	68	37	5.4	B	⋯
47	337.676	-0.335	2.1	1.8	35	38	2.0	C	S37
48	338.891	0.596	3.7	3.0	-55	40	4.3	B	S29

Note. — The classification flag refers to the morphology of the bubble: 'C' indicates that the bubble is a closed bubble and 'B' refers to a broken bubble.

The GLIMPSE bubble column indicates the identification of this bubble in Churchwell et al. (2006) with the catalogue number.

2.6 Discussion

It has been noted before that complexes with elevated free-free emission are associated with elevated $8\,\mu$m emission (Cohen & Green 2001; Murray & Rahman 2010). In MR10, we used this correlation to argue that, based on the higher resolution $8\,\mu$m images, both the free-free and $8\,\mu$m emission are powered by a central source. In this chapter, we have shown that bubbles are associated with all of the sources we have examined. The bubbles are identified by their bright rims as seen in $8\,\mu$m emission.

In addition, the bubbles are surrounded by an elevated background of $8\,\mu$m emission. The total luminosity in the $8\,\mu$m band of our WMAP sources is dominated

Table 2.4. H II Region Velocities

Associated Star Forming Complex	Name	l (deg)	b (deg)	v_{LSR} (km s^{-1})	Reference Number
1	[L89b] 10.073-00.412	10.0732	-0.4119	13.6	1
$\cdots$	GRS 010.20 -00.30	10.1467	-0.3377	13	2
$\cdots$	[WMG70] 010.2-00.3	10.149	-0.343	14.2	3
$\cdots$	PMN J1809-2019	10.1589	-0.3489	14.2	1
$\cdots$	GAL 010.2-00.3	10.1615	-0.3546	12.8	4
$\cdots$	[L89b] 10.190-00.426	10.1898	-0.426	36.2	1
$\cdots$	[L89b] 10.190-00.426	10.1898	-0.426	5.4	1
2	[WC89] 010.30-0.15B	10.303	-0.1462	7.7	5
$\cdots$	GAL 010.32-00.16	10.3148	-0.15	13.1	4
3	GAL 010.46+00.02	10.458	0.0239	70.1	1
$\cdots$	GAL 010.46+00.03	10.4625	0.034	68.9	4
$\cdots$	GAL 010.47+00.03	10.4722	0.0264	68	6
4	GAL 010.6-00.4	10.6205	-0.3872	0.2	7
$\cdots$	[SG70] 010.6-0.4	10.6258	-0.383	0.4	8
$\cdots$	[KC97c] G010.7-00.5	10.6639	-0.4666	-2.4	1

References. — (1) Lockman (1989); (2) Anantharamaiah (1985a); (3) Wilson et al. (1970); (4) Bronfman et al. (1996); (5) Kim & Koo (2001); (6) Wood & Churchwell (1989); (7) Wink et al. (1982); (8) Lockman et al. (1996); (9) Quireza et al. (2006); (10) Kolpak et al. (2003); (11) Caswell (1972); (12) Wink et al. (1983); (13) Pestalozzi et al. (2005); (14) Kuchar & Bania (1994); (15) Walsh et al. (1997); (16) Rodríguez-Rico et al. (2002); (17) Caswell & Haynes (1987); (18) Georgelin & Georgelin (1970); (19) Russeil et al. (2005); (10) Ikeda et al. (2001); (21) Gardner & Whiteoak (1978); (22) Caswell et al. (1975); (23) Downes et al. (1980)

Note. — Table 2.4 is published in its entirety with the article Rahman & Murray (2010) in the electronic edition of the Astrophysical Journal. A portion is shown here for guidance regarding its form and content.

by the elevated background as opposed to the high-surface brightness emission from the bubble walls. We conclude that the bulk of the ionizing photons from the central source escape through the bubble walls to reach distances of 100-200 pc or more, confirming the results of MR10.

Previous estimates of stellar masses associated with giant H II regions have been underestimates of the total stellar mass at those locations. This follows from the fact that the H II regions reprocess only a small fraction of the ionizing photons in a given WMAP source.

We suggest that massive clusters inhabit the central regions of the complexes. These clusters have evaded detection due to the lack of high surface brightness H II or radio continuum emission. We suggest that this results from a lack of gas and PAH particles in the immediate vicinity of the young clusters. The clusters have evacuated their surroundings, leaving little material to reprocess the ionizing photons emitted by the cluster.

2.6.1   Scale Height of O Stars

As discussed above, the WMAP sources studied in this chapter are expected to contain approximately one-third of the O stars in the Galaxy. Using those objects in our catalogue with unique distances, we estimate the scale height of the O stars. As a first approximation, we assume that each of the star forming complexes contain a similar number of O stars. Using this assumption, we construct the cumulative distribution function of star forming complexes as a function of their height above the galactic plane. The scale height of the distribution is

$$h_* = 35 \pm 5 \text{pc}. \tag{2.1}$$

This value is consistent with that obtained by Elias et al. (2006) for the local galactic disk (within 1 kpc) of $h_{\text{LGD}} = 34 \pm 3$ pc for their O-B2 subsample. Both are smaller

than the value obtained by Reed (2000) of $h_{\rm LGD} = 45 \pm 20$ pc for all OB stars within a distance of 4 kpc, but easily fall within their error bars. We note that the scale height of the molecular gas is $h \sim 40$ pc (Malhotra 1994), and the scale height of the GLIMPSE bubbles is $h = 40$ pc if the population is assumed to be at an average distance of 4 kpc (Churchwell et al. 2006).

2.6.2 Free-Free to $8\,\mu{\rm m}$ Emission Relationship

A morphological correlation has been established between the MSX 8 micron emission and the radio continuum (Cohen & Green 2001). We investigate this correlation using the WMAP free-free emission maps and the $8\,\mu$m emission from the GLIMPSE 8 micron mosaics. For each WMAP source, we summed the free-free emission from the inside the Source Extractor ellipse from MR10. We summed the $8\,\mu$m from the same ellipse in the Spitzer GLIMPSE mosaic. The result is shown in Figure 2.17. From a least-square fit, we find the following relationship:

$$F_{8\,\mu{\rm m}} \propto F_{\rm ff}^{1.1\pm0.34} \tag{2.2}$$

where $F_{8\,\mu{\rm m}}$ is the integrated 8 micron GLIMPSE flux and $F_{\rm ff}$ is the integrated 90 GHz free-free emission from the WMAP free-free foreground emission map. We find a similar relationship using the MSX Band A integrated flux in place of the GLIMPSE measurements.

We note that while the $8\,\mu$m emission may be caused both by PAH emission as well as warm dust continuum emission, the total flux in the $8\,\mu$m band is dominated at large radii rather than the small, bright areas towards individual H II regions (MR10, Figure 7). As such, we infer that the driver of this relationship is the PAH emission and not the warm dust emission. While this correlation is strong, the physical meaning behind it remains an open question.
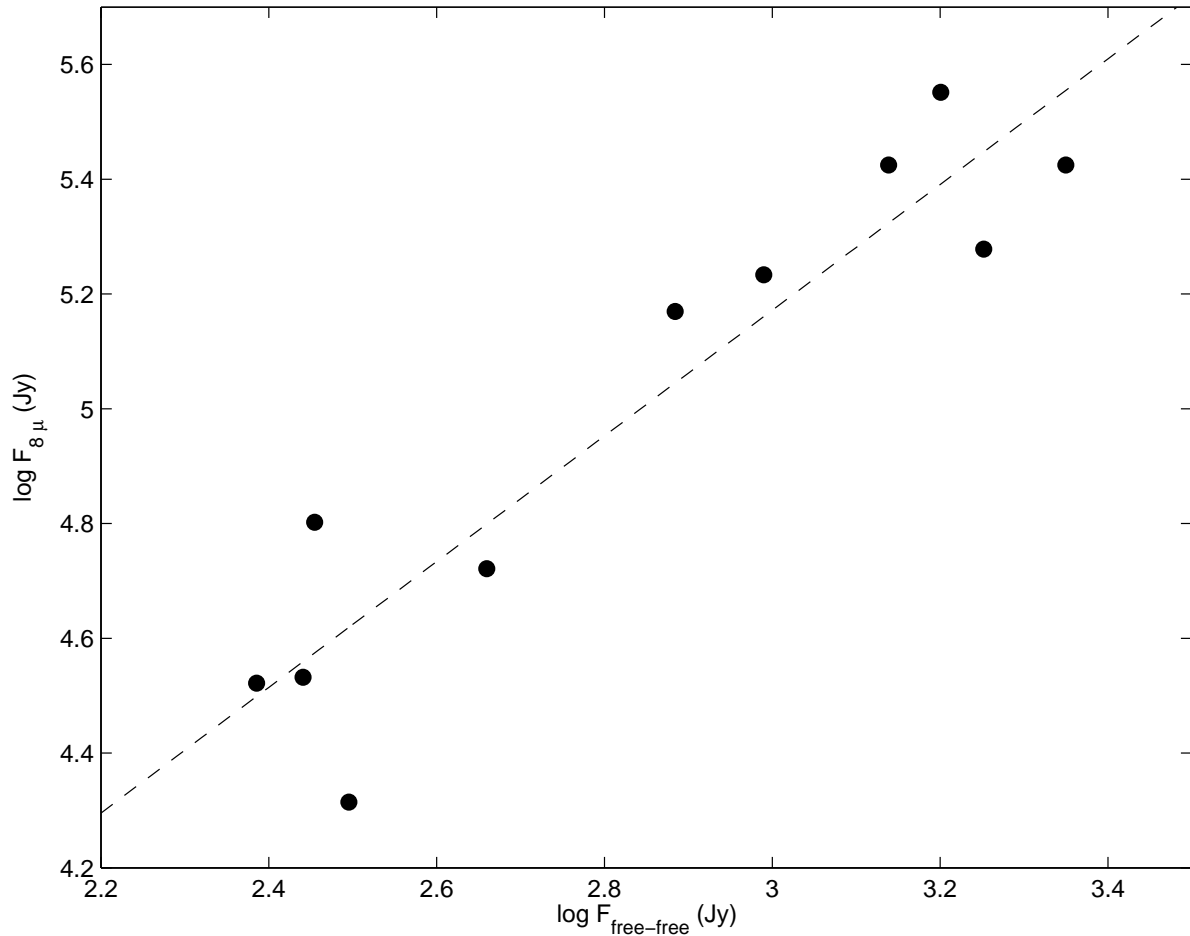
Figure 2.17: The comparison between the total flux integrated over the complexes presented in Table 2.1 in free-free emission through the WMAP free-free foreground emission map at 90 GHz, and in $8\,\mu$m emission taken through the GLIMPSE 8 micron mosaics. The slope of the best fit line is 1.1 ± 0.3. Complexes without GLIMPSE coverage are excluded from this plot.

We caution against the use of this relationship without any physical insight, especially to extragalactic regions. Calzetti et al. (2007) find that $8\,\mu$m emission is a poor tracer of the star formation rate due to sensitivity to metallicity, size and star formation history. Consequently, we warn against the use of this relationship as a calibration of the star formation rate.

2.6.3 Velocity Dispersion of the Molecular Gas

Both molecular and atomic gas in the disk of the Milky Way are seen to have supersonic velocity dispersions. These dispersions are normally interpreted as being due to turbulence, although their origin is uncertain. If the motions are due to turbulence, they must be driven, since undriven turbulence decays on roughly a dynamical time (Mac Low et al. 1998). Furthermore, the turbulence must be driven on 100 pc scales, since three dimensional turbulence cascades from large scales to small scales and not the other way around. A number of driving mechanisms have been proposed (Mac Low & Klessen 2004; Miesch & Bally 1994), including supernovae, stellar winds, and gravitational instabilities, with no conclusive evidence for any particular mechanism. We investigate the kinetic energy that is injected into the ISM by the expansion of the massive complexes that we identify. We note that all of the star forming complexes we have identified are likely to be in giant molecular clouds—a preliminary search shows that more than thirty are in fact in molecular clouds.

We calculate the mechanical luminosity in the expansion of each of the star forming complexes using

$$L_{mech} = \frac{\pi}{2}\Sigma_0 \Delta v_c^3 r,\tag{2.3}$$

where $\Sigma_0 = 170 M_\odot\ \mathrm{pc}^{-2}$ (Solomon et al. 1987) is the surface density of a GMC, and r and Δv_c are taken from Table 2.2. For SFCs where the half-spread velocity was not measured, we used the mean half-spread velocity, $\Delta v = 12$ km s^{-1}, of the known sources. For cases where the kinematic distance remains ambiguous, we take the mean

radius of the complex determined from both the near and far distances. Since the ratio of the two distances is less than two, this introduces an error of less than a factor of two for 9 out of our 40 SFCs. For each of the SFCs, we present the calculated dynamical properties in Table 2.5 with the columns as follows: column (1) the catalogue number, column (2) the mass swept up in the shell in solar masses, column (3) the kinetic energy of the swept up shell in erg, and column (4) the mechanical luminosity produced by the motion of the shell in erg s^{-1}.

The total mechanical luminosity being injected into the ISM inside the solar circle due to the expansion of these SFCs is the sum of the individual luminosities. We limit ourselves to the radius of the solar circle as all of the SFCs are located either at or within the solar circle, and thus will not be injecting mechanical luminosity into the medium outside of this radius. We find

$$L_{mech} \approx 6.7 \times 10^{38} \left(\frac{\Sigma_0}{170 M_\odot \, \mathrm{pc}^{-2}} \right) \, \mathrm{erg \, s}^{-1}. \tag{2.4}$$

This sum encompasses only one-third of the star formation in the Galaxy. The other two-thirds should supply a proportionate amount of mechanical luminosity, for a total kinetic luminosity of $\sim 2 \times 10^{39} \, \mathrm{erg \, s}^{-1}$.

We compare this luminosity to that required to maintain the velocity dispersion in the molecular gas within the the solar circle:

$$L_{turb} \equiv \frac{1}{2} \frac{M v^3}{2h}, \tag{2.5}$$

where $h = 40$ pc is the scale height of the molecular disk, the molecular gas mass inside the solar circle $M = 1.0 \times 10^9 M_\odot$, and a molecular gas velocity $v = \sqrt{2 \ln 2} \sigma_{mol}$ with $\sigma_{mol} = 7 \, \mathrm{km \, s}^{-1}$ (Malhotra 1994). The turbulent luminosity is

$$L_{turb} \approx 2.4 \times 10^{39} \left(\frac{v}{8 \, \mathrm{km \, s}^{-1}} \right)^3 \, \mathrm{erg \, s}^{-1}. \tag{2.6}$$

We conclude that the mechanical luminosity we see in the bubbles, multiplied by a factor of three to account for the other two thirds of Galactic star formation, is

similar to the turbulent luminosity seen in the molecular gas. This suggests that the expansion of bubbles within the identified SFCs may eventually dissipate and be a significant energy source driving the turbulent motions of the molecular gas disk.

Despite the similarities in the mechanical and tubulent luminosities, there exist a number of challenges to this explanation of the velocity dispersions. First, the mechanical luminosities measured are coming from the coherent expansion motion of the shells within the SFCs. For the energy in the expansion to drive the velocity dispersion, the fluid motions must cascade from ordered to random at a high efficiency. Further, the mechanical luminosity will be injected into the molecular material surrounding the SFC and not distributed throughout the molecular disk. Consequently, the energy will be injected into a small fraction of the molecular material and will not be able to drive turbulence in the regions outside of the SFCs. However, the similarity between the mechanical and turbulent luminosities indicate that this mechanism is likely to contribute some energy to the turbulent motions and this point merits further investigation.

We note that the kinetic energies calculated for most of the bubbles (refer to Table 2.5) range from 10^{48} to just below 10^{52} erg s^{-1}. The kinetic energies of our most energetic bubbles are similar to those measured in the superbubbles identified by Heiles (1979), which range from 4×10^{51} erg s^{-1} to 2×10^{53} erg s^{-1}.

We note that our bubbles are selected by their ionizing luminosity, i.e., we require a very young stellar population. In addition, we do not see significant synchrotron radiation from these areas, indicating the absence of supernova remnants. This implies that the clusters are too young to have had more than a few supernova explode, and many of our sources likely have not had any supernovae go off. We infer that the superbubbles in the Galaxy are not initially driven by the energy from supernovae, but rather by the energy injected into the medium by the massive stars during their lifetime. It may well be, however, that supernovae contribute significantly to the

kinetic energy later in the evolution of a superbubble.

Table 2.5.   Dynamical Properties of the Star Forming Complexes

SFC #	log M_{sh} ($M_\odot$)	log E_k (erg)	log L_{mech} (erg s^{-1})
1	4.9	50.7	37.8
2	4.9	50.1	36.9
3	2.8	48.0	36.2
4	5.7	50.9	37.2
5	5.4	50.5	37.1
6	2.9	48.1	36.2
7	4.3	50.2	37.7
8	6.1	51.8	38.1
9	2.9	48.1	36.2
10	5.6	51.3	37.8
11	3.3	48.1	35.8
12	5.3	49.5	35.6
13	1.6	46.0	34.6
14	4.1	49.3	36.6
15	3.1	48.2	36.3
16	2.2	46.6	34.8
17	5.4	50.2	36.6
18	4.0	49.1	36.6
19	2.9	48.0	36.2
20	2.0	47.2	35.9
21	6.1	51.3	37.3
22	6.3	51.8	37.8
23	4.6	49.7	36.8
24	3.9	48.3	35.5
25	4.5	49.7	36.8
26	6.1	51.7	37.9
27	5.0	50.0	36.6
28	6.2	51.2	37.1
29	6.2	51.3	37.2
30	2.2	47.3	36.0
31	6.0	51.2	37.3
32	5.1	50.3	37.0
33	5.4	50.8	37.5

Table 2.5 (cont'd)

SFC	log M$_{sh}$	log E$_k$	log L$_{mech}$
#	(M$_\odot$)	(erg)	(erg s^{-1})
34	5.5	50.1	36.3
35	2.8	48.0	36.2
36	3.5	48.5	36.1
37	5.8	50.8	36.9
38	4.5	49.4	36.4
39	3.9	48.1	35.1
40	3.8	49.0	36.5

2.6.4   Bubbles: Spherical Shells or Flattened Rings?

The three-dimensional geometry of the bubbles identified by Churchwell et al. (2006) has been contested recently. Beaumont & Williams (2010) propose that Churchwell et al.'s bubbles are flattened rings. Beaumont & Williams (2010) suggest that the aspect ratios of these rings may be anywhere from a few to as much as 10. Nineteen of our forty-eight bubbles are in the GLIMPSE bubble catalogs. We test the assertion of Beaumont & Williams (2010) statistically using the bubbles in Table 2.3.

We model our bubbles as ellipsoids, following the procedure of Noumeir (1999) with semi-axes a, b, c aligned along the x, y and z axes such that $a \geq b \geq c$. The matrix equation for the ellipsoid is

$$u^\mathsf{T} X u = 1 \tag{2.7}$$

where u is an arbitrary position vector. The matrix X is a diagonal matrix with entries a^2, b^2, c^2, corresponding to the semi-axes of the ellipsoid. We rotate the ellipsoid along the z-axis by an angle θ, and along the y-axis by an angle ϕ, producing the matrix

$$X' = \begin{bmatrix} \alpha \cos^2 \phi + c^2 \sin^2 \phi & \beta \cos \phi \cos \theta \sin \theta & (c^2 - \alpha) \sin \phi \cos \phi \\ \beta \cos \phi \cos \theta \sin \theta & a^2 \sin^2 \theta + b^2 \cos^2 \theta & -\beta \sin \phi \cos \theta \sin \theta \\ -(\alpha + c^2) \sin \phi \cos \phi & -\beta \sin \phi \cos \theta \sin \theta & \alpha \sin^2 \phi + c^2 \cos^2 \phi \end{bmatrix} \tag{2.8}$$

where we define $\alpha = a^2 \cos^2\theta + b^2 \sin^2\theta$, and $\beta = a^2 - b^2$.

To determine the observed ellipse on the sky resulting from the rotation of the ellipsoid, we produce an orthographic projection of the ellipsoid onto the y-z plane. The resulting projection is

$$X_P = \begin{bmatrix} a^2 \sin^2\theta + b^2 \cos^2\theta & -\beta \sin\phi \cos\theta \sin\theta \\ -\beta \sin\phi \cos\theta \sin\theta & \alpha \sin^2\phi + c^2 \cos^2\phi \end{bmatrix} \tag{2.9}$$

To minimize the observed axis ratio, we assume the bubbles are circular rings with $a = b$, implying the semi-major axis of the projected bubble is a, and the projected semi-minor axis is $\sqrt{a^2 \sin^2\phi + c^2 \cos^2\phi}$. The resulting axis ratio, a function of only the rotation along the y-axis, is given as

$$R_{ax}(\phi) = \frac{a}{\sqrt{a^2 \sin^2\phi + c^2 \cos^2\phi}} \tag{2.10}$$

We compute the expectation value of the axis ratio $\langle R_{ax}(a/c) \rangle$, for $a/c = 10$ and $a/c = 4$. Using eqn. (2.10) we find $\langle R_{ax}(10) \rangle = 2.4$ and $\langle R_{ax}(4) \rangle = 1.8$. We compare this to our sample of 48 bubbles, for which we find $\langle R_{ax} \rangle = 1.3 \pm 0.3$, suggesting that the intrinsic aspect ratio $a/c \lesssim 4$ at the two sigma level. In fact $\langle R_{ax} \rangle = 1.3$ corresponds to a mean intrinsic aspect ratio $a/c = 1.7$.

A more sensitive test is that of the maximum aspect ratio; the maximum observed aspect ratio is 2.2, corresponding to a maximum inclination angle of $31°$ from the face-on position of a ring with $a/c = 4$. For a random distribution of inclination angles weighted by the metric in spherical coordinates, we would expect 48%, or 23 ± 7 of the bubbles to have an aspect ratio greater than 2.2.

We note that if the observed maximum aspect ratio (2.2) is in fact the true mean aspect ratio, then $\langle R_{ax}(2.2) \rangle = 1.4$, consistent with the observed mean aspect ratio. We note further that if flattened shells do exist in the regions analyzed, we would see bright linear structures in the $8 \, \mu$m images with the length of order the diameter of the observed bubbles. We do not see any such features in the images.

We note that the bubbles in our sample are on average much larger than the bubbles found by Beaumont & Williams (2010). In the case of these larger bubbles discussed here, we find an insufficient number of observed bubbles with large aspect ratios to support the geometry of a flattened ring and the original picture of nearly-spherical shells is more likely to be physically correct.

2.7 Summary

From an analysis of the 13 most luminous sources found in the WMAP free-free emission map, we have identified 40 star forming complexes using a combination of morphology in $8\,\mu$m emission from the Spitzer GLIMPSE and MSX surveys and velocities of known H II regions at the same location on the sky. For all 31 of the 40 complexes we are able to determine a unique distance associated with the radial velocity measurements, allowing us to determine the physical size of these complexes. For 20 of these star forming complexes, there are a sufficient number of H II region velocity measurements to estimate the expansion speed of the complex and consequently, a dynamical age.

We catalogue 48 bubble-like objects, 19 of which have been previously catalogued by Churchwell et al. (2006). For most of these bubbles, we were able to determine a physical size. We also present a comprehensive list of the radio recombination line velocity measurements associated with each star forming region.

We discuss each of the WMAP sources individually, commenting on the morphology within the source. Many of the northern sky star forming complexes are associated with previously identified star forming complexes. In most cases, the previous masses (or luminosities) for embedded clusters are substantially underestimated, as earlier studies often did not take into account the leakage of ionizing photons from the central ionizing source. We also find substantial evidence of triggered star formation in many of the star forming complexes. A number of our star forming complexes, especially

the southern sky complexes, have not been previously investigated or identified as possible locations of massive stellar clusters.

We determine the scale height of the Galactic O stars to be $h_* = 35 \pm 5\,\mathrm{pc}$, consistent with previous values for the scale height of OB stars in the local galactic plane. We determine a strong empirical relationship between the total integrated $8\,\mu\mathrm{m}$ and free-free emission; $F_{8\,\mu\mathrm{m}} \propto F_{\mathrm{ff}}^{1.1}$.

We show that the kinetic energy injected per unit time into the galactic medium by the expansion of the star forming complexes is similar to that required to maintain the velocity dispersion seen in the Galactic molecular gas. Thus we propose that the expansion of the star forming complexes is a primary driver of turbulence in the molecular gas of the Galaxy. We further show that the kinetic energy of the identified bubbles is similar to that of known superbubbles, implying that superbubbles are being produced before any supernova activity has taken place within the cluster.

Finally, we show that the three dimensional geometry of the bubbles is more consistent with a nearly-spherical shell rather than a flattened ring geometry based on statistics of the identified sample.

Chapter 3

A Candidate for the Dragonfish Association

A preliminary version of this chapter was published as:

"A Candidate for the Most Luminous OB Association in the Galaxy"

Rahman, M., Matzner, C.D., & Moon, D-S., 2011, The Astrophysical Journal Letters, 728, 37

3.1   Chapter Overview

The Milky Way harbors giant H II regions which may be powered by star complexes more luminous than any Galactic OB association known. Being across the disk of the Galaxy, however, these brightest associations are severely extinguished and confused. We present a search for one such association toward the most luminous H II region in the recent catalog by Murray and Rahman, which, at ~9.7 kpc, has recombination rate of $\sim 7 \times 10^{51}$ sec^{-1}. Prior searches have identified only small scale clustering around the rim of this shell-like region, but the primary association has not previously been identified. We apply a near-infrared color selection and find an overdensity of point sources toward its southern central part. The colors and magnitudes of these excess

sources are consistent with O- and early B-type stars at extinctions $0.96 < A_K < 1.2$, and they are sufficiently numerous (406 ± 102 after subtraction of field sources) to ionize the surrounding H II region, making this a candidate for the most luminous OB association in the Galaxy. We reject an alternate theory, in which the apparent excess is caused by localized extinction, as inconsistent with source demographics.

3.2 Introduction

Very massive OB associations are objects of intense interest. Given that the association birthrate ($\dot{\mathcal{N}}_{\mathrm{cl}}$) is observed to vary with association mass (M_{cl}) as $d\dot{\mathcal{N}}_{\mathrm{cl}}/d\ln M_{\mathrm{cl}} \propto 1/M_{\mathrm{cl}}$ (McKee & Williams 1997), or possibly slightly flatter, a large portion of each galaxy's star formation occurs within its most massive OB associations. Giant OB associations are most capable of disrupting their gaseous environment, from their natal molecular clouds to the entire galactic neighborhood, and they inflate superbubbles which erupt from the disk, feeding a galactic halo or fountain. They sculpt and illuminate the giant H II regions seen in distant galaxies and are a notable feature of starburst evolution. Being the most extreme examples of intense star formation in the current universe, they are laboratories for the physics of star cluster formation such as environmental influences on the initial mass function, formation of very massive stars, and dynamical evolution with rapid stellar evolution.

Although several of the brightest known OB associations within the Milky Way approach 'super star cluster' status ($M > 10^4 M_\odot$, Portegies Zwart et al. 2010), it is possible that even more luminous associations have escaped detection because of severe extinction and confusion in the Galactic plane. For instance, the Galactic OB associations with the largest known ionizing output, S, are those powering the NGC 3603 H II, Arches, Quintuplet, and Galactic Center regions ($\log S/\mathrm{s}^{-1} \simeq 51.5, 51.0, 50.9$, and 50.5, respectively: Figer 2008; Conti & Crowther 2004); however, the upper

limit of the Milky Way association distribution is estimated to be even brighter ($\log S_u/\mathrm{s}^{-1} \simeq 51.7$; McKee & Williams 1997).

In Chapter 2[1], we identified 40 star-forming complexes within the 13 most luminous ($S > 3 \times 10^{51}$ s^{-1}) free-free emission regions observed by WMAP and catalogued by Murray & Rahman (2010). Many of these complexes are potential hosts to embedded super star clusters. Of particular interest is the most luminous unconfused star-forming complex located at (l, b) = (298.4,-0.4) with a kinematic distance of 9.7 kpc. With an output of $\log S/\mathrm{s}^{-1} \simeq 51.8$, the stars powering this region may represent the Milky Way's most luminous OB association. (We refer to this region and its cluster as G298 or, inspired by its 8 μm appearance, as the 'Dragonfish Nebula': Figure 3.1.) The region appears in 8 μm as a closed bubble surrounded by a prominent shell. Previous searches using near-infrared (NIR) point source catalogs from 2MASS (Dutra et al. 2003) and Spitzer GLIMPSE (Mercer et al. 2005) have concentrated on the brightest regions of free-free emission around the shell and relied on integrated source counts. Although some clustering was discovered in these studies (Figure 3.2), the central ionizing association is yet undiscovered.

In this Chapter, we identify a candidate for the central OB association powering the Dragonfish, primarily by applying a color selection to the 2MASS catalogue. Our candidate is potentially the most luminous (and thus massive) OB association in the present Milky Way.

3.3   Feasibility and Methods

Only very luminous stars of deeply embedded OB associations are visible due to distance and extinction. Whether the association can be identified using the 2MASS point source catalogue (Skrutskie et al. 2006) depends on the OB association radius

---

[1]Published as Rahman & Murray (2010)
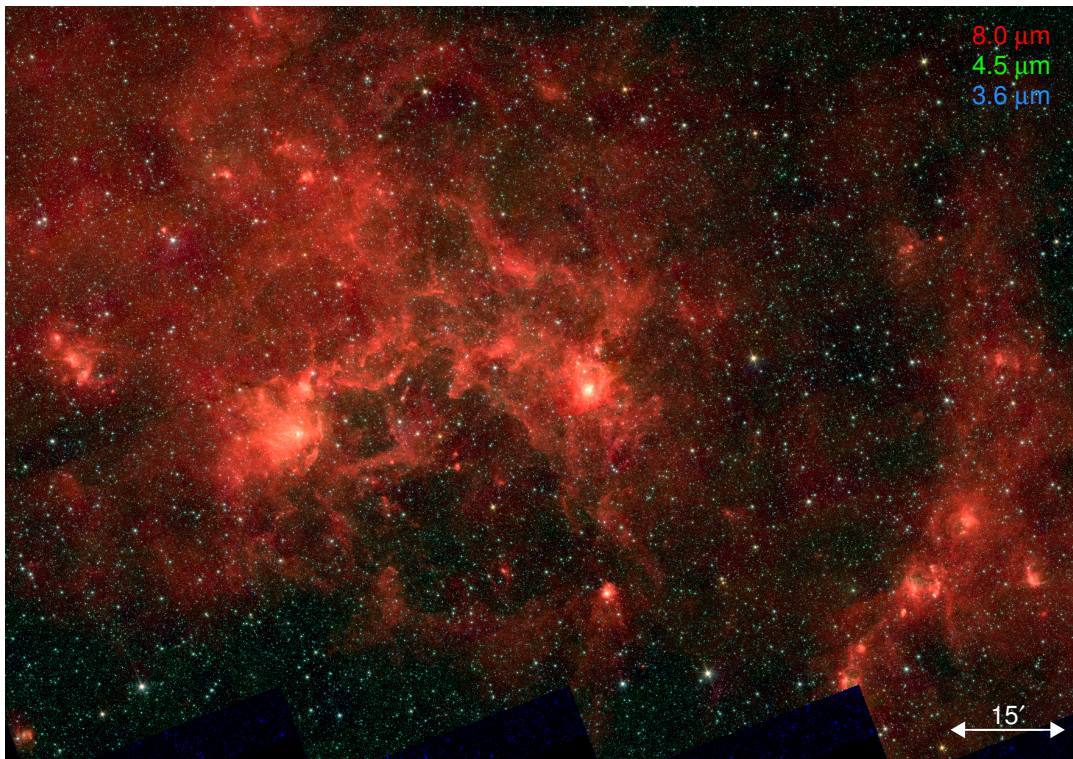
Figure 3.1: G298 or the Dragonfish region seen in the Spitzer GLIMPSE 3.6 (blue), 4.5 (green) and 8.0 (red) μm bands (Benjamin et al. 2003).

and field star density.

Radii in the range 10–30 pc are likely since most associations, irrespective of mass, are disrupted immediately after birth (Roberts 1957). OB association birthsites in the Milky Way have a limited range of mass column densities, $\Sigma \simeq 0.3\,\mathrm{g\,cm^{-2}} \pm 0.5\,\mathrm{dex}$ (Fall et al. 2010). Using the definition of the turbulent virial parameter (from McKee & Zweibel 1992), turbulent linewidths in these birthsites are $\sigma = 5\alpha^{1/2}[(0.5/\varepsilon)(\Sigma/.3\,\mathrm{g\,cm^{-2}})M_5]^{1/4}\,\mathrm{km\,s^{-1}}$, for associations of mass $10^5\,M_5\,M_\odot$ which form with efficiency ε from a region with turbulent virial parameter α. Crossing and formation timescales are both shorter than the ionizing lifetime and the terminal expansion speed of an OB association is likely to be $\sim \sigma$. For an association of $\sim 10^5 M_\odot$, an age between 2–4 Myr, and an expansion speed between 4–6 $\mathrm{km\,s^{-1}}$, we therefore expect an expanding population currently 8–24 pc in radius, possibly surrounding a dense core which survived the disruption event. For a physical radius $R = 10(R/10\mathrm{pc})$ pc with the ionizing luminosity of the Dragonfish as measured from WMAP, the association source density is $10(R/10\mathrm{pc})^{-2}\,\mathrm{arcmin^{-2}}$. We measure the 2MASS source population density in the Galactic plane to be $14 - 17\,\mathrm{arcmin^{-2}}$. For $R < 8$ pc the association dominates raw 2MASS source counts, whereas for $R > 10$ pc it is a minor variation of the 2MASS population which is difficult to detect using raw source counts.

The NIR color information provides an additional avenue to search for the embedded associations. We make use of this in the search for the embedded association within the Dragonfish. Ionization from a coeval stellar population drops sharply after 4 Myr as its most massive and powerful stars turn off the main sequence, so it is unlikely, though not impossible, that G298's ionizing population is any older. The ionizing population is sufficiently rich ($S > 10^{50}\,\mathrm{s^{-1}}$: Kennicutt et al. 1989) to fully sample the stellar initial mass function (IMF); its very massive stars should still be present and visible.

The association is likely highly extinguished, even if it has cleared its natal cloud. At a distance of 9.7 kpc the fiducial distance-extinction relationship within the Galactic disk, $A_V/D \simeq 1.6\,\text{kpc}^{-1}$ (Binney & Merrifield 1998), predicts $A_V \simeq 16$; this corresponds to a K_s-band extinction $A_{K_s} \simeq 1.0$ (Nishiyama et al. 2008). We adopt the Nishiyama et al. (2009) extinction law, which is steeper than that of Cardelli et al. (1989). We rely primarily on the 2MASS point source catalog for our analysis, but use three additional data sets to check for consistency: the USNO-B catalog of visible magnitudes, the Spitzer GLIMPSE catalog at 3.6 and 4.5 μm, and deeper J and H band photometry of a small section of the candidate.

For our search, we target main-sequence, massive stars, at a distance of $\sim$ 9.7 kpc and an extinction of around $A_K \simeq 1$. Further, association members visible in all three bands have spectral types of roughly B1 or earlier, so their intrinsic emission in the NIR bands ($\lambda \sim 1.0 - 2.4\,\mu$m) is entirely in the Rayleigh-Jeans limit (($J - H, H - K) = (-0.11, -0.10)$; Martins & Plez 2006). With the predicted extinction, NIR colors should be $(J - H, H - K) \simeq (1.1, 0.5)$. Association sources should lie in a tight group along the reddening vector from this common initial color. If the upper IMF follows the Salpeter (1955) slope to an upper limit of 120 $M_\odot$, we expect $\sim 400 \times 10^{-0.34(A_K-1.0)}(\text{D}/9.7\,\text{kpc})^{1.16}$ members with confident NIR colors ($[J, H, K_\text{s}] < [15.9, 15.0, 14.3]$, for which the signal-to-noise ratio exceeds five in all bands). Note that if the association is older than 4 Myr or is not coeval, it must be even more numerous because more stars are required to make up for the missing ionization from the top of the main sequence.

The first steps of our analysis are to select sources with the color of an early-type star behind a range of extinctions bracketing the expected value, to test for a statistically significant overdensity within the confines of the 8 μm bubble, and then to vary the adopted extinction range in order to optimize the statistical significance of the overdensity. In practice we determine source density using the angular offset θ_N

between a source and its Nth neighbour, as $\Sigma_* = N/(\pi\theta_N^2)$, and use $N \sim 20 - 100$ to reduce Poisson noise at some expense in resolution. Once the angular scale of the putative association is determined, we assess its significance by comparing source density within this region to the mean $\bar{\Sigma}_*$ and standard deviation σ_Σ of those within independent, identically-sized regions in a 2-degree field centered on, but excluding, the 8 μm bubble. Statistical significance is measured by $(\Sigma_* - \bar{\Sigma}_*)/\sigma_\Sigma$.

Once a candidate is identified, we check that the same procedure applied to regions outside the 8 μm bubble yields no candidates of similar significance. We then examine the color-color and color-magnitude diagrams (CCDs and CMDs) of similarly-sized regions to check that an apparent overdensity is not caused by features of the distribution of stars and extinction.

3.4 Results

3.4.1 Candidate OB Association

Based on the expected source colors from § 3.3, we apply a NIR color cut of $1.0 < J - H < 1.4$ and $0.44 < H - K_s < 0.62$, corresponding to colors of hot stars with $0.9 < A_K < 1.2$. Within the color cut, the 2-degree diameter field encompassing the Dragonfish has a mean stellar density $\bar{\Sigma}_* = 1.4$ arcmin^{-2}, which we refer to as the field star density. The standard deviation of Σ_* averaged over association-sized regions is $\sigma_\Sigma = 0.30$ arcmin^{-2}. We find a significant overdensity of stars in the Dragonfish Nebula at $(l, b) = (298.55, -0.72)$, located inside the shell of the star forming complex (Figure 3.2). This overdensity is not evident in the field star density of all point sources in 2MASS (Figure 3.3). In Figure 3.4, we present the field star density maps of a series of extinction cuts, showing the appearance of the overdensity at the chosen colour cut, and its absence in the others.

The 1–σ stellar overdensity contour ($\Sigma_* = \bar{\Sigma}_* + \sigma_\Sigma$) has semimajor and semiminor

axes (11′, 10′), corresponding to (31, 28)pc; however, the association may extend beyond the observational limit. The peak of the overdensity is $\Sigma_* = 3.7$ arcmin^{-2}, 8-σ above the background level on cluster-sized regions, adopting the 100th nearest neighbor. The region contains 897 sources within the adopted boundaries. Subtracting the contribution due to background sources, the candidate association is composed of 406 ± 102 sources, consistent with the value determined based on the chosen IMF and measured luminosity (§ 3.3). Using the 1–σ boundaries, the mean density of the association is $\Sigma_* + 4.0\sigma_\Sigma$. We refer to the candidate as the "Dragonfish Association".

The association is strongly concentrated within the central 4.1′, but contains an extended asymmetric envelope. The central, dense, symmetrical region has a stellar density which depends as $\theta^{-\alpha}$ with $\alpha = 0.44 \pm 0.03$ for $2' < \theta < 3'$, where the value of α depends on the assumed density of field sources. At larger radii the azimuthally averaged density drops more rapidly, but is dominated by the asymmetries visible in Figure 1. Half the excess sources are found within 4.7′, or $13\,(D/9.7\text{kpc})$ pc, similar to the half-light radii of other Galactic OB associations (Portegies Zwart et al. 2010).

Assuming half the projected mass falls within this radius, and assigning a total mass of $10^5\,M_\odot$ we infer that the association's central regions are older than their virial crossing times, whereas its outskirts are not ($T_{cr} = 22$ Myr). It therefore seems likely to be unbound on the whole (Gieles & Portegies Zwart 2011) but to contain a bound core; however this bears further investigation.

Using the USNO and Spitzer GLIMPSE catalogues, we are able to confirm that the stars identified in the Dragonfish Association have magnitudes and colors consistent with OB stars with the stated extinction, but not further able to distinguish the association population from the background. In the GLIMPSE wavelengths ($> 3\,\mu$m), this is because nearly all stars have identical, Rayleigh-Jeans colors, whereas with the USNO wavelengths ($< 1\,\mu$m), the spectral energy distribution is strongly dominated by the extinction. Thus template colors of most stellar types can be fit to the additional

photometry by varying the assumed distance or extinction of the star.

3.4.2 Color-Color and Color-Magnitude Diagrams

The NIR color information provides an additional avenue to determine important parameters of the candidate association, including the statistical significance of the overdensity, the possible background contributors, and the color variation of all point sources within the association boundaries. Figure 3.5 presents the CCD and CMD of the point sources within the 2 degree field centered on the Dragonfish Nebula, showing the distribution of all 2MASS point sources, as well as the relative location of the color cut. We indicate in red the point sources that fall within the association boundaries. We indicate in blue all stars within the field that meet the association's color cut. The position of the main sequence is indicated at a distance of 9.7 kpc and extinguished by $A_K = 1.0$. The reference magnitudes for the O spectral type are taken from Martins & Plez (2006), and for the remaining spectral types from Pickles (1998). The path taken by an O5V star if placed at varying distances, assuming the average extinction to distance ratio, is indicated by the red line. The path taken by any given reference star is just a translation of this path on the diagram. The color cut is sufficiently large to permit spectral classes of A and earlier at the given reddening. However, the sensitivity of 2MASS limits stars at this distance and extinction to be no later than B1V.

In Figure 3.6 we bin the CCD and CMD to investigate the overabundance in the region within the Dragonfish Association as compared to the surrounding regions. These figures indicate the location and prominence of the cluster overdensity as a function of both color and magnitude. For the CCD, we bin the sources in a 35^2 bin grid spanning $-0.3 < J - H < 2.5$ and $-0.2 < H - K < 1.1$. For the CMD, we similarly use a 35^2 bin grid with $5 < J - H < 17.0$, and identical $J - H$ limits. We grid the point sources that fall within the association boundaries and subtract the average
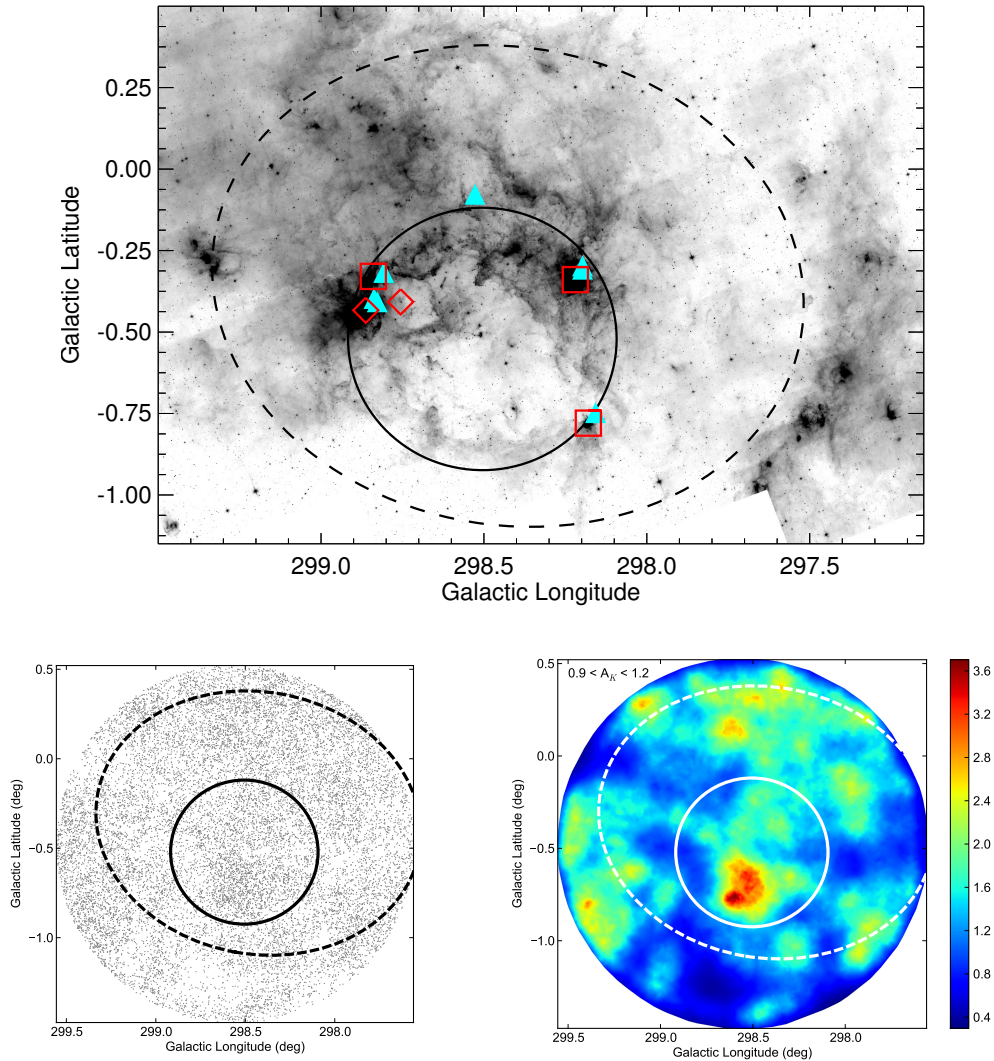
Figure 3.2: Top: The $8\,\mu$m GLIMPSE image of the Dragonfish Nebula. The dotted ellipse indicates the location of the WMAP source, and the solid ellipse indicates the location of the star-forming complex. The cyan triangles indicate the location of known H II regions. Clockwise from top: G298.56-0.11, G298.2-0.3, G298.19-0.78, G298.9-0.4, and G298.837-0.347. The red squares and diamonds indicate the regions of stellar clustering identified by Dutra et al. (2003) and Mercer et al. (2005). Bottom Left: The individual 2MASS sources within the field surrounding the Dragonfish Nebula passing the color cut. Bottom Right: The 2MASS stellar densities of the field surrounding the Dragonfish Nebula at the color cut corresponding to O-stars with extinctions between $0.9 < A_K < 1.2$. The color bar indicates the stellar density in stars per square arcminute.
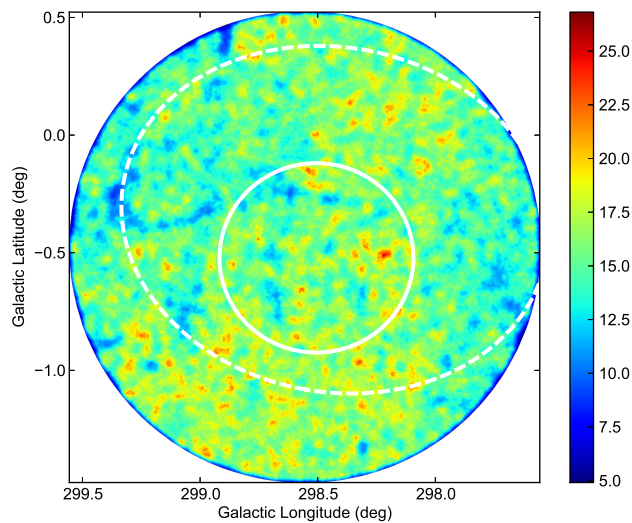
Figure 3.3: The 2MASS stellar densities of all stars in the field surrounding the Dragonfish Nebula. The color bar indicates the stellar density in stars per square arcminute. The ellipses are the same as in Figure 3.2.

bin value from the surrounding field. In both the CCD and CMD, an overabundance of point sources appears in the range $1.0 < J - H < 1.5$. We note an underdensity in the CCD at $(J - H, H - K) = (0.8, 0.3)$. The total number of sources "missing" in the underdensity is approximately 200. The underdensity is associated with a galactic structure feature in the surrounding field which we discuss in depth in Chapter 5.

Given that the colors of these underdense sources are separated from those of the putative OB association by a vector which is nearly parallel to the extinction vector, could the association be only an illusion caused by intervening extinction with $A_K \sim 0.25$? If so we would expect an overall deficit of stars in this direction (due to the extinction of dim sources), but there is no such trend. In fact the missing sources are about half as numerous as the surplus ones. Corroborating this point, we note that the vector separating the two populations is slightly steeper than the Nishiyama et al. (2008) extinction law (whereas the overpopulation is perfectly consistent with OB
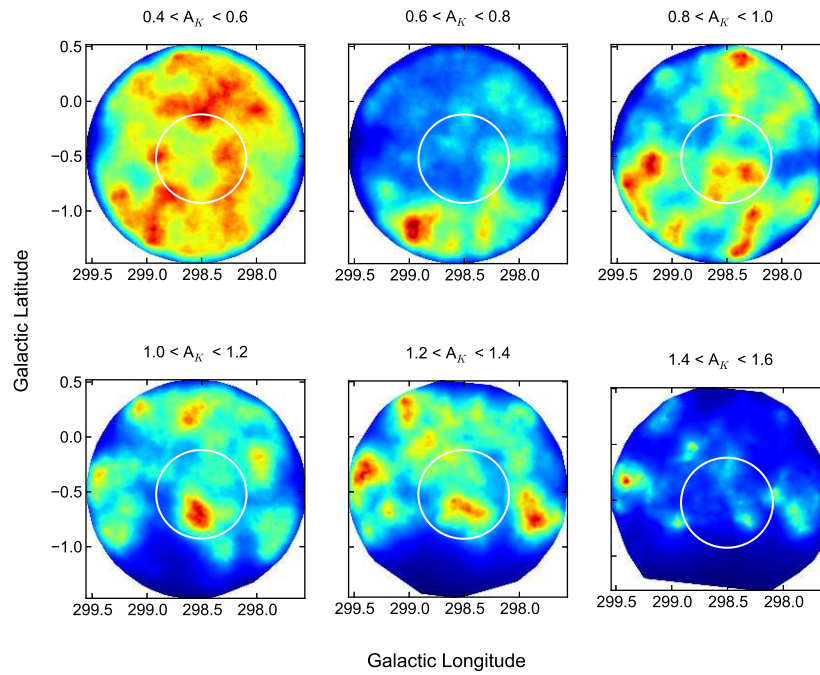
Figure 3.4: The 2MASS stellar densities of the field surrounding the Dragonfish Nebula in colour cuts corresponding to O-stars with extinctions between 0.4 and 1.6 in A_K. The ellipse indicates the location of the star forming complex.
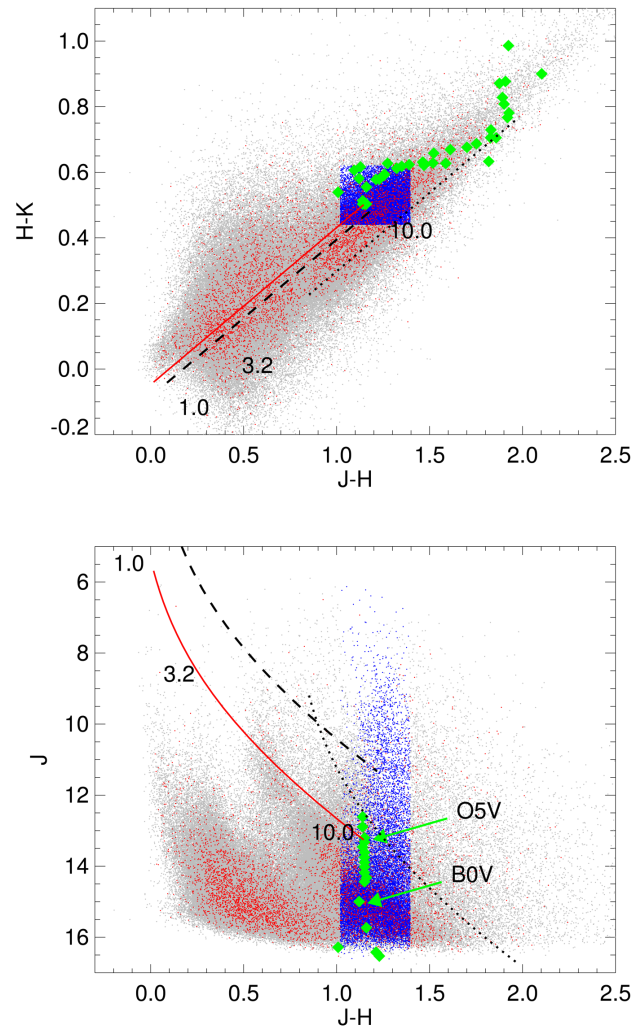
Figure 3.5: Color-color (top) and color-magnitude (bottom) diagrams of the 2MASS point sources. The grey points are all points within the two-degree field, while the red points are the sources within the association boundaries. The blue points indicate all sources within the color cut. The green diamonds indicate the main sequence at a distance of 9.7 kpc with an extinction of $A_K = 1.0$. The location of an O5V and B0V star are indicated for reference. The red line indicates the track of an O5V star at various distances, with the numbers indicating the distance in kpc. Similar paths are shown for K3II (black dotted line) and B0I (black dashed line) stars.
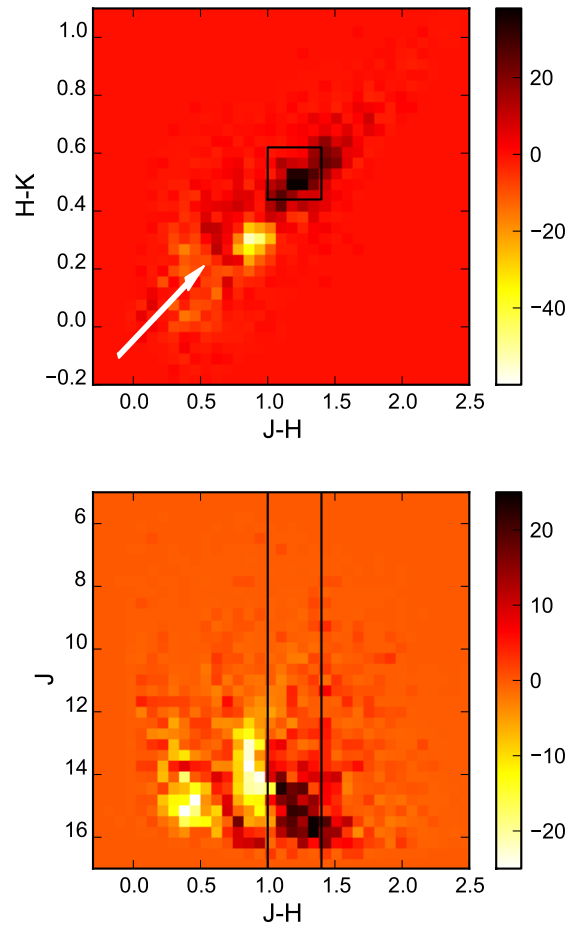
Figure 3.6: Binned color-color (top) and color-magnitude (bottom) diagrams of the 2MASS point sources within the candidate association boundaries with the binned background removed from the diagrams. The cluster color cut is indicated with the black lines. The color bars indicate the number of stars in each bin. The white arrow on the color-color diagram indicates the extinction vector corresponding to an $A_K = 0.5$ from the unreddened location of O stars.

stars reddened by that law). Moreover, sources which appear underdense on this plot vary on larger angular scales than that of the association; their population is mostly a function of galactic latitude, although there are somewhat fewer of them toward the association. We therefore conclude that the association does in fact exist, but there may also exist localized extinction which affects the color distribution of sources.

To further investigate the role of patchy extinction, we have obtained additional J and H band photometry towards a central $3.9'$ field in the candidate association using the Wide Field IR Camera on the 2.5-metre du Pont Telescope, with limiting magnitudes of $J = 17.1$, and $H = 16.3$ at a SNR of 3 (J. Radigan, private communication, 2010). We extract 906 stars in this field. With this additional photometry, we find stars in the range of $0.8 < J - H < 0.96$, with a continuous density of stars throughout this color range (Figure 3.7). Further, we find the overdensity of point sources at the 2MASS identified colour cut in the range of $1.0 < J - H < 1.4$, distinct from the other population of point sources with magnitudes brighter than $J < 15.5$, but merging into the other locus of sources at fainter magnitudes. We also find no evidence for any shadowing features which would indicate a strong extinction feature. This supports our conclusion that the apparent association is not an extinction feature.

3.5 Confusing sources

In order to identify possible contaminating stars within the color cut, we model the NIR colors and magnitudes of template stars of different spectral types and luminosity classes. We vary the distances of the model stars to examine which stars meet the cut above the 2MASS limiting magnitudes. We use reference magnitudes, extinction relationship and the average extinction-to-distance ratio as in §3.4.2. All main sequence OB stars down to B1V can fall within the color and magnitude limits. With the 2MASS limiting magnitudes, assuming the extinction-to-distance ratio, all subtypes of O stars are visible to 13 kpc. All main sequence stellar types later than
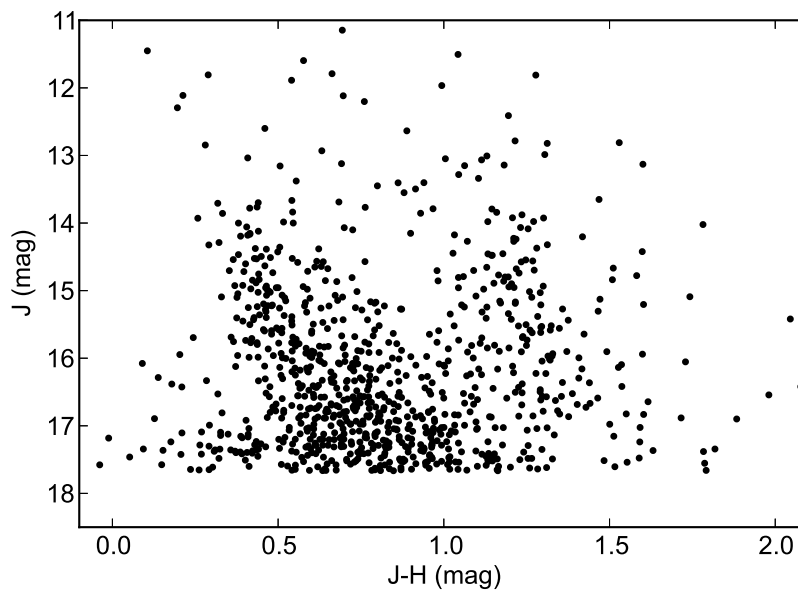
Figure 3.7: The J vs. J-H color-magnitude diagrams of the du Pont point sources at the centre of the association.

B1V fall below the magnitude limits. OB giants (down to B9III) and K1III to M0III giants can fall within the color and magnitude limits. All supergiant stars can fall within the association color cut and magnitude limits. We show examples of stars that may fall within the color and magnitude limits in Figure 3.5. The red-clump giant feature, composed of early K giant stars (López-Corredoira et al. 2002; Indebetouw et al. 2005) partially overlaps the association color cut towards the faint end, but is not the primary contributor to the background population.

Using the Robin et al. (2004) model of the stellar population we produce a synthetic catalogue of stars (Figure 3.8). We simulate the field in the direction and with the size of the Dragonfish Association, using the 2MASS limiting magnitudes from §3.3, and a diffuse extinction law of 1.6 A_V/kpc. The model background population underestimates the total number of sources. However, we find that the majority of stars within the color cut are early K giant stars with masses between 1 and 3 $M_\odot$ and distances between 3.0 and 4.5 kpc; we assume these represent our contaminating

sources.

3.6 Conclusions

We have used the 2MASS point source catalogue to search for the central OB associa-tion within the Dragonfish Nebula by analyzing the on-sky stellar density with NIR colors consistent with extinguished O stars. We find an overdensity of point sources within the bubble at an extinction range of $0.96 < A_K < 1.2$. Comparing the CCD and CMD of the candidate association with the surrounding field, we confirm the presence of the overdensity at the chosen color range. We reject an extinction explanation for the overdensity and infer that the contaminating star population consists predominantly of K giants 3-4.5 kpc away. Our candidate association contains 406 ± 102 members visible in 2MASS with magnitudes consistent with O and early-B stars, similar to the ionizing population expected from the region's free-free luminosity. We infer from its assumed mass, radius, and maximum age that it is likely to be unbound on the whole but may contain a bound core; however further investigation is necessary to determine its dynamical state. This is a candidate for the most luminous (and consequently the most massive) OB Association in the Galaxy. If confirmed by upcoming spectroscopic observations, the Dragonfish Association is an outstanding candidate for multiwave-length examination, as it is a promising laboratory massive star formation, stellar dynamics, and feedback processes within the Galactic environment.
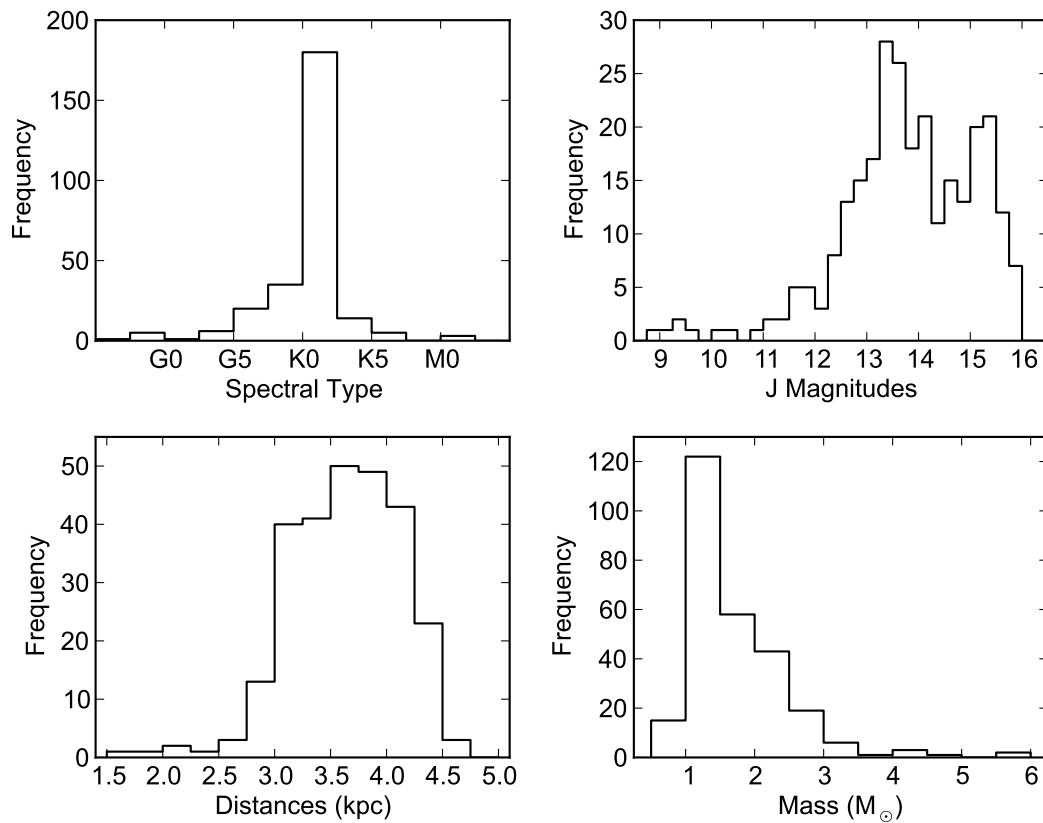
Figure 3.8: Histograms of the synthetic population produced with the Robin et al. (2004) simulation, limiting to the selected colour cut and magnitude limits of 2MASS. The histograms show the distributions of the synthetic population in spectral type (top left), magnitude (top right), distance (bottom left), and mass (bottom right).

Chapter 4

Spectroscopy of the Dragonfish Association

A preliminary version of this chapter was published as:

4.1 Chapter Overview

Young OB associations with masses greater than 10^4 M$_\odot$ have been inferred to exist in the Galaxy but have largely evaded detection. Recently, a candidate OB association has been identified within the most luminous star forming complex in the Galaxy, the Dragonfish Nebula. We identify 18 young, massive stars with near-infrared spectroscopy from a sample of 50 members within the candidate OB association, including 15 O-type, and three Luminous Blue Variables or Wolf-Rayet stars. This number matches the expected yield of massive stars from the candidate association, confirming its existence and ability to power the parent star forming complex. These

results demonstrate the existence of a 10^5 M$_\odot$ OB association, more powerful than any previously known in the Galaxy, comparable in mass only to Westerlund 1. Further, the results also validate the color selection method used to identify the association, adding credence to others discovered in the same way.

4.2 Introduction

The most luminous and powerful of a galaxy's young stellar associations contain a significant fraction of its massive stars, and dominate all collective forms of energetic feedback into the galaxy's large-scale wind, gaseous disk, and halo (McKee & Williams 1997; Dove et al. 2000). While the massive cluster populations of some other galaxies, such as M83 are well characterized (Chandar et al. 2010), only the closest couple kiloparsecs of the Milky Way have been probed in detail (Lada & Lada 2003). Across the Galactic plane, severe obscuration by dust and the high density of field stars have confounded searches for even the most luminous associations, leaving our knowledge of them incomplete. About 50 young OB associations with masses greater than 10^4 M$_\odot$ have been inferred to exist in the Galaxy (McKee & Williams 1997; Larsen 2009); however, they have largely evaded detection.

Our view of the Galactic population of H II regions is substantially more complete, thanks to radio surveys (Caswell & Haynes 1987) and subsequent follow-up studies. Of the identifiably coherent structures which emerge from such work, the most luminous is the so-called Dragonfish Nebula at $(l,b)=(298,-0.4)$ (Murray & Rahman 2010, Chapter 2). Located on the far side of the Galaxy, 9.7 kpc through the Galactic disk, its morphology and radio velocities are indicative of an expanding bubble. Its H-ionizing luminosity of $10^{51.8}$ photons per second, if it originates from a coherent group of stars, requires the presence of the most luminous young stellar cluster or OB association in the Galaxy. The region's distance and location in the Galactic plane imply a high degree of extinction, roughly $A_K \sim 1$ or $A_V \gtrsim 10$.

Using a near-infrared (NIR) color selection method, a candidate for the central powering source of the Nebula was identified: the Dragonfish Association (Chapter 3[1]). The association is composed of 406 ± 102 candidate O stars, consistent with the measured ionizing luminosity, making it one of the largest single OB associations or young clusters in the Galaxy (M $\sim 10^5$ M$_\odot$). Notably, the candidate association is not projected towards one of the bright regions of H II and $8\,\mu$m emission in its vicinity, but within an evacuated shell surrounded by such emission. This suggests that the ionizing source has inflated a bubble of radius 69 pc within the Galactic disk. The overdensity of sources being indirect evidence, we seek direct spectroscopic confirmation that the overdensity consists of O stars, and that the field objects are K giants.

In this chapter, we confirm the existence of the Dragonfish Association through NIR spectroscopy of massive stars. In addition, we identify two candidate Luminous Blue Variables and a Wolf-Rayet within the association. This verifies the presence of a OB association which, on the basis of source counts, is sufficiently luminous to power its host star forming complex, giving it a total mass of 10^5 M$_\odot$ and making it the most luminous OB association in the Galaxy. The confirmation of the Dragonfish association validates the NIR color selection method as a way of identifying candidate clusters and associations in distant star forming complexes.

4.3   Observations & Data Reduction

We performed near-IR low-resolution long-slit spectroscopy of 50 candidate O-stars within the Dragonfish Association and a control sample of four non-cluster sources, using SOFI on the 3.6m New Technology Telescope (NTT) at the ESO La Silla Observatory between March 16-20, 2011. Low resolution (R $\sim$ 1000) spectra were taken of

---

[1]Published as Rahman et al. (2011a)

each of the candidate stars between 1.52 and 2.4 μm using a 0.''6 slit. We were able to observe two candidates simultaneously using the length of the slit (290") where alignment on the sky was possible. A nod-and-shuffle technique was used to improve the removal of the near-IR OH sky lines. Both samples are limited to NIR colors consistent with extinguished O stars (or less extinguished K giants), and to K magnitudes brighter than 12. The control sample is offset from the candidate association by 0°.5 and should represent the interloper sources within the cluster sample. The total integration time is 60 min for each cluster source and 2 min for each non-cluster source, using the nod-and-shuffle technique. This provides minimum signal-to-noise ratios of > 250 and > 50, respectively. In addition, standard O, K, A, and Wolf-Rayet stars were observed with a minimum SNR > 40 to aid in the spectral classification.

The instrumental crosstalk effect was removed from all calibration and science frames using the Image Reduction and Analysis Facility (IRAF) script provided by observatory. The remainder of the data reduction and analysis took place in Python using the *numpy*, *scipy*, *matplotlib* and *pyfits* packages.

The wavelength calibration was determined using Xenon arc lamp images taken at the beginning of each night. Nine reference emission lines between 1.54 and 2.48 μm were fit with using a Gaussian for each row of pixels along the spatial axis. The centre positions of each line were fit to a cubic function to produce an independent wavelength solution for each row of pixels along the spatial axis. Based on the accuracy of both the Gaussian and cubic fit, the error in the wavelength solution is smaller than 1 Å.

Bad pixels were identified in each frame using a gradient-based filter; the centre-weighted second-gradient of each frame was taken. The gradient was taken along the spatial axis rather than the dispersion axis to keep detail in wavelength dependent features. Pixels above a threshold in the second-derivative image were identified as bad pixels. Pixels identified in this manner were combined with the observatory-

provided bad pixel mask. The values of the bad pixels were replaced using a linear interpolation method using the neighbouring good pixels along the spatial axis.

A master flat was produced from the normalized median of the dome flats taken each night. A comparison of the flats from each night show little variation, indicating a stable flat field throughout the observing run.

Each of the sequential dither positions were subtracted from one another and divided by the master flat to remove the effects of sky emission, dark current, and flat fielding. Due to the time-varying nature of the OH sky lines, residuals of the sky lines remain in the frame. This was corrected by subtracting the median of a 10-pixel strip along the spatial axis from the spectra pixels.

The spectra on the differenced frames were fit to a linear function to correct for the alignment of the slit on the detector. The centroid of the spectra shifts between 3-4 pixels from the top of frame to the bottom. To extract the spectra, a 10-pixel strip, centred on each spectrum, along the spatial axis was summed for each row along the dispersion axis to produce a one-dimensional spectum. This extracted spectrum was normalized by dividing by the median data value.

Each of the science targets had 3 nod-and-shuffle cycles producing 6 spectra. Each of the 1-D spectra were regridded using a linear interpolation method to ensure accurate wavelength combination. The combined spectrum was produced by taking the mean of intensity value at each wavelength bin. An estimate of the error was produced by taking the standard deviation of the individual spectrum at each bin, producing the estimates of the SNR of > 250 for cluster sources, and > 50 for non-cluster sources.

To correct for sky transparency and the wavelength-dependent detector sensitivity, a transparency function was produced from spectra of two telluric standards taken at the airmasses of the science targets. These standard stars were Hipparcos 59642 (G1V), and Hipparcos 62539 (F5V). The spectra were divided by models of G0V and F5V stars from Lancon & Rocca-Volmerange (1992). A 45 Å median filter was applied

to the resultant transparency function to correct for any single-pixel noise effects in the telluric spectra. The combined spectrum was divided by the transparency function. The H-band (1.5-1.8 μm) and K-band (2.0-2.4 μm) windows were isolated and continuum rectified individually. The spectra were continuum rectified by fitting the spectra in each of the windows to a third-order polynomial and dividing by the fit. We use the resultant 1-D spectrum for stellar classification.

4.4   Analysis & Results

4.4.1   Spectral Classification

From the NIR color identification method, the contaminating non-member population confused with the candidate association is predominantly K giants with moderate extinction ($A_K \simeq 0.3$; Chapter 3). Due to the high extinction, the intervening interstellar medium will imprint absorption lines on the spectra as well, primarily from neutral metals (see §4.4.2). The NIR spectra of K giants are similarly riddled with neutral metal lines, causing difficulty in identifying O stars on this basis, at least at low spectral resolution (Rayner et al. 2009). Consequently, to type each of the stars, we concentrate on visually identifying and isolating spectral features that appear in early-type stars and comparing their relative strengths to that from reference spectra.

To discriminate between extinguished O stars and K giants, we concentrate on visually identifying two absorption lines which are characteristic of massive young stars but absent or very weak in K giants. These are the 2.166 μm Br γ line and the 1.700 μm He I line, which is prominent in late O stars. A number of weaker features, such as the 1.693 μm He II line (present in early O stars), 1.681 μm H I line, and the 2.188 μm He II line, are also useful for identification.

In Table 4.4.1, we present the identified young massive stars: 15 O stars and three evolved massive stars. We present the spectra of a selection of these stars in Fig 4.1. We

classify the NIR spectra of O stars with the Brackett series of hydrogen absorption lines and He I and II absorption lines. These features are weak, necessitating signal-to-noise ratios above 100 for detection (Hanson et al. 2005). We determine a subtype range and luminosity class with the aid of the weaker absorption lines and NIR photometry using the NIR extinction law from Nishiyama et al. (2009) and model photometry from Martins & Plez (2006). The magnitude differences between luminosity classes (from 0.2 to 1.0 mag in the K-band) of the same spectral subtype ranges make it improbable for small differences in the extinction determination to change the luminosity class identification. We note that massive stars with weaker features, such as early O stars lacking He I absorption or with Brackett γ absorption that has been filled in, may evade detection (Hanson et al. 2005). All except the most luminous stars (the WN9 and O4-6 stars) show strong Br γ absorption. The later stars all show He I absorption while the earlier stars show He II absorption.

In addition to the 15 O stars, we identify one Wolf-Rayet star based on H I, He I and He II emission (Morris et al. 1996). Further, we find two candidate Luminous Blue Variable (LBV) candidates, based on numerous He I emission lines, and [Fe II] emission in one case (Fig. 4.2; Morris et al. 1996). These LBV candidates fit best the profile of "quiet" or "late" LBVs, with smaller emission lines than more "active" LBVs. Active LBVs would be excluded from the associaiton colour cut due to the significant line emission that would alter the colours of the objects. These rare, exotic objects, transition stages of the most massive stars, are typically found in locations of recent star formation. Confirmation of the LBVs will require studies of their photometric variability.

4.4.2   Interstellar Features

The high signal-to-noise spectra of the massive stars presented in figure 4.1 contain a number of features that are similar to features in the contaminating K-giant population.

Table 4.1.   Massive Stars Identified in the Dragonfish Association

#	RA	Dec	l (deg)	b (deg)	Spectral Type	K_S (mag)	A_K (mag)
1	12h11m30.2s	-63°15′35″.7	298.458	-0.736	O6-8I	10.5	1.2
2	12h11m32.0s	-63°15′52″.7	298.462	-0.740	O8-9.5I	10.5	1.1
3	12h11m41.4s	-63°16′31″.4	298.481	-0.748	O8-9.5III	12.0	1.0
4	12h11m48.2s	-63°14′33″.6	298.488	-0.713	O6-8III	11.1	1.0
5	12h11m54.1s	-63°17′04″.0	298.506	-0.753	WN9	11.5	1.2
6	12h11m58.4s	-63°09′42″.1	298.495	-0.630	O8-9.5III	11.6	0.9
7	12h12m06.5s	-63°11′36″.1	298.515	-0.659	O6-8III	11.0	1.1
8	12h12m11.1s	-63°12′20″.8	298.525	-0.670	O4-6V	11.6	1.1
9	12h12m20.3s	-63°13′42″.5	298.546	-0.690	LBV?	11.9	1.1
10	12h12m21.4s	-63°16′38″.4	298.555	-0.738	LBV?	9.0	1.1
11	12h12m22.1s	-63°13′40″.9	298.549	-0.689	O9-9.5III	11.7	1.0
12	12h12m29.5s	-63°10′51″.5	298.556	-0.641	O5-7V	11.9	1.1
13	12h12m37.2s	-63°14′52″.5	298.580	-0.705	O4-6V	11.6	1.1
14	12h12m41.3s	-63°09′27″.3	298.574	-0.614	<O5V	11.9	1.1
15	12h12m52.3s	-63°17′03″.9	298.613	-0.736	O7-9.5III	11.2	1.0
16	12h12m52.6s	-63°18′30″.8	298.618	-0.760	O6-8III	11.4	1.0
17	12h12m54.4s	-63°17′56″.5	298.619	-0.750	O6-8I	11.1	1.2
18	12h12m55.3s	-63°06′40″.6	298.593	-0.564	O9-9.5III	11.3	1.0
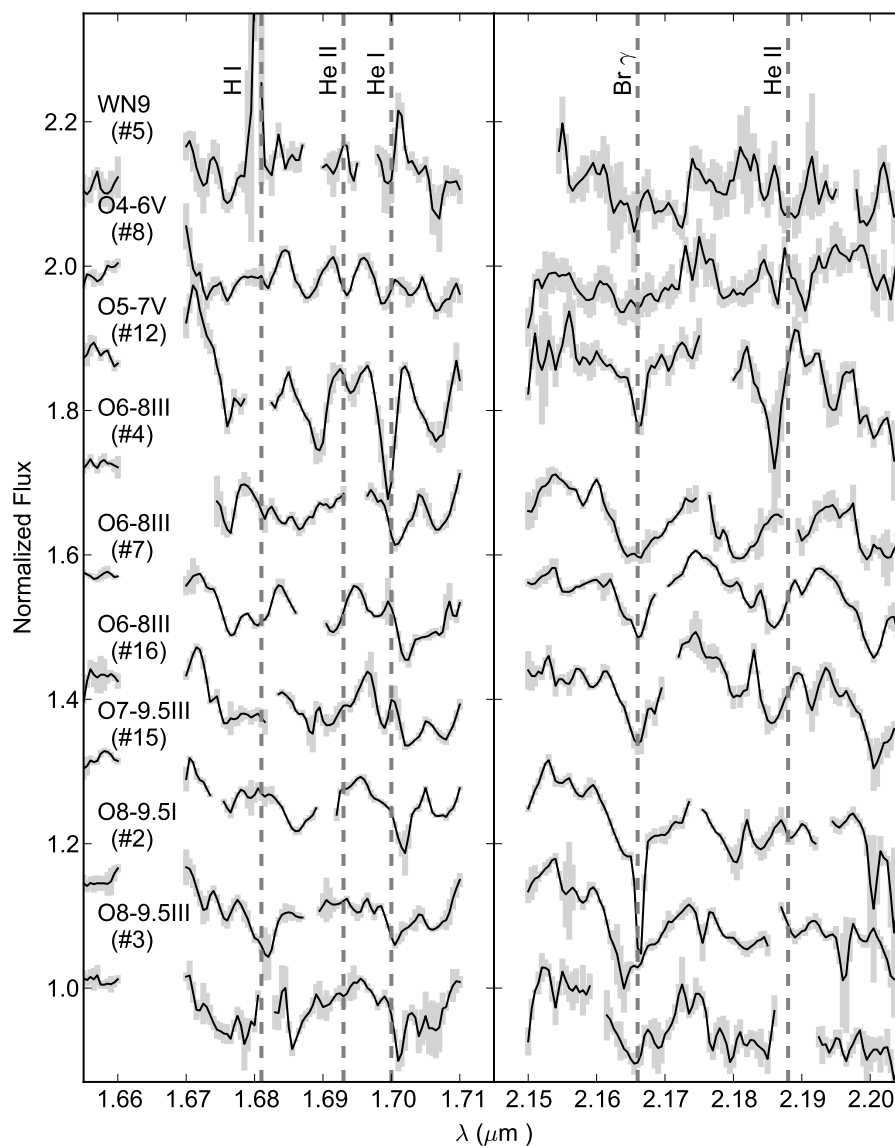
Figure 4.1: The spectra of 9 massive stars within the Dragonfish Association at the wavelength ranges of interest for spectral classification. The spectral types and identification numbers from Table 4.4.1 are indicated. The wavelengths of features used to classify the stars are indicated with dashed lines. The spectra have not been adjusted for Doppler shifts. The error bars are indicated in grey.
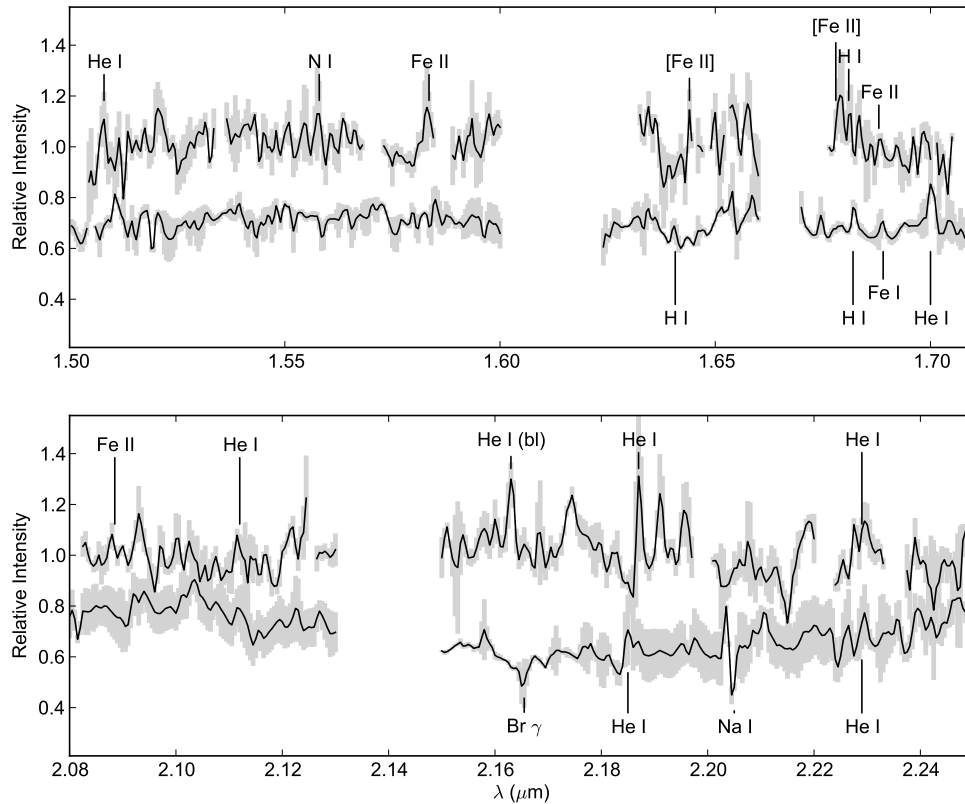
Figure 4.2: The spectra of the two candidate luminous blue variable candidates. The upper spectrum is star 9 and the lower is star 10 from Table 4.4.1. The error bars are indicated in grey. Characteristic spectral features are indicated. All spectral features are significantly stronger than those of the O-stars.

Riddled throughout the spectra are neutral metal lines, primarily from Mg, Al, Fe, and Si. These elements are common in the interstellar medium and have been observed in absorption within the local 100 pc (Redfield & Linsky 2004). Consequently, these lines are expected to be imprinted on relatively featureless spectra when seen through a large column, as would be expected towards the association.

In addition to the metal absorption lines, strong CO vibrational absorption bands are visible in the spectra of all identified massive stars at 2.29, 2.32 ($v = 2 \to 0$) and 2.35 ($v = 3 \to 1$) μm. These are often detected as photospheric absorption features of K-giants (Rayner et al. 2009), however, they may be also imprinted on nearly featureless spectra of younger, more massive stars by interstellar absorption. The $v = 2 \to 0$ bands have been detected towards NGC 2024 IRS 2 with line widths $\Delta v = 1.4$ km s^{-1} (Black & Willner 1984). The individual lines within each band are found to be saturated with total band equivalent widths of $\sim$0.5 Å (Lacy et al. 1994). Towards the Dragonfish region, there is CO emission detected between 10 km s^{-1} < v_{lsr} < 30 km s^{-1} coincident with the Dragonfish association and its surrounding photon-dominated region (PDR; Grabelsky et al. 1988; Murray 2011). In the stacked cluster O-star spectra (see §4.4.3), the equivalent width of each of the CO bands is $\sim$5 Å, consistent with what is seen towards NGC 2024 when saturated over a larger range of velocities.

While the presence of the CO bands challenges the spectral typing of the stars, we can use additional absorption line features to confirm the accuracy of the typing. Specifically, the two next strongest K-band spectral features in the spectra of cool stars are the Calcium/Iron absorption feature at 2.26 μm, and the Sodium/Scandium absorption feature at 2.20 μm. These features are present and strong in cooler stars, visible from F-type to M-type stellar spectra. In the spectra of the non cluster stars (see Fig. 4.3), these features are strongly detected, but not found in the spectra of the stars classified as O-type based on the presence of hydrogen and helium absorption features. This independent test indicates that the spectra typing is accurate and the

CO bands are likely due to an interstellar effect rather than a photospheric effect.

For the $v = 3 \to 1$ band to arise in the ISM, sufficient CO with excitation temperatures exceeding 1000 K must exist to populate the $v = 1$ vibrational state. The PDR traced by polycyclic aromatic hydrocarbon emission in the region (Chapter 2), is a likely site of such warm CO (Hollenbach & Tielens 1997). We note that CO $v = 2 \to 0$ and $v = 3 \to 1$ bands have been observed in absorption towards massive stars in Cygnus OB2 classified by NIR and optical spectroscopy, at significantly lower dust extinctions than the Dragonfish's (Comerón et al. 2008). Therefore, we conclude that CO absorption bands in the NIR spectra of the identified O stars are plausibly interstellar in origin, at least when the O stars are surrounded by an intensely illuminated PDR. However, this point deserves additional study.

4.4.3 Stacked Spectra Comparison

To investigate the weak NIR features in a more robust manner, we construct three groups of sources and examine the stacked spectra of each: the 15 cluster O stars, the 32 cluster sources not immediately identified as massive stars, and the four non-cluster field sources from our control sample. We present the stacked spectra in figure 4.3. The primary spectral discriminators, Br γ and 1.700 μm He I, are strong in the cluster O stars. Br γ is weaker but visible in the cluster contaminant population, and both lines are absent in the control non-cluster population. Further, weaker H I absorption features at 1.514, 1.534, 1.544, 1.556, 1.570 and 1.681 μm, characteristic of massive stars rather than cool giants, are detected in the O star population and absent in the others. Conversely the Ca and Fe feature at 2.26 μm, a characteristic feature in the spectra of cool stars, is strong in the non-cluster population, weak in the cluster contaminants, and absent in the O stars. In addition, differences between the three populations are visible with lines at 1.522 μm Mn, 1.529, 1.551, 1.573, and 1.697 μm Fe, and 2.207 μm Na/Sc, all of which are present in the non-cluster and contaminant populations, and

either weak or absent in the O star population. These spectral differences confirm that the identification of the association O stars is robust.

4.4.4 Possible Runaway?

One of the identified O stars, Source 14 in Table 4.4.1, appears to be highly blueshifted in the 1.693 μm He II, 1.700 μm He I, 1.736 μm H I and Br γ absorption lines. The blueshift of the lines corresponds to a radial velocity of 300 ± 50 km s^{-1}, as compared to the other O stars that show no signficant Doppler shift. The velocity is much larger than can be explained by Galactic rotation. This indicates that the star is in a close binary system, or is a runaway O star either kicked out of the association or originating elsewhere. In our single-epoch spectrum, we find no indications of a companion star in the spectrum, such as splitting of spectral lines. If it is a runaway, it could have been produced by a binary-binary encounter or by the result of the supernova explosion of the primary of a massive binary (Gvaramadze et al. 2008). Similar massive runaways have been identified originating from Cygnus OB2 (Comerón & Pasquali 2007).

4.5 Discussion & Summary

The spectroscopic identification of massive, young stars confirms the existence of a young OB association within the Dragonfish Nebula, but its share of the nebula's ionization budget must be addressed statistically. Using the extracted candidate cluster properties from Chapter 3, we infer a membership probability of 35.5 %, for an expected yield of 17.8 ± 3.4 members in the cluster sample. Indeed, 18 of our cluster sources are young, massive stars. This confirms that the Dragonfish Association is real, and not a chance sky overdensity of other stellar types (e.g. K-giants) coincident with the nebula or a spurious effect of intervening extinction. Further, this indicates that the NIR color selection method produces association membership probabilities
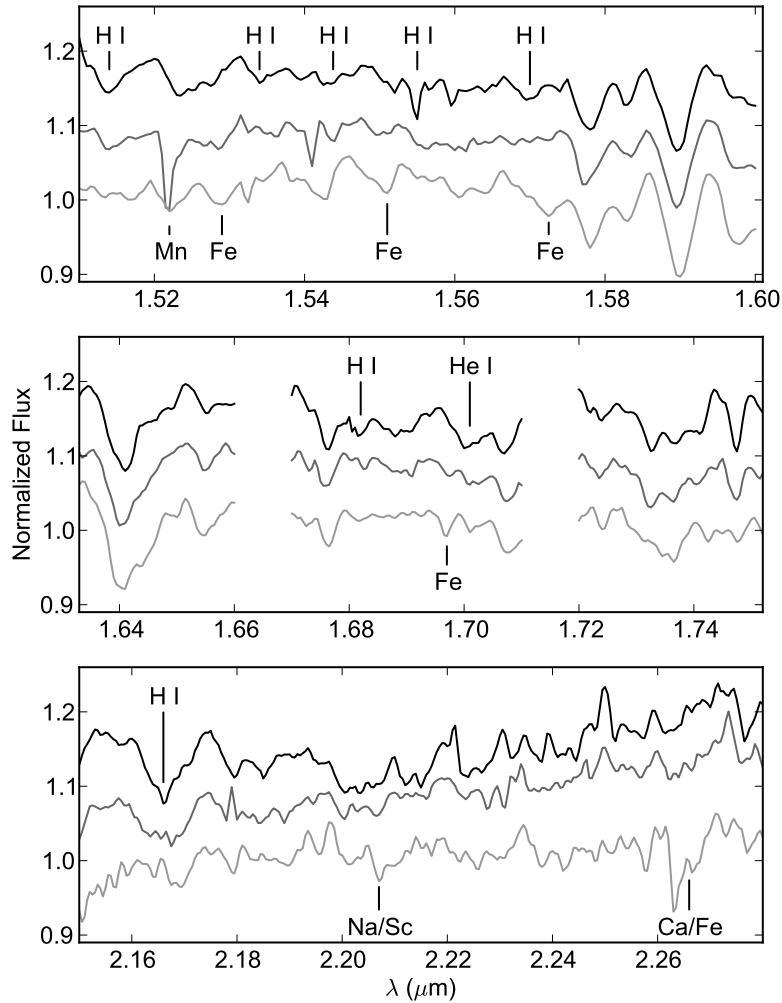
Figure 4.3: The stacked cluster O star (top, black line), cluster contaminant (middle, lighter, line) and non-cluster (bottom, lightest line) spectra. The error of the stacked spectra is at the 0.01% level, and so is not indicated. Characteristic distinguishing spectral features are indicated for the O stars and K giants. The cluster contaminants likely include massive stars with features too weak to be identified on individual spectra.

consistent with the actual yield within the association.

From the point sources identified using the color selection method, assuming a minimum candidate spectral type of O9.5V (Martins et al. 2005) and using a standard stellar initial mass function (Kroupa 2001), the inferred total stellar mass of the association is $\sim 10^5$ M$_\odot$ (Chapter 3). This result, based solely on the population statistics, is remarkably consistent with the estimated mass of the minimum stellar population required to power its central star forming complex (Chapter 2). This indicates that the Dragonfish Association dominates the ionization of its surrounding nebula. Further, the mass of this association is greater than other luminous associations in the Galaxy such as NGC 3603 (1.3×10^4 M$_\odot$), Trumpler 16 in the Carina Nebula (1.8×10^4 M$_\odot$), Cygnus OB2 (7.6×10^4 M$_\odot$), and the Arches (7.7×10^4 M$_\odot$; Weidner et al. 2010). It is similar to that of Westerlund 1 (10^5 M$_\odot$; Clark et al. 2005), however the Dragonfish is significantly more luminous compared to Westerlund 1 based on its free-free luminosity (Westerlund 1 is not visible in the WMAP free-free maps; Murray & Rahman 2010). This is consistent with the more evolved state of the massive stars in the latter. If the Dragonfish association is, in fact, the sole engine of the free-free emission in the complex, its output of $10^{51.8}$ H-ionizing photons per seconds is similar to R136, the dominant powering source of the most luminous H II region in the Local Group, 30 Doradus in the Large Magellanic Cloud (Parker & Garmany 1993; Evans et al. 2011).

The identification of O stars and evolved massive stars confirms the existence of the Dragonfish Association. The association is not embedded within a bright H II region, but rather a void of continuum and PAH emission surrounded by a shell, indicating that it is the central illuminating and inflating source of the Galaxy's most luminous star forming complex. As an extreme example of Milky Way star formation, the Dragonfish complex merits further study in a number of ways. Its large population of O stars, an estimated 13 with masses > 100 M$_\odot$ (using the initial mass function

from Kroupa 2001), makes it an ideal laboratory for investigations of environmental influences at the upper limit of stellar masses. With high-precision astrometry, its membership can be more firmly established and its internal kinematics can be probed. X-ray, radio, and γ-ray follow-up is warranted to identify colliding wind binaries and young stellar objects. Searches for IR excess sources should reveal a population of new protostars triggered by its influence. Moreover, this influence should be sought in the dynamics of atomic and molecular gas in its environment.

Additional candidate associations have been identified towards star forming complexes identified by Chapter 2 using this method and will be characterized Chapter 5. The confirmation of the Dragonfish Association adds significant credence to the hypothesis that colour-selected clusters found toward the Galaxy's most luminous star forming complexes are in fact their driving stellar associations.

Chapter 5

Searching for Young, Massive Clusters & OB Associations

A preliminary version of this chapter was submitted as:

"OB Associations at the Upper End of the Milky Way Luminosity Function"

Rahman, M., Matzner, C.D., & Moon, D-S., 2012, The Astrophysical Journal

5.1 Chapter Overview

The Milky Way's most luminous, young and massive ($M \gtrsim 10^4$ $M_\odot$) star clusters and OB associations have largely evaded detection despite knowledge of their surrounding H II regions. We search for these clusters and associations within the 40 star forming complexes from Rahman & Murray in the 13 most luminous WMAP free-free emission sources of the Galaxy. Adopting the colors of OB stars, taking into account the line-of-sight extinction, we identify new candidate associations using the 2MASS point source catalog. In 40 star forming complexes searched, 22 contain cluster/association candidates with sizes and masses in the range of 3′–26′ and $10^{2.3}$–10^5 $M_\odot$ respectively. Of the 22 candidates, at least 7 have estimated masses $\gtrsim 10^4$ $M_\odot$, doubling the number of such massive clusters known in the Galaxy. Applying our method to

a statistically similar set of target locations, we estimate that 3.0 ± 0.6 of these 22 candidate associations are unrelated to the star forming complexes. In addition, the extinction measurements of the candidates correlate well with extinction estimates from a model Galactic extinction distribution. These facts, along with the clear detection of Cygnus OB2 and the previous verification of the Dragonfish Association as the most luminous OB association in the Galaxy, validate our method. The 22 candidates are located in 12 WMAP sources searched, leaving only one without an identified candidate. In 8 of the most luminous WMAP sources, the enclosed candidates can account for their observed free-free flux. This is suggestive of the presence of hidden clusters in the remaining 5. With our new compilation, the Galactic census of young, massive stellar associations may now be very close to complete.

5.2   Introduction

A spiral galaxy's metabolism is dominated by the effects of its most massive ($M \gtrsim 10^4$ M$_\odot$) young stellar clusters and OB associations. Not only are these clusters and OB associations the birthplaces of a substantial fraction of a galaxy's stars, but they also dominate the energetic feedback within the galactic disk and drive disk-halo interactions through the production of superbubbles (McKee & Williams 1997; Chu 2008). While the upper end of the cluster mass function (CMF) has been derived through Galactic H II region observations (McKee & Williams 1997; Murray & Rahman 2010), the powering clusters of the H II regions have mostly evaded detection. This is primarily due to the large distance and extinguishing column through the Galactic Disk. While a number of members of the upper end of the CMF have been identified and characterized, including NGC 3603 (Stolte et al. 2004) and the Galactic Centre clusters (Figer et al. 1999), the census of the upper end is far from complete. This poses a problem for any global studies of the Galaxy's energy budget, star formation

properties, turbulence, and overall ecology. Moreover, more complete knowledge of the upper end of the CMF is required for detailed comparison to other galaxies, critical to further understanding the role of star formation in galaxy evolution (Whitmore et al. 2007; Larsen 2009).

The work in Chapter 2 with data from the *Wilkinson Microwave Anisotropy Probe* (WMAP) and the *Spitzer* GLIMPSE survey has identified 40 star forming complexes (SFCs) within the Galaxy's most luminous free-free emission sources. Only one of the SFCs has a previously identified powering cluster (NGC 3603), indicating that the complexes may be harboring unknown luminous young massive clusters and OB associations. Notably, Chapter 3 identified a candidate association for the most luminous SFC (the Dragonfish Nebula) based on the density of near-infrared (NIR) point sources, filtering non-member field stars using an extinction-related color-cut. The candidate association is located 9.7 kpc through the Galactic disk with a line-of-sight extinction $1.0 < A_K < 1.4$ mag. Without the NIR colour selection process, the association would remain hidden to visual or automated cluster search methods. Follow up NIR spectroscopy of this candidate has confirmed the presence of the most luminous OB association in the Galaxy, the Dragonfish Association (Chapter 4[1]).

In this chapter, we expand upon the method of Chapter 3 to search for young massive clusters or OB associations in all of the SFCs identified in Chapter 2. We organize this chapter as follows: In §5.3, we discuss previous cluster searches, followed by outlining the nature of the target SFC in §5.4. We discuss the use of the Two Micron All-Sky Survey (2MASS) for cluster searches and present the cluster search technique in §5.5. In §5.6, we present our new candidate clusters and associations and their statistical significance, whereas we estimate masses and luminosities for the candidates in §5.7. We, in §5.8, produce and discuss the most recent census of Galactic young massive clusters and OB associations, and finally summarize our conclusions in §5.9.

---

[1]Published as Rahman et al. (2011b)

5.3   Previous Cluster Searches

Star clusters have historically been discovered in the visible wavelengths. However, these discoveries have been limited to the closest cluster populations due to the substantial dust obscuration through the disk. The advent of large NIR surveys has enabled the search for star clusters and OB associations through this obscuration. Specifically, the 2MASS (1.2–2.2 μm) and the Spitzer Galactic Legacy Infrared Mid-Plane Survey Extraordinaire (GLIMPSE, 3.6–8.0 μm) have produced catalogs covering large areas of the Galactic plane in wavelengths where stellar flux dominates but extinction effects are minimized, although not completely eliminated (Skrutskie et al. 2006; Benjamin et al. 2003).

Dutra et al. (2003) and Bica et al. (2003) have systematically searched for star clusters in 2MASS, focused around optical and radio nebulae–primarily H II regions. Their search used visual identification of clustering on small images (5′– 15′ square) centered around the nebulae. Though this process, 346 new cluster candidates were identified. However, these efforts only searched for clusters around known nebulae, missing those not coincident with nebular emission (see §5.4). In a more automated manner, Froebrich et al. (2007) used the total on-sky stellar density of 2MASS point sources within $|b| < 20°$ to identify 1788 cluster candidates, of which 1021 are new. This method is less biased towards nebula-coincident clusters, but more susceptible to false positives. They estimated that their contamination rate of chance overdensities within their catalog is approximately 50%. In both these cases, the searches are most sensitive to dense clusters, rather than diffuse regions. For instance, Froebrich et al. (2007) only detected a small clustered region within Cygnus OB2, rather than the entire OB association with a half-light radius of 13′, readily identifiable with 2MASS (Knödlseder 2000). Over 96% of the Froebrich et al. (2007) catalog candidates have a total central cluster density of greater than four sources per square arcminute, and over half greater than 10 sources per square arcminute. For the highly veiled

case where only the most luminous stars are visible, typical source densities of 10^4 $M_\odot$ OB associations are expected to be $\sim 1.0(R/10 \text{ pc})^{-2}(D/10 \text{ kpc})^{0.84}$ sources per square arcminute, where R and D are the association radius and distance (Chapter 3). For comparison, the typical stellar density of a 2MASS field in the Galactic Plane is between 14 and 17 sources per square arcminute (§5.5.1). Consequently, these previous 2MASS searches are insensitive to more dispersed OB associations. Similarly, Mercer et al. (2005) identified 92 new cluster candidates using similar automated and visual identification methods with the GLIMPSE point source catalog. All of the GLIMPSE cluster candidates have diameters of $3'$ or less, indicating the same bias towards dense clusters. Since there are likely many more associations, such as Cygnus OB2, with diameters $> 3'$, a systematic search optimized towards larger, more massive OB associations is required to find them.

For the candidate clusters identified in the works of Dutra et al. (2003), Bica et al. (2003), and Mercer et al. (2005), further photometric and spectroscopic studies have been conducted on the candidate clusters, which have found high rates of false positive clusters (Borissova et al. 2005; Ivanov et al. 2005). In the cases of clusters that are confirmed, they have masses that tend to be in the range of 10–1,000 $M_\odot$. These masses are much smaller than the Galaxy's most massive clusters and OB associations, and many of these clusters do not contain any stars with spectral types earlier than B. Consequently, the stellar populations of the confirmed clusters are insufficient to ionize their surroundings (Hanson & Bubnick 2008; Soares et al. 2008). This suggests that the stellar populations in these regions have not been fully identified.

The recent work by Bica & Bonatto (2011) indicates that when candidate clusters are poorly populated or projected against dense stellar backgrounds, discerning a real cluster from a field density fluctuation (or asterism) is difficult or impossible. This poses a problem in the search for the most luminous clusters in the Galaxy located at significant distances; only the brightest members would be visible due to

the substantial extinction and distances through the Galactic disk, even in the infrared regime. This creates the appearance of a poorly populated cluster. Further, most, if not all, of these clusters and associations should be located inside the Galactic disk, leading to a substantial confusing stellar background population. Therefore, these previous searches are best suited to finding nearby, compact clusters far from the Galactic mid-plane.

In summary, previous cluster searches are insensitive to the extended angular sizes ($> 3'$) that would be typical of massive OB associations deep in the Galactic disk. The limited sampling of only the most luminous stars in these deeply veiled clusters, as well as confusion from the dense stellar background, would have prevented their detection. Therefore, the previous searches described above have not identified the most luminous clusters and OB associations within the Galaxy.

5.4   WMAP-identified Star Forming Complexes

To identify the locations of the most luminous OB associations, we use the identification of their parental SFCs from the WMAP and Spitzer GLIMPSE survey (Murray & Rahman 2010, Chapter 2). The WMAP mission provides all-sky, high sensitivity ($\sim \mu K$) microwave maps with five bands in the $23.5 - 90$ GHz range with a relatively large ($\sim 1°$) beam size. The five bands permit the separation of each of the Galactic "foreground" emission components; synchrotron emission, thermal dust emission, and free-free emission. The free-free emission almost entirely arises from reprocessed ionizing photons produced by the young, luminous (and massive) stars that found en masse in the most luminous young clusters and OB associations. Murray & Rahman (2010) identify free-free emission sources through the WMAP foreground map, finding that 14 sources are responsible for one-third of the total galactic ionizing luminosity. These regions are expected to be powered by young, very massive clusters or OB associations that contain sufficient O-type stars to produce the observed free-free

emission. Within these 14 sources, only two have had previously identified powering clusters and associations, specifically the Galactic Center region and NGC 3603 (Murray & Rahman 2010). Also notable is that amongst this list of the 13 most luminous regions, the regions hosting previously known massive clusters and OB associations, including Carina and Cygnus OB2, are not included. This suggests that these regions may contain clusters/associations more massive than those previously known.

The large ($> 1°$) radii of the WMAP sources leads to significant confusion along the line of sight, especially in the sources towards the inner Galaxy. Chapter 2 use the Spitzer GLIMPSE 8 μm emission maps and radio recombination line radial velocities to separate the large WMAP sources into SFCs for the 13 most luminous sources from the previous work, excluding the Galactic Center region. The observed SFCs differ in structure from the traditional model of a Strömgren sphere H II region: the complexes often appear as limb-brightened shells with the strongest nebular emission appearing on the large (with typical radii $5' < R < 30'$) shells rather than on the central region. Bubbles are blown by the centrally powering clusters, evacuating large regions surrounding them. Previously identified bright H II regions appear on the shells, indicating the locations of possible triggered clusters. Further, Murray & Rahman (2010) find that the majority of ionizing photons escape from the shells and produce diffuse ionization surrounding the entire complex, often with radii $> 1°$. While the classical Strömgren sphere interpretation of the SFC structure would suggest that the powering source should be located towards the center of the bright emission, this model suggests that the cluster is not expected to be coincident with the nebular emission for all but the youngest and smallest complexes.

Within the 13 investigated WMAP sources, Chapter 2 identify 40 discrete SFCs with distances ranging from 2.5 to 15 kpc and semimajor axes between $2'$ and $67'$. In some cases, the kinematic distance ambiguity is not resolved and two possible distances are identified. Since the WMAP sources extend to large radii in the Galactic

plane, we expect a great deal of confusion along the line of sight: while the measured luminosities of these sources suggest that they contain massive clusters, they also likely contain a number of less-massive sources along the line of sight. Due to the large fraction of ionizing photons escaping the central area of the complex, it is difficult a priori to determine which of the complexes are home to the massive clusters using ionization-based measures. In this work, we search for massive clusters and associations in all of the identified SFCs.

Previously, we have directed our attention to the most luminous of the SFCs, the Dragonfish Nebula. We developed a method using the 2MASS point source catalog to identify a candidate for the Galaxy's most luminous OB association, with a total stellar mass of 10^5 $M_\odot$ (Chapter 3). Follow-up NIR spectroscopy of bright stars within the candidate association confirmed the existence of Dragonfish Association with membership statistics consistent with the candidate's expected value (Chapter 4). This success of identifying and confirming the existence of the Dragonfish Association leads credence to our method used to identify the source. In this work, we use the same method of Chapter 3 to identify candidate clusters and OB association within the remaining SFCs from Chapter 2.

5.5   The 2MASS Selective Star Count Method

We refine the method of Chapter 3 to identify candidate clusters and associations within the SFCs using the line-of-sight extinction through the Galactic plane. This filters non-cluster stars from candidate members, allowing the associations to be identified in areas of significant point source contamination. Schematically, the process is as follows: We isolate stars matching the NIR colours of O-type stars at graduated extinction levels. We then use the on-sky density of point sources matching the colour cut to find overdensities consistent with the location of the SFC. Verifying from binned colour-colour and colour-magnitude diagrams that the candidate cluster

is not caused by a chance overdensity of projected Galactic structure based on the color distribution along the line of sight, we extract the candidate cluster's membership properties. We refer to this method as the 2MASS Selective Star Count (SSC) method, which we describe further.

5.5.1 The 2MASS Point Source Catalog

To identify members of the candidate cluster, we use the 2MASS Point Source Catalog (Skrutskie et al. 2006). The survey covers the entire sky with J (1.25 μm), H (1.65 μm), and K_S (2.16 μm) bands, enabling consistent coverage of the SFCs in both the northern and southern skies. We limit our searches to the point sources with photometric quality flags of A, B, or C, corresponding to a minimum signal-to-noise ratio of 5 for all of the J, H, and K_S bands. The 2MASS catalogue is complete to $J \leq 15.8$, $H \leq 15.1$, and $K_S \leq 14.3$ magnitudes in the absence of confusion. However, the areas we investigate are highly confused causing the completeness limit to be up to 1 magnitude brighter. This prevents the detection of less luminous objects that are expected to be cluster members based on the stellar initial mass function (IMF).

The typical FWHM of the 2MASS point sources is $2\rlap{.}''5$ and quoted magnitudes are measured with apertures of $4''$, which will cause significant confusion for the most compact clusters or the dense areas of more disperse OB associations (Skrutskie et al. 2006). Given the selected quality limit, these densely-packed confused sources will be excluded from our searches. Based on this constraint, we expect our search method to be insensitive to clusters with on-sky point source densities $\gtrsim 31$ per square arcminute due to overlapping apertures causing confusion. Within 1f the Galactic midplane, we find a total density of point sources in the target areas to be between 14 and 17 per square arcminute meeting the chosen quality cut. Therefore we expect such compact clusters to be readily identified by visual inspection of the images. In this sense, our SSC method is entirely complementary to search strategies of Bica et al. (2003), Dutra

et al. (2003) and Mercer et al. (2005). We discuss this further in the case of NGC 3603 in §5.6.1.

5.5.2 Extinction-derived Colour Selection

The hypothesized powering clusters and associations of the SFCs should exist at large extinctions due to their distance through the Galactic disk. We make use of this to identify the cluster candidates on the basis that all cluster members should be similarly extinguished along the line of sight. Our method for uncovering candidate clusters is to identify overdensities of stars with colors consistent with massive stars at extinction ranges consistent with the distances to the SFC being probed.

All of the SFCs were identified using techniques sensitive to ionizing flux with large ionizing luminosities ($Q_0 \gtrsim 10^{50.5}\,\mathrm{s}^{-1}$). The most luminous stars near the stellar upper mass limit have significantly smaller ionizing outputs ($Q_0 = 10^{49.6}\,\mathrm{s}^{-1}$ for an O3V star; Martins et al. 2005). The measured ionizing luminosities therefore require very large numbers of O-type stars to power them. For this reason we specifically search for overdensities of O-type stars with magnitudes and colours consistent with the distances and expected extinctions to the SFCs.

We use the NIR O-type star magnitudes and colours from Martins & Plez (2006). We note that the colours of all O-type stars in $J - H$ and $H - K_S$ are constant, with $J - H = -0.11$ and $H - K_S = -0.10$, as expected since these bands are located in the O-type stars Rayleigh-Jeans tails. These colours are, however, not unique to O-type stars; B- and early A-type stars are indistinguishable from O-type stars based on NIR colours alone to within the accuracy of the 2MASS color measurements (Chapter 3), and their relative abundance as compared to O-type stars may make them significant contributors to the total number of stars: $\sim 1/8$ ratio of O-type stars to B-type stars (Kroupa 2001). Only through their magnitudes can we make a distinction between O-, B- and A-type stars, given a particular distance and extinction.

We take the intrinsic colours of O-type stars and redden them to determine the colour cuts to make on the 2MASS stars. For the extinction law, we adopt that of Nishiyama et al. (2009), which gives the extinction ratios $\frac{A_J}{A_K} = 2.89$ and $\frac{A_H}{A_K} = 1.62$. We note that this is a departure from the canonical values for the extinction ratios due to a different power law slope for the relationship between extinction and wavelength ($A_\lambda \propto \lambda^\alpha$); this determination uses a slope $\alpha = -2.0$, while the previously accepted value is $\alpha = -1.61$ (Cardelli et al. 1989). The shallower slope has been found to be erroneous by Stead & Hoare (2009), who use an even steeper power law slope of $\alpha = -2.14$. The steeper slope of the extinction law changes the relationship between the NIR and visual; rather than a ratio of $A_V/A_K \sim 10$, the new ratio becomes $A_V/A_K \sim 16$ (Nishiyama et al. 2008). However, the difference in the extinction ratios between the different laws in the NIR bands is less than 20%, which is inconsequential in the candidate cluster identification because of the large color cuts used for the selection procedure.

We use the following relations for O-star extinctions:

$$A'_K(J - H) = 0.797(J - H) + 0.0877 \tag{5.1}$$

$$A'_K(H - K_S) = 1.66(H - K_s) + 0.166 \tag{5.2}$$

A 2MASS point source must meet these extinction criteria in both colors to be selected in the filtering process.

5.5.3 The Nearest Neighbour Algorithm

We analyze the density structure of 2MASS point sources using a nearest neighbour method, as described by Casertano & Hut (1985). This method samples each of the points within the chosen colour cut, providing an adaptive resolution, sampling the areas with more point sources more heavily than those areas with an absence of

point sources. From each of the points, we measure the distance r_j to the j-th nearest neighbour. We determine the local surface density, μ_j, with an unbiased estimator:

$$\mu_j = \frac{j-1}{\pi r_j^2} \tag{5.3}$$

with $j > 3$. From Casertano & Hut (1985), the standard deviation of the estimator is:

$$\sigma_j = \frac{\mu_j}{\sqrt{j-2}} \tag{5.4}$$

The specific value of j to be used is a function of the density of points within the sample; using too small a value of j samples only the most local variations of surface density, while using too large a value of j smooths over the smallest density variations. The on-sky point source density varies based on the location in the Galactic plane, the color-cut chosen, and the width of the color-cut. The typical on-sky densities of the point sources can vary by an order of magnitude through the test extinction range since fewer stars with very red colors are cataloged in 2MASS than bluer stars. Consequently, using a constant j value over the entire range would dramatically change the scale of structure highlighted. So for each color cut, we determine an optimal value for for j given a angular resolution based on the average number of point sources within a field:

$$j = \lfloor \frac{\theta_{cr}^2 N_*}{\Theta^2} \rfloor \tag{5.5}$$

where N_* and Θ are the total number of stars in and angular radius of the colour-selected 2MASS field, and θ_{cr} is the *characteristic resolution*, corresponding to the mean resolution across the selected field. For the purpose of this investigation, we choose a characteristic resolution $\theta_{cr} = 3.5'$ based on the resolution used to identify the Dragonfish Association from Chapter 3. At this characteristic resolution, typical j values range from 15 to 30 for most regions with extinction cuts of $\Delta A_K = 0.1$. The densities are gridded onto an oversampled ($d < 11''$), uniformly-spaced grid using a

Delaunay triangulation method from the Matplotlib python package (Hunter 2007) to simplify the analysis.

5.5.4   Candidate Identification

For each of the SFCs, we examine the surrounding $2°$ field with 0.1 steps in the A'_K color cut in the range of $0.0 < A'_K < 2.0$. We enlarge the surrounding field to $3°$ for SFCs with semi-major axes larger than $30'$. In each extinction step, we produce the nearest neighbour on-sky density map, and visually identify cluster candidates coincident with the on-sky position of the SFC position and the 8 μm morphology from Chapter 2.

Using small steps in the color cut allows for effective filtering of field stars from candidate clusters: while the typical point source density of unfiltered sources ranges from 14 to 17 sources per square arcminute (§5.5.1). The typical field densities within the color cuts range from 0.05–0.5 sources per square arcminute. The substantial decrease in the field source density due to the color filtering enables the detection of more diffuse clustering than has been possible in previous searches (§5.3).

Our adoption of sequential extinction cuts over the entire range allows for the filtering of effects due to the structure of the Galaxy itself. For instance, a significant effect of Galactic structure is the appearance of linear overdensity features above and below the Galactic plane caused by the limited thickness of the extinction-producing gas disk and also by the appearance of all thick disk and halo stars at a particular colour range (Figure 5.1). These large scale effects can be visually separated from localized overdensities with ease.

Once a candidate is identified, the extinction range is refined to enhance the prominence of the overdensity, and a final density map is produced. From this map we visually identify the candidate's geometric boundaries, including its centroid position, semi-major and semi-minor axes. Once the boundaries are chosen, we determine the

total number of enclosed sources, N_{TOT}. To constrain field contamination, we measure the mean (N_{BG}) and standard deviation (σ_{BG}) of the number of field stars surrounding the candidate in regions with the same area as the identified candidate.

To better distinguish between real clusters and asterisms, we analyze each candidate cluster with binned colour-colour and colour-magnitude diagrams as in Chapter 3. In each of the binned diagrams, we do not find substantial voids of point sources at colours along extinction vectors in either of the colour-colour and colour-magnitude diagrams. This would be a feature that is expected if the appearance of an overdensity at the selected colour cut was caused by localized extinction that is making point sources at that location appear redder. Using this as a diagnostic, we find that none of the overdensities appear to be consistent with the alternative hypothesis of a local extinction feature.

5.6 Candidate Clusters/Associations

In Table 5.1, we present the candidate clusters/associations identified within the SFCs. For SFCs with multiple candidates, an alphabetical key is used to distinguish between them. We define the extraction significance as:

$$\text{ES} = \frac{N_{TOT} - N_{BG}}{\sigma_{BG}} \tag{5.6}$$

with N_{TOT}, N_{BG}, and σ_{BG} as defined in §5.5.4.

Two of the candidate associations (those within SFC 8 and 30) have extraction significance values of less than unity; these candidates are identified solely based on their morphology as compared to the SFC and have significant large scale structure in the field surrounding them that produces large background variations.

The candidates have characteristic radii between $3'$ and $20'$, with a median of $\sim 7'$. This is consistent with the sensitivity of the SSC method to larger diffuse structures

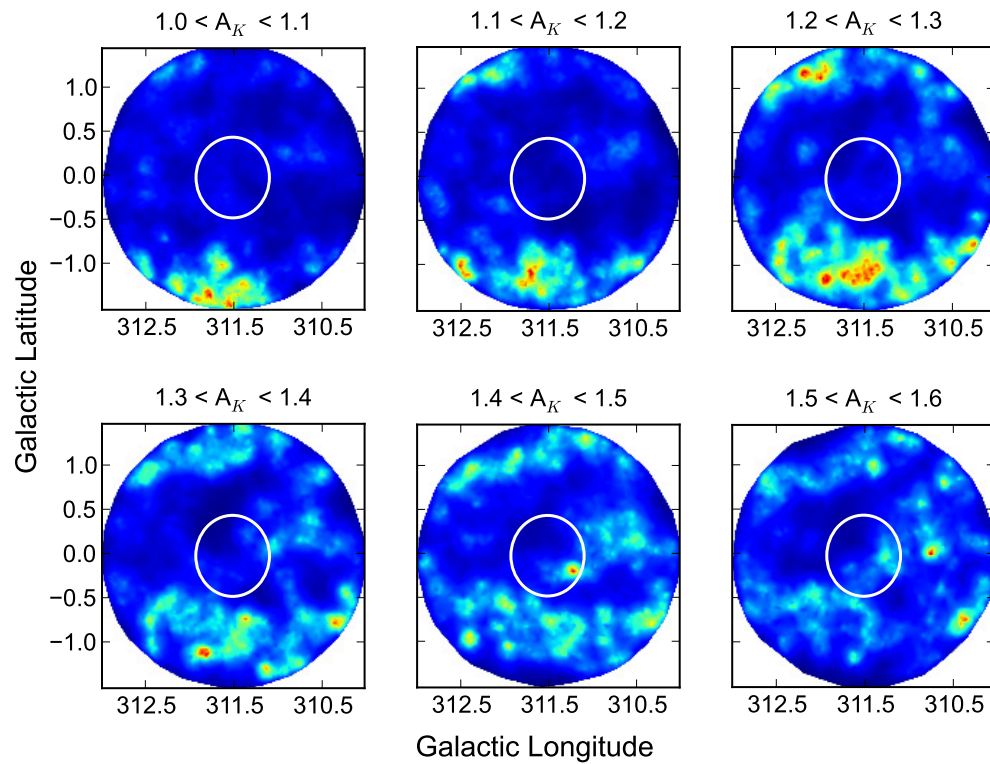Figure 5.1: 2MASS Point Source Density Maps at the location of SFC 31 (white circle) with extinction cuts between A_K = 1.0 and 1.6 (left to right, top to bottom). Galactic structure effects produce the long horizontal streak-like features that appear in the first extinction cut symmetrically 1°above and below the galactic plane and narrow in subsequent cuts. These features are visually filtered from the selection process.

than in previous cluster searches (see §5.5.4). Accordingly, these candidates would not have been identified in the previous searches. While the SSC method is more sensitive to diffuse structures, the ellipses are chosen to contain the most prominent areas of the overdensity and do not necessarily represent the outer boundaries of the clusters. The typical extinction cut of the candidates has a range of $\Delta A_K \sim 0.2$. We find that K-giants are the primary contaminants of all the new candidates, since they tend to be the dominant population of visible red stars in the 2MASS survey (Robin et al. 2003).

We present the stellar density diagrams and the $8\,\mu$m images from the Spitzer GLIMPSE or Midcourse Space Experiment (MSX) in Figures 5.2 to 5.8. These images indicate the SFC location from Chapter 2 and the candidate cluster location.

Since the candidate extinctions were determined independently from the distance to their host SFC, we can use the distance to extinction relationship as a consistency check. We present this relationship in Figure 5.9, indicating the extinction ranges of the candidates with the kinematic distances determined from Chapter 2, and the modelled extinction from Marshall et al. (2006) using the SFC kinematic distance from Chapter 2 in Table 5.1. We also indicate the possible distances (and model extinctions) of SFCs without a kinematic distance ambiguity solution and the location of the Dragonfish association from Chapter 3. We find the correlation coefficient of the two extinctions to be 0.75 when using the more consistent distance in the cases of the distance ambiguity, showing that they are statistically significantly correlated. This correlation provides strong evidence for the reality of the candidate clusters. For sources with a distance ambiguity, the modelled extinction provides support in favour of one of the two possibilities.

5.6.1   Previously Identified Clusters

An important measure of the success and the sensitivity of the SSC method is identifying known massive clusters and associations within 2MASS. For this purpose, we use

the cases of NGC 3603, the powering cluster of SFC 28, and Cygnus OB2. We discuss these two cases below.

NGC 3603

A notable cluster that was not detected by the SSC method is the massive cluster within NGC 3603 that powers SFC 28. This very compact cluster is mostly contained within its inner 33″, requiring high spatial resolution to discern individual members (Stolte et al. 2004). At the resolution of 2MASS, the central cluster is highly confused, as can be seen in Figure 5.10. This prevents individual sources from being identified as point sources, and hence, missing from the 2MASS PSC. In fact, only 17 point sources are identified in the central region that pass the desired quality cut for the SSC method (inset of figure 5.10). Further filtering point sources to those with colours corresponding to O-type stars at the extinction of NGC 3603, we are restricted to 12 point sources. Because of the compact area in which they reside, this is seen as an increase of the point source density at the corresponding extinction cut, but not above the natural variation of point sources matching these colours. In redder color cuts, this region is seen as a void in point source density. This is consistent with our expectation that the SSC method is insensitive to compact clusters, such as those that can be identified visually.

Despite this, the SSC method is useful to investigate the entire area of the NGC3603 natal cloud for more diffuse secondary clusters or associations. We suspect that these are the candidate clusters we identify in SFC 28, on the edge of the region. They appear at a significantly higher extinction than NGC 3603 ($\Delta A_K \sim 0.4$). If they are not unrelated regions farther across the Galactic plane, they could be regions deeply embedded within the cloud, consistent with the CO morphology from Grabelsky et al. (1988). In either case, these candidates are not the powering source of SFC 28.

Table 5.1. Candidate Clusters/Associations

SFC	l (deg)	b (deg)	D^b (kpc)	smaj (arcmin)	smin (arcmin)	PA (deg)	j	A'_K Min	A'_K Max	A_K^c (Model)	N_{TOT}	N_{BG}	σ_{BG}	ES
5a	23.108	-0.439	4.9, (10.8)	6	4	-52	40	0.5	0.7	1.0, 2.4	106	57	18	2.7
5b	22.928	-0.252	4.9, (10.8)	3	2	-24	40	0.5	0.7	1.1, 1.4	32	18	7	2.0
6	23.389	-0.187	9.2	9	7	63	29	0.6	0.7	1.6	84	34	13	3.8
7a	23.993	0.110	5.8, (9.8)	5	3	0	37	0.5	0.6	1.4, 2.2	18	8	4	2.3
7b	23.600	0.166	5.8, (9.8)	7	4	0	37	0.5	0.6	0.7, 1.7	38	19	9	2.2
8	24.152	-0.374	10.3	13	11	-68	114	1.7	2.0	2.3	392	315	137	0.6
10	25.058	0.165	6.1	15	11	72	108	1.5	1.7	1.2	690	341	165	2.1
12	25.995	0.127	8.8, (6.5)	7	5	0	107	1.6	1.8	1.8, 1.4	184	66	34	3.4
17	30.610	0.167	6.3	24	16	-13	41	0.6	0.7	0.7	409	266	61	2.3
19	34.294	0.220	2.2	9	5	-30	27	0.6	0.7	0.6	48	24	10	2.3
22	37.114	-0.577	10.5	7	4	-41	37	1.5	1.6	2.2	55	18	11	3.2
23	38.294	-0.004	3.5, (9.9)	6	6	0	35	1.3	1.4	1.1, 2.4	48	24	13	1.9
25	49.318	-0.215	5.7	7	6	-38	155	0.6	0.8	0.6	198	124	28	2.6
26	283.976	-0.868	4	19	10	-79	61	0.4	0.5	0.2	278	196	47	1.7
28a	291.177	-0.952	7.4	7	6	0	121	0.8	1.0	0.7	175	92	28	3.0
28b	292.238	-0.666	7.4	11	9	-23	121	0.8	1.0	1.0	333	193	47	3.0
29[a]	298.550	-0.720	9.7	11	10	0	100	1.0	1.4	1.0	897	491	102	4.0
30	311.034	0.454	3.5	7	4	67	63	0.4	0.5	0.9	43	34	10	0.9
31	311.539	0.347	7.4	8	7	-63	48	0.3	0.4	1.2	87	45	13	3.4
33	328.013	-0.568	3.7	23	7	-7	193	0.4	0.6	0.3	735	502	138	1.7
34a	333.514	-0.080	3.4	6	5	0	604	0.3	0.7	0.2	473	299	70	2.5

Table 5.1 (cont'd)

| | | | | | | | | A'_K | | $A_K{}^c$ | | | | |
SFC	l (deg)	b (deg)	D^b (kpc)	smaj (arcmin)	smin (arcmin)	PA (deg)	j	Min	Max	(Model)	N_{TOT}	N_{BG}	σ_{BG}	ES
34b	332.931	-0.569	3.4	17	7	-23	604	0.3	0.7	0.3	1766	1239	212	2.5
36	336.537	-0.162	5.4, (10.2)	6	4	-50	26	1.0	1.1	0.8, 2.0	36	12	6	4.1
37	337.243	-0.011	10.9	10	6	9	495	1.3	1.8	1.6	781	460	91	3.5
38	337.787	-0.382	3.5	9	7	-60	44	0.4	0.5	0.9	91	50	16	2.6
39	338.361	0.197	13.3, (2.5)	7	7	90	14	1.8	1.9	1.8, 0.2	24	11	5	2.4

[a]Candidate cluster properties from Chapter 3

[b]Where a kinematic distance ambiguity exists, we list the distance most consistent with candidate extinction first, and the less consistent distance in parentheses.

[c]Model extinction from Marshall et al. (2006)

Cygnus OB2

To ensure that the SSC method can identify known OB associations, we use Cygnus OB2 as a test case. This association, located in the outer Galaxy, has a substantially reduced background stellar population in comparison to the clusters in the inner galaxy. Therefore, the association can be identified using total stellar density without extinction cuts, as has been done by Knödlseder (2000).

Using the method, we easily identify Cygnus OB2 (Figure 5.11) at an extinction range of $0.5 < A_K < 0.8$, with position, structure and extinction consistent with the values determined by Knödlseder (2000). The typical background level in the field is 0.3–0.6 per square arcminute, approximately 10%–20% of the peak density of the association. If we choose the boundary of the cluster to be the isodensity contour at 1.2 per square arcminute, the average rate of line-of-sight contaminating sources within the association boundaries is < 0.28, allowing for high-yield extraction of association members from the field.

5.6.2   Statistical Significance

In the previous subsection, we have discussed the success and sensitivity of the SSC method using previously identified clusters and associations. However, the problem that has plagued previous cluster candidate identification methods has been the overwhelming number of false positives. We conduct a test to determine the rate of false positive candidate identifications through the SSC method.

We generate a list of 40 artificial SFCs with positions, dimensions and position angles randomly chosen to match the distribution of actual SFCs on the sky: the artificial locations are generated from a uniform random distribution between $270° < l < 90°$ and $-1° < b < 1°$. The position angles, semimajor axes and the axial ratios were generated by producing linearly interpolated cumulative distribution functions from the real SFC list. Using the SSC method, we attempt to identify "candidate

Figure 5.2: Spitzer GLIMPSE $8\,\mu$m image (left) and the on-sky density diagrams (right) of the 2MASS point sources. The source and extinction ranges are indicated above each figure. The green solid ellipse indicates the location of the SFC from RM10, while the red dashed ellipses indicate the location of the candidate clusters. The colour bar indicates the point source density in sources per square arcminute.

Figure 5.3: Spitzer GLIMPSE 8 μm image (left) and the on-sky density diagrams (right) of the 2MASS point sources. The source and extinction ranges are indicated above each figure. The colour bar and annotations are the same as Figure 5.2.
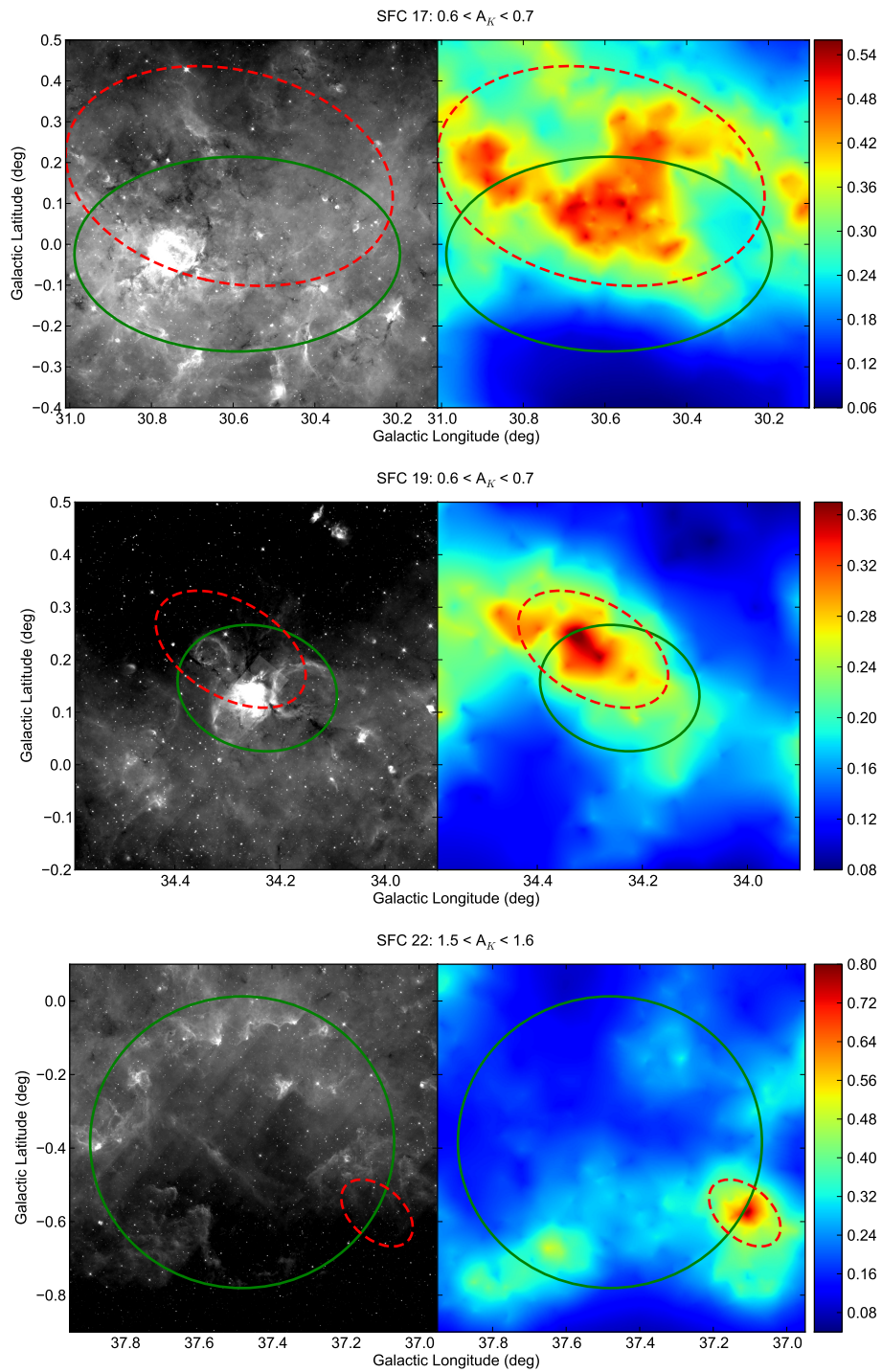
Figure 5.4: Spitzer GLIMPSE 8 μm image (left) and the on-sky density diagrams (right) of the 2MASS point sources. The source and extinction ranges are indicated above each figure. The colour bar and annotations are the same as Figure 5.2.
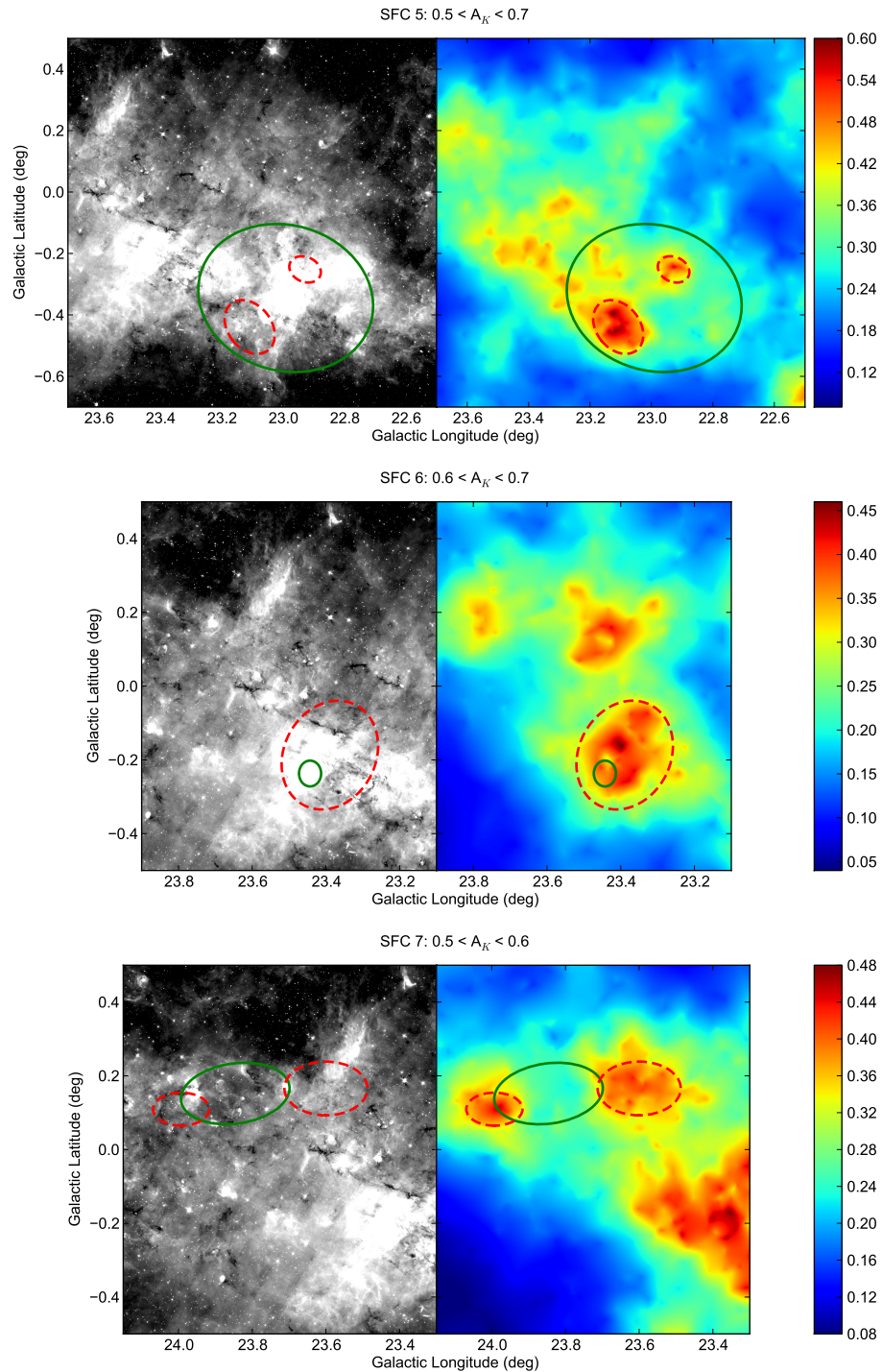
Figure 5.5: Spitzer GLIMPSE 8 μm image (left) and the on-sky density diagrams (right) of the 2MASS point sources. The source and extinction ranges are indicated above each figure. The colour bar and annotations are the same as Figure 5.2. We use the MSX 8 μm image for SFC 26 due to Spitzer GLIMPSE coverage limits.
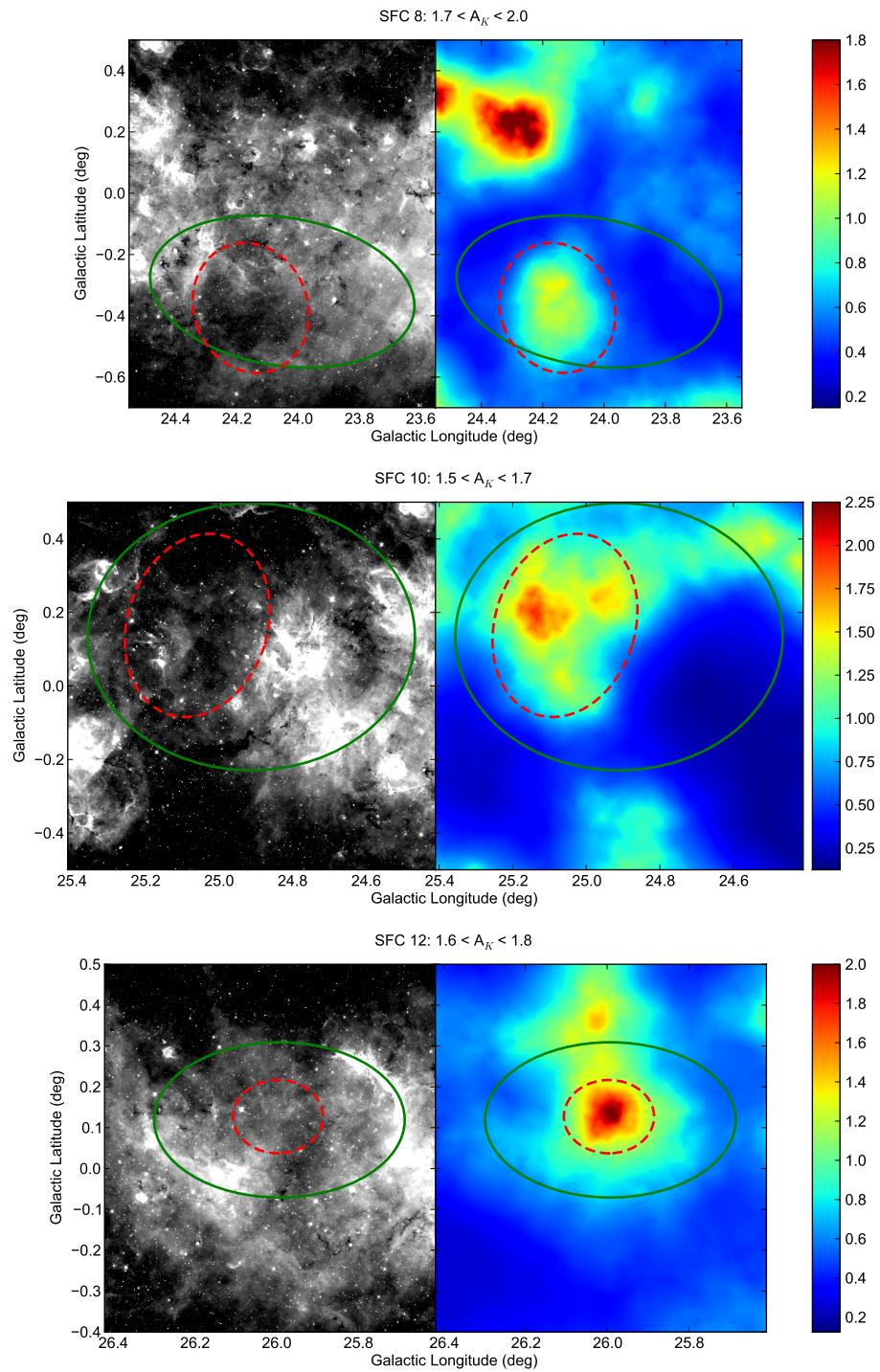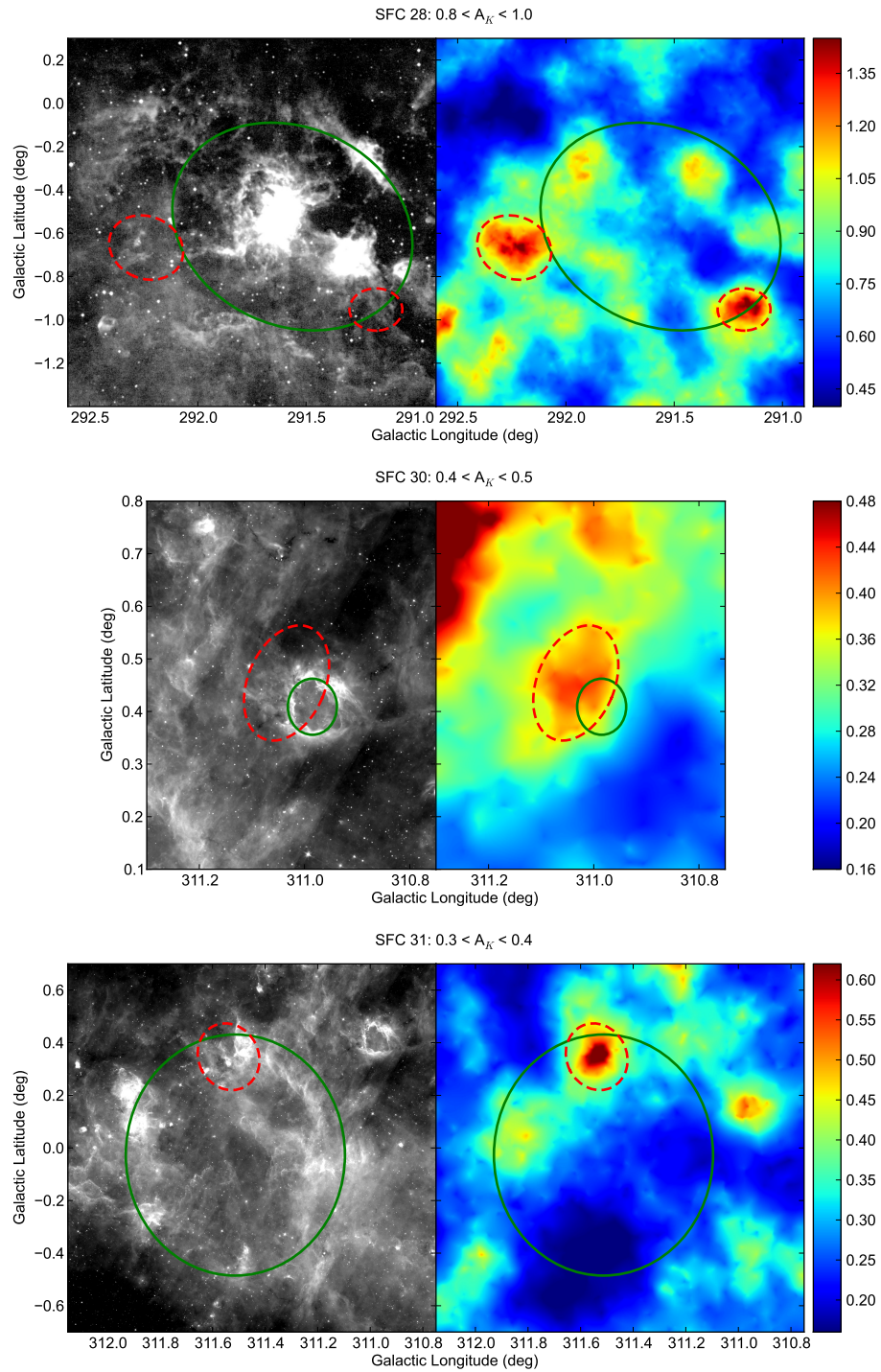
Figure 5.6: Spitzer GLIMPSE 8 μm image (left) and the on-sky density diagrams (right) of the 2MASS point sources. The source and extinction ranges are indicated above each figure. The colour bar and annotations are the same as Figure 5.2. We use the MSX 8 μm image for SFC 28 due to Spitzer GLIMPSE coverage limits.
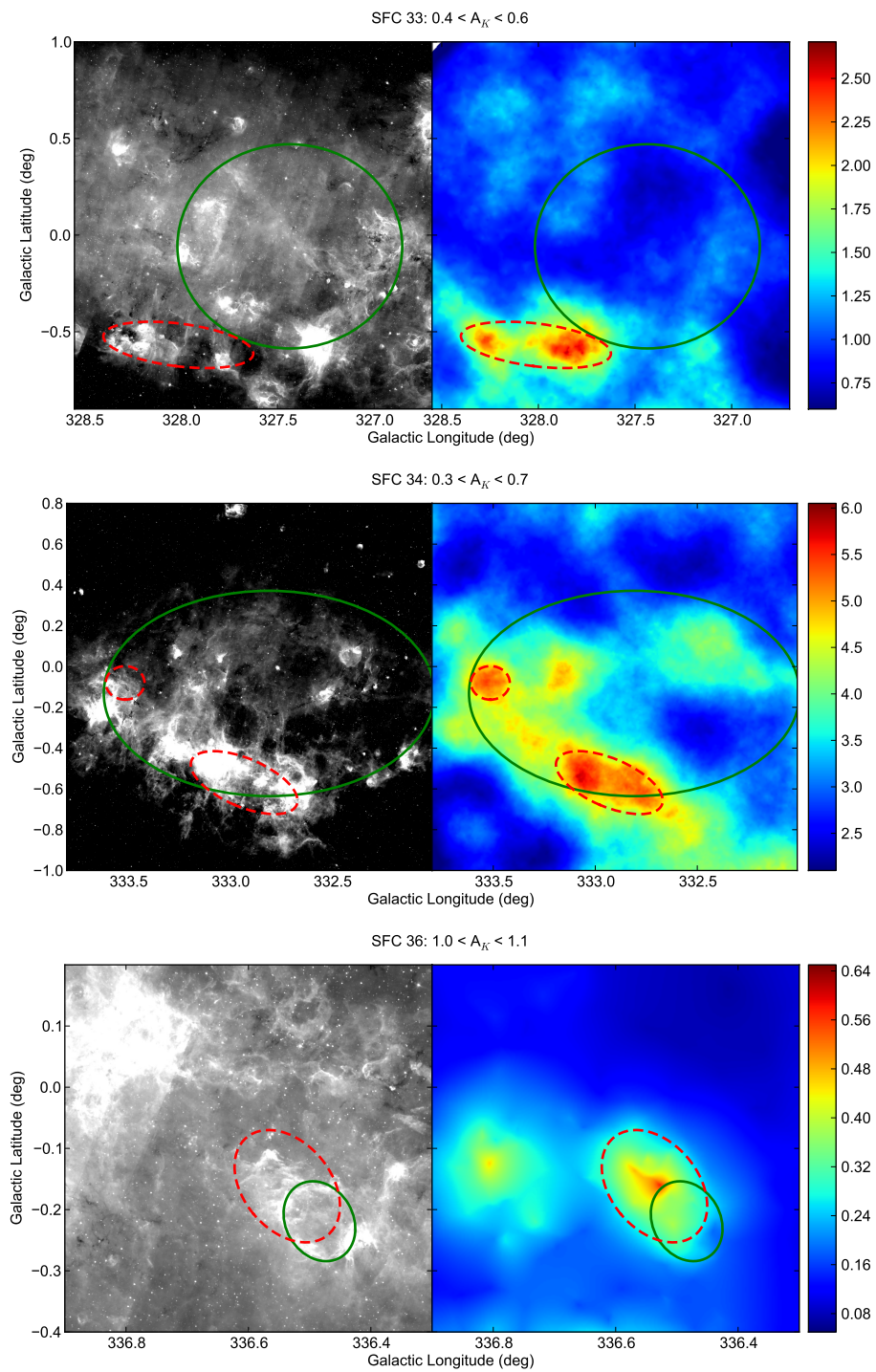
Figure 5.7: Spitzer GLIMPSE 8 μm image (left) and the on-sky density diagrams (right) of the 2MASS point sources. The source and extinction ranges are indicated above each figure. The colour bar and annotations are the same as Figure 5.2.

Figure 5.8: Spitzer GLIMPSE 8 μm image (left) and the on-sky density diagrams (right) of the 2MASS point sources. The source and extinction ranges are indicated above each figure. The colour bar and annotations are the same as Figure 5.2.
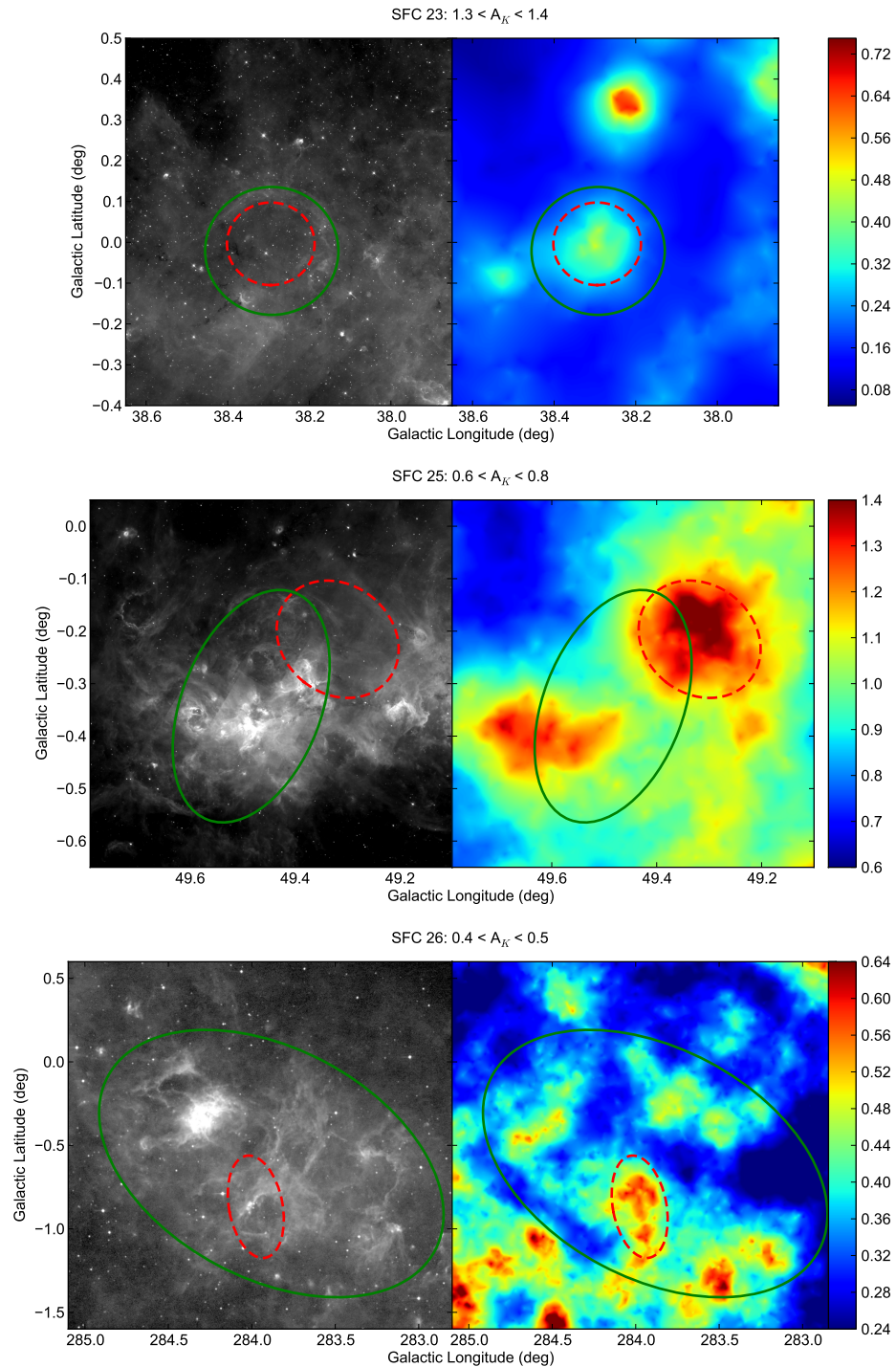
Figure 5.9: A comparison between the extinction range of all identified candidate clusters to the kinematic distance of their host SFC from Chapter 2 (left) and with the model extinction from Marshall et al. (2006, right). The local distance to extinction relationship ($A_K/D = 0.1$ mag kpc^{-1}) is indicated with the dashed gray line on the left. The diagonal is indicated with the gray line on the right. The connected red ranges indicate the SFCs without a kinematic distance ambiguity resolution. The green range indicates the location of the Dragonfish Association properties from Chapter 3. As no information about the kinematic distance was used in identifying the candidates, the correlation between the candidate and model extinction is not caused by a bias in the SSC method.

clusters" for these artificial SFCs, with the same criteria as in §5.5.4. This test was conducted five times. From the five lists of artificial SFCs, the rate of identified candidates is 3.0 ± 0.6, which is a much smaller yield than the 22 actual SFCs with identified candidates. It should be noted that the artificial candidates may be actual clusters or associations related to less luminous WMAP sources on the sky from Murray & Rahman (2010).

In addition to the false positive test, the correlation between the modelled extinction and the candidate extinction (§5.6; Figure 5.9) provides strong support for the reality of the clusters identified by the SSC method. Finally, the spectroscopic confirmation of the Dragonfish Association (Chapter 4) provides additional, circumstantial evidence of the clusters identified by this method. These independent lines of evidence indicate that most ($\sim 86\%$) of our cluster candidates are indeed associated with their host SFCs, and are their dominant engines of ionization and dynamical power.

5.7 Mass & Luminosity Estimates

We estimate the physical properties of the candidate clusters to assess if the identified candidates can produce the observed free-free flux of their parent WMAP source (Table 5.2). We note that the stated boundaries from the candidate identification and extraction method are not the absolute boundaries of the clusters (§5.6). Consequently, the extracted clusters will likely exclude the diffuse outskirts of the clusters or associations, especially when the background level of contaminating sources is particularly high. Such diffuse populations can produce significant contributions to the total complex population as has been recently observed in the Carina Nebula where previously undiscovered OB stars were identified in X-ray observations, doubling the massive stellar population (Povich et al. 2011b). Also note that we do not make any correction for the multiplicity of sources.
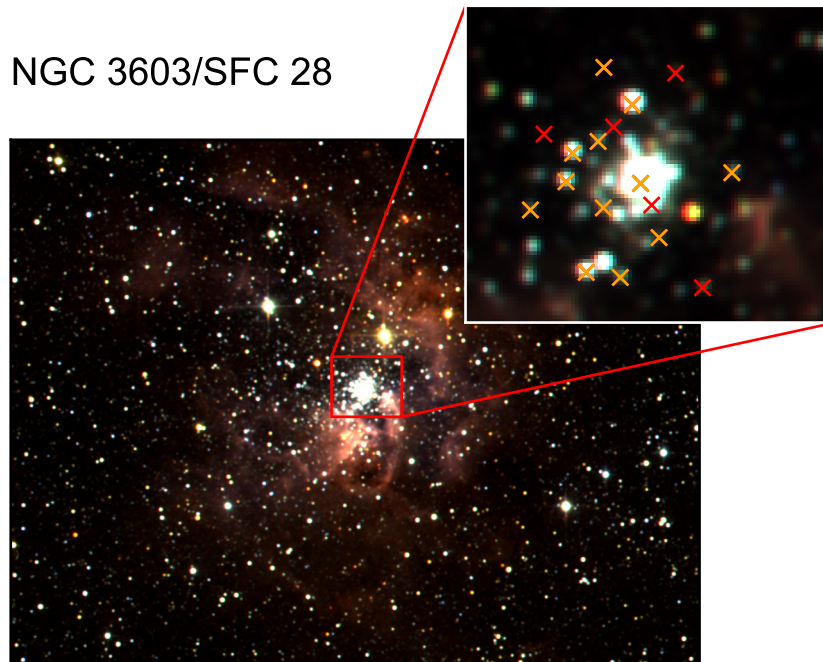
Figure 5.10: NGC 3603 region from 2MASS in J (blue), H (green) and K (red) with the central cluster magnified (inset). The crosses indicate the locations of the only 2MASS point sources that pass the required quality cut within $33''$ of the cluster centre. The orange crosses are the point sources that meet the colour cut of the cluster, while those in red are the sources that do not.
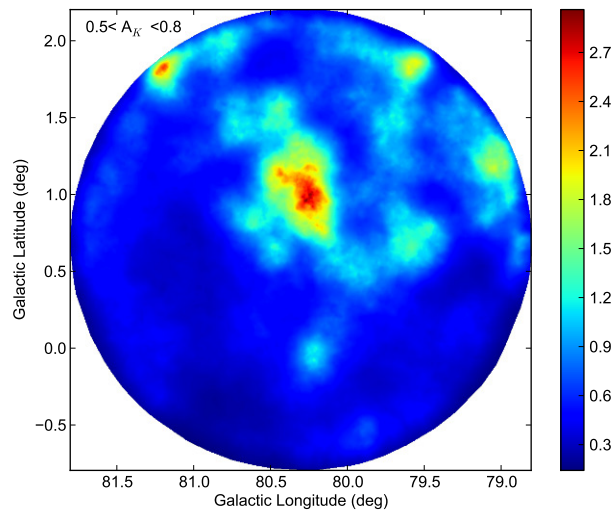
Figure 5.11: The on-sky density diagram of 2MASS point sources between $0.5 < A_K < 0.8$ in the Cygnus OB2 region. The colour bar indicates the point source density in sources per square arcminute

We estimate the least massive stars that are extracted in the candidate clusters by using the observed 2MASS K_S-band magnitude limit from §5.5.1, with the mean extinction range of the candidate and the kinematic distance of the SFC from Chapter 2. In cases where the kinematic distance is ambiguous, we use the distance most consistent with the Marshall extinction (see Figure 5.9). We use the absolute magnitude tabulations from Martins & Plez (2006) for O-type stars and from Pickles (1998) for all other stars. We also use Martins et al. (2005) for the O-type star mass determinations and Andersen (1991) for all other stars. From the mass of the least massive star and the number of stars extracted in the candidate cluster ($N_{tot} - N_{BG}$ in Table 5.1), we determine a total cluster mass (M_*) and ionizing luminosity (Q_0) integrating over an IMF. To maintain consistency with previous work, we use the modified version of the Muench et al. (2002) IMF and the mass-to-ionizing luminosity conversion from Murray & Rahman (2010). This conversion factor assumes a fully-sampled IMF with

all stars on the main sequence, rather than summing the ionizing luminosity from each individual source in the cluster. The dominant source of error in the determination of the cluster mass is the chosen IMF, which is discussed in detail in Murray & Rahman (2010). However, the total ionizing luminosity of the cluster is more reliable, since the bulk of the ionization comes from the most massive stars, and consequently is only dependent on the upper-end slope of the IMF. For the ionizing luminosity, the dominant source of error is the uncertainty in the number of point sources from the extraction process, let alone the possible effect of multiplicity that has not been taken into account.

Finally, assuming $\nu = 90$ GHz, we determine the expected free-free flux contribution of the candidate. We also visually classify the candidates based on their location with respect to the identified SFC and the 8 μm morphology. We indicate that they are either "centrally-located" if they appear towards the centre of a shell-like structure or the entire SFC, or "shell-located" if they appear on the edge of a shell or SFC.

In Table 5.1, N_{sub} is the number of sources in the candidate cluster once the background level is subtracted ($N_{TOT} - N_{BG}$). We include the Dragonfish Association properties from Chapter 3. For the WMAP sources with multiple identified candidate clusters, we include totals for the cluster masses, ionizing luminosities and free-free emission fluxes.

We note that the latest stellar type of all extracted sources is either O-, B- or A-type stars. Therefore all sources extracted from the clusters will have similar colours in the NIR bands since they are in the Rayleigh-Jeans tail. Therefore, we do not expect cluster members to be excluded based on have colors that fall outside of the color cut.

The total cluster masses of the candidates range from 150 to 10^5 M$_\odot$. As suspected, some of the candidates (and SFCs) are low mass intervening clusters. In these cases, the estimated ionizing luminosity and free-free emission flux are overestimated as the IMF is poorly sampled on the upper end and the mass-to-ionizing luminosity

conversion breaks down. This has been discussed in detail by Kennicutt et al. (1989). Therefore the free-free flux contribution from these clusters will be much smaller than those tabulated since the mass-to-ionizing luminosity relation is unsuitable for a poorly sampled IMF. By ionizing luminosities of log $Q_0 \sim 50$ or cluster masses greater than 1600 $M_\odot$, > 10 O-type stars are required to ionize the complex and the IMF should be sufficiently well sampled to allow the accurate use of the mass-to-ionizing luminosity relationship (Martins & Plez 2006).

We find the sum of the estimated free-free emission fluxes to be roughly consistent with the WMAP measurement for G34, G37, G298, G327, and G337. For G30 and G49, the identified candidates appear to be centrally located, but the smaller-than-expected mass, ionizing luminosity, and free-free flux most likely come from a diffuse component of the cluster/association. Should these candidates be confirmed, an in-depth investigation, possibly in the X-rays, will be required to identify the extended or diffuse population. For G283 and G327, only shell-located regions are identified. In the case of G327, the lack of sharp shell structure in the bubble in 8 μm and 2MASS stellar overdensity structure (see Figure 5.7, top panel) may indicate that the original driving cluster of the bubble has evolved beyond its ionizing luminous stage, and the ionizing population of the complex is a more diffuse, triggered population. In source G291, we identify two possible triggered clusters; however the dominant cluster in the region, NGC3603, has been previously identified and was not detected by the SSC method (see §5.6.1).

In some cases, such as G332, multiple candidates are identified at the same (or reasonably close) distances and extinction ranges. These candidates are likely associated and may represent more widespread star formation across a giant molecular cloud. Accordingly, the total embedded cluster mass in these situations would be the sum of the individual "clustered" regions, plus the diffuse component that we do not recover from the extraction process.

The total expected free-free emission luminosities of the candidates in G24 and G332 substantially exceed the measured flux from WMAP. There are at least six possibilities to account for this: (1) one or more of the candidates within the WMAP source are false positives, (2) the extraction has overestimated the number of member stars by a substantial fraction, (3) the kinematic distance to the SFC is closer than the actual distance, (4) the cluster is older than 3.9 Myr, where the most massive stars have left the main sequence (Bressan et al. 1993), (5) a higher-than-average fraction of the ionizing photons are absorbed by dust, and (6) the ionizing photons escape the Galaxy through a chimney. To determine whether it is case (1) or (2), follow-up astrometric or spectral confirmation of the cluster is required. In case (3), the distances to the ionizing sources can be unambiguously determined though trigonometric parallax, if strong maser sources are available. In case (4), the evolutionary state of the candidate requires accurate determination of the spectral type of candidate sources to determine the earliest stars in the cluster and their individual evolutionary state. If so, these clusters may harbor young core-collapse remnants of very massive stars, such as black holes or magnetars, and should be searched for counterparts in the radio and X-rays.

With these caveats, we find candidates to central powering clusters that can account for the observed WMAP free-free emission flux within G24, G30, G34, G37, G49, G298, G332, and G337. Of the original WMAP sources investigated in Chapter 2, only G10 does not have any candidate clusters identified through this method, either centrally located or triggered.

Table 5.2.   Estimated Physical Properties of Candidate Clusters/Associations

WMAP Source	SFC	D (kpc)	$\overline{A_K}$ (mag)	N_{sub}	Morphology Flag[a]	Latest Stellar Type	M_{min} ($M_\odot$)	Log M_*[b] ($M_\odot$)	Log Q_0[b] (s^{-1})	S_{ff} (Est)[b,c] (Jy)	S_{ff} (WMAP)[c] (Jy)
G24	5a	4.9[†]	0.6	49±18	C	B9V/A0V	2.6	3.0	[49.8]	[144]	
	5b	4.9[†]	0.6	14±7	C	B9V/A0V	2.6	2.4	[49.2]	[41]	
	6	9.2	0.65	50±13	C	B4V	5.5	3.4	50.2	115	
	7a	5.8[†]	0.55	10±4	S	B9V	2.7	2.3	[49.1]	[22]	
	7b	5.8[†]	0.55	19±9	S	B9V	2.7	2.6	[49.4]	[42]	
	8	10.3	1.85	77±137	C	O9.5V/B0V	15	4.2	51.0	576	
	10	6.1	1.6	349±165	C	B5V	5	4.2	51.0	1610	
	12	8.8[†]	1.7	118±34	C	B0.5V	13	4.3	51.1	985	
Total								*4.8*	*51.6*	*3535*	*1377*
G30	17	6.3	0.65	143±61	C	B9V	2.7	3.5	50.3	267	1585
G34	19	2.2	0.65	24±10	C	A8V	2	2.5	[49.3]	[243]	285
G37	22	10.5	1.55	37±11	S	B0V	14	3.9	50.7	241	
	23	3.5[†]	1.35	24±13	C	B9V/A0V	2.6	2.7	[49.5]	[138]	
Total								*3.9*	*50.7*	*380*	*244*

Table 5.2 (cont'd)

WMAP Source	SFC	D (kpc)	$\overline{A_K}$ (mag)	N_{sub}	Morphology Flag[a]	Latest Stellar Type	M_{min} (M⊙)	Log M_*[b] (M⊙)	Log Q_0[b] (s⁻¹)	S_{ff} (Est)[b,c] (Jy)	S_{ff} (WMAP)[c] (Jy)
G49	25	5.7	0.7	74±28	C	B9V	2.7	3.2	50.0	169	458
G283	26	4	0.45	82±47	S	A0V	2.5	3.2	50.0	341	848
G291	28a	7.4	0.9	83±28	S	B8V/B9V	3	3.3	50.1	130	
	28b	7.4	0.9	140±47	S	B8V/B9V	3	3.5	50.3	218	
Total								*3.7*	*50.5*	*348*	*688*
G298[b]	29	9.7	1.1	406±102	C	O9.5V	16.5	5.0	51.8	307	313
G311	30	3.5	0.45	9±10	C	A1V	2.3	2.2	[49.0]	[44]	
	31	7.4	0.35	42±13	S	B9V	2.7	2.9	[49.7]	[57]	
Total								*3.0*	*49.8*	*102*	*766*
G327	33	3.7	0.5	233±138	S	A1V	2.3	3.6	50.4	1014	943
G332	34a	3.4	0.5	174±70	C	A1V	2.3	3.5	50.3	899	
	34b	3.4	0.5	527±212	C	A1V	2.3	3.9	50.7	2714	
Total								*4.1*	*50.9*	*3613*	*1787*

Table 5.2 (cont'd)

WMAP Source	SFC	D (kpc)	$\overline{A_K}$ (mag)	N_{sub}	Morphology Flag[a]	Latest Stellar Type	M_{min} (M☉)	Log M_*[b] (M☉)	Log Q_0[b] (s⁻¹)	S_{ff} (Est)[b,c] (Jy)	S_{ff} (WMAP)[c] (Jy)
G337	36	5.4†	1.05	24±6	C	B9V	2.7	2.7	[49.5]	62	
	37	10.9	1.55	321±91	C	B0V	14	4.8	51.6	1944	
	38	3.5	0.45	41±16	S	A1V	2.3	2.8	[49.6]	[201]	
	39	13.3†	1.85	13±5	C	O8.5V	20	3.6	50.4	86	
Total								4.8	51.6	2293	2239

Note. — The Q_0 and S_{ff} values enclosed in brackets are likely incorrect due to poor sampling of the IMF (described in §5.7.)

[a]C refers to a candidate that appears as a central cluster, S refers to a candidate that appears embedded in a shell structure.

[b]Candidate cluster properties from Chapter 3

[c]The error on these parameters scale linearly with the error on N_{sub}

[d]The flux measurements are given at 90 GHz.

†The kinematic distance that is most consistent with the expected average distance-to-extinction ratio is used.

5.8 Completing the Upper End of the Galactic Cluster Mass Function

Our knowledge of the upper end of the Galactic cluster mass function (CMF) has long been recognized as incomplete. This has been established through comparison to galaxies with similar masses and star formation rates as the Milky Way (Larsen & Richtler 2000; Larsen 2009), and comparing the known cluster/association population with the inferred H II mass function (McKee & Williams 1997; Hanson & Popescu 2008). These comparisons show that up to 90% of young, massive clusters and OB associations are yet to be found.

Table 5.3 presents the current census of known massive, young ($\lesssim 4$ Myr) clusters and OB associations in the Galaxy, including the massive candidates from this work, where we include all known clusters and associations with masses similar to or greater than 10^4 M$_\odot$. The age limit of 4 Myrs ensures that even the most massive stars, which produce the bulk of the ionizing luminosity, are still on (or near) the main sequence Murray & Rahman (2010). This effect is prominently seen in the case of Westerlund 1, where despite the large cluster mass ($> 10^{4.7}$ M$_\odot$) and rich population of Wolf-Rayet and late-O type stars (Brandner et al. 2008), the cluster is not detected as a prominent free-free emission source in WMAP (Murray & Rahman 2010). If the candidates from this work are confirmed with the minimum masses estimated, the census of young, massive clusters and OB associations is doubled with 7 new candidates.

Notably, the age restriction of the census excludes the red supergiant clusters recently discovered with ages > 10 Myrs and masses $> 10^4$ M$_\odot$ (Figer et al. 2006; Davies et al. 2007; Clark et al. 2009). The massive stellar component of these clusters have entirely evolved off the main sequence, and consequently the clusters have an insignificant ionizing luminosity. This is corroborated by the lack of any reprocessed free-free emission towards the clusters from the WMAP free-free emission maps

(Murray & Rahman 2010).

5.8.1 Estimates of Completeness

The completeness of the census can be estimated through CMFs from previous work for other galaxies in the visible wavebands, such as the Antennae and M83 (Fall et al. 2009; Chandar et al. 2010). Ivanov et al. (2010) estimate that the Milky Way contains $\geq 81 \pm 21$ clusters with masses of $10^4 - 10^5$ M$_\odot$ and ages up to $\sim$25 Myr, assuming all clusters within 6 kpc are known (Piskunov et al. 2008). This estimate can be scaled to our 4 Myr age limit using the age distribution from Chandar et al. (2010, $\frac{dN}{d\tau} \propto \tau^{-1}$) with a minimum age of 1.3 Myr based on the youngest clusters observed. The scaled estimate is $\gtrsim 31$ clusters in the Milky Way, of which Larsen (2009) would predict that 8 are bound.

Another independent measure of completeness is a comparison to the H II region luminosity functions of other galaxies. We compare to the H II region luminosity functions from Kennicutt et al. (1989), using a minimum Hα luminosity of $L(H\alpha) > 10^{38.6}$ erg s^{-1} which is similar to the 10^4 M$_\odot$ cutoff. In the most analogous cases to the Milky Way in terms of morphological class, NGC 6384 (an Sb galaxy) contains 38 sufficiently luminous H II regions, while NGC 7741 (an SBc galaxy) contains 17. Smith & Kennicutt (1989) show that the H II luminosity function of the Milky Way is comparable to those of Sb-c galaxies, indicating that using the Sb-c galaxies as a guide is a valid estimation of the total young, massive clusters in the Galaxy.

Both of these estimates of the total number of massive ($> 10^4$ M$_\odot$) clusters/associations in the Galaxy are comparable to 14, the number of associations in our census, of which seven are presented here (Table 5.3). Since the estimates of the number of young, massive clusters expected is between 17-38, we infer from this that our knowledge of young, massive clusters in the Milky Way is now within approximately a factor of two of being complete.

Table 5.3.   Census of Massive ($\gtrsim 10^4$ M$_\odot$), Young ($\lesssim 4$ Myr) Clusters & OB Associations in the Galaxy

Galactic Region	Mass (log M$_\odot$)	Distance (kpc)	Name	Reference
Galactic Centre	4.1	8.5	Central Cluster	(5)
	4.0	8.5	Arches	(3)
	4.0	8.5	Quintuplet	(3)
G24	$\geq 4.2^*$	10.3	SFC 8	(1)
	$\geq 4.2^*$	6.1	SFC 10	(1)
	$\geq 4.3^*$	8.8†	SFC 12	(1)
G37	$\geq 3.9^*$	10.5	SFC 22	(1)
G43	~ 4	11.4	W49A	(2)
G80	4.4	1.5	Cygnus OB2	(8)
G287	>4.3	2.3	Carina	(7)
G291	4.2	6.0	NGC 3603	(4)
G298	5.0	9.7	Dragonfish	(6)
G332	$\geq 4.1^*$	3.2	SFC 34a,b	(1)
G337	$\geq 4.8^*$	10.9	SFC 37	(1)

*Candidate Cluster/Association from this work.

†Unresolved kinematic distance ambiguity. The distance indicated is the most consistent with the model extinction to the candidate.

References. — (1) *This work*; (2) Conti & Blum (2002); (3) Figer et al. (1999); (4) Harayama et al. (2008); (5) Paumard et al. (2006); (6) Chapter 3; (7) Smith & Brooks (2007); (8) Wright et al. (2010);

Note. — Wolff et al. (2007) use an IMF-sensitive extrapolation over a small mass range to determine the masses of IC 1805 and NGC 6611. The extrapolated mass of NGC 6611 is $10^{4.4}$ M$_\odot$, in contrast to more recent work by Bonatto et al. (2006) that revise the minimum cluster mass down to $10^{3.2}$ M$_\odot$. In both of these cases, the free-free luminosities of the regions from Murray & Rahman (2010) are inconsistent with young clusters with M$> 10^4$ M$_\odot$, indicating smaller masses. Consequently, we exclude both of these regions from this census.

5.8.2   Remaining Galactic Plane Targets

This work is based on the luminosity-selected sample of SFCs from Chapter 2 on the basis that their ionizing luminosities are from young, massive clusters hosted by the SFCs. However, this work was not a comprehensive search through the entire Galactic plane. We can determine the likely regions of young, massive clusters that remain hidden by comparing our census to the catalog of giant H II regions from Conti & Crowther (2004). As noted in Chapter 2, previously identified individual regions closely packed together are likely associated in larger complexes (see §2.1 in Chapter 2 for a detailed discussion). For the purpose of this comparison, we group the giant H II regions from Conti & Crowther (2004) into 27 degree-sized zones in the Galactic plane. Each Galactic plane zone consists of 1–7 giant H II regions.

Of the 27 Galactic plane zones, young massive ($\gtrsim 10^4$ M$_\odot$) clusters or associations have not been identified in 18. Within the 18 zones without young massive clusters, 6 have previously known powering clusters with masses less than 10^4 M$_\odot$, and 5 have candidates identified in this work also less than 10^4 M$_\odot$. We list the zones lacking a young, massive cluster in Table 5.4. For the 5 zones with candidates identified in this work, they have lower mass limits $> 10^{3.2}$ M$_\odot$. Because our search is not sensitive to the diffuse outskirts of clusters/associations, it is possible that the candidates in the 5 zones have masses larger than 10^4 M$_\odot$. Further observations and analysis are required to better constrain the total masses of these clusters.

Twelve of the 27 Galactic plane zones have not been probed in this work, leaving a substantial discovery space for the SSC method to be applied. Recently, Lee et al. (2012) have identified SFCs in the remaining WMAP free-free sources not originally covered in Chapter 2, which provides a new sample of morphologically-identified regions to probe. Investigating this remaining SFCs may enable the completion of the entire upper end of the Galactic CMF.

Table 5.4.   Giant H II Regions Lacking Known Young Massive Clusters

Galactic Region	Distance Components (kpc)	Names
G3	14.3, 14.6	AMWW34, AMWW35
G6[†]	2.8	M8
G8	13.5	...
G10[†]	4.5, 15	W31
G15[†]	2.4	M17
G20	11.8	...
G30[‡]	6.3	W43, SFC 17
G49[‡]	5.7	W51, SFC 25
G70	8.6	W58A
G133[†]	4.2	W3
G283[‡]	4.7,5.9, 8	RCW 49, SFC26
G274	6.4	RCW 42
G289	7.9	...
G305[†]	3.5	...
G320	11.5, 12.6	...
G327[‡]	3.6	RCW97, SFC 33
G347[†]	7.9	[DBS2003] 179
G351	13.7	...

[†]Regions with known powering clusters, but significantly less massive than 10^4 M$_\odot$

[‡]Regions with candidate powering clusters, but with minimum stellar masses less than 10^4 M$_\odot$

Note. — All regions and distance components are from Conti & Crowther (2004).

5.9   Conclusions

We have used the 2MASS point-source catalog to search for massive clusters and association candidates within the SFCs from WMAP, looking for the brightest stars, taking into account the line of sight extinction. Including the previous work of Chapter 3, we find that 22 of the 40 SFCs host a candidate cluster that has been identified through our method, either central to the SFC or on its periphery. The extracted candidates have semimajor axes of $3' - 26'$. The average extraction significance of the candidates is 2.4. The candidates with smaller extraction significances are selected based primarily on morphology.

We discuss the case of two previously identified clusters/associations: NGC 3603, which is unidentified through our method due to the compact nature of the cluster, and Cygnus OB2, which we readily identify and whose properties we accurately constrain. We find the false positive rate to be 3.0 ± 0.6 out of 22 identified. The strong correlation between the candidate extinctions and the modelled extinction based on the SFC distances provides strong support for the reality of the clusters. This is reinforced by the spectroscopic confirmation of the Dragonfish Association (Chapter 4), originally identified with the method of Chapter 3.

We estimate the masses and luminosities of the candidates, showing that the candidates can account for the observed WMAP free-free flux for most of the investigated sources. Of the WMAP sources investigated, only one (G10) lacks any candidate clusters or associations. Finally, we produce the Galactic census of the young, massive clusters and OB associations. With the newly identified candidates from this work, we estimate that we are likely within a factor of two to complete the young massive cluster population. We indicate locations on the Galactic plane possibly hosting the remaining unidentified massive clusters and associations.

Future astrometric, spectroscopic and/or X-ray follow-up observations can confirm the candidates, measure their physical properties and determine their environmental

impact. With such confirmation, the candidate clusters and associations within the most luminous SFCs in the Galaxy will enable the more accurate determination of the upper end of the Galactic CMF.

Chapter 6

Conclusions & Future Work

6.1 Conclusions

Over the course of this thesis, we have sought to identify and characterize the Milky Way's most luminous star clusters. Initially, we identify them through their environmental signatures of gas morphology and reprocessed emission. Subsequently, we seek to identify their massive stellar populations directly. It is through this process that we substantially increase the number of young, massive star clusters known in the Galaxy and better characterize the upper end of the Galactic cluster mass function.

In Chapter 2, we use data from Spitzer GLIMPSE and radio recombination line surveys to identify SFCs within the 13 most luminous WMAP free-free emission sources in the Galaxy. On the basis of morphology from the 8 μm emission and radial velocities from radio recombination lines, we identify 40 SFCs, some of which are expected to contain young clusters or OB associations with masses greater than 10^4 M$_\odot$. Based on the locations of the SFCs, we estimate that the scale height of Galactic O-type stars to be 35 ± 5 pc, consistent with previous values. With the free-free emission measurements from WMAP and the 8 μm emission measurements from Spitzer GLIMPSE, we find a nearly linear relationship between the two integrated over the area of the WMAP sources. Having estimated the expansion velocity of the

bubbles associated with the SFCs, we show that the mechanical luminosity from the expansion of bubbles accounting for one-third of the Galaxy's star formation can account for approximately one-third of the luminosity require to maintain the velocity dispersion of the molecular gas inside the solar circle, suggesting that the expansion of bubbles surrounding the most luminous star clusters and OB associations is likely sufficient to support the observed turbulence of the molecular gas disk. Further, we show that the kinetic energy of some of the largest bubbles in the sample is similar to those of previously known superbubbles, likely prior to a single supernova taking place, indicating that some of these bubbles are progenitors of the superbubbles. Finally, based on statistical arguments of projection, we show that the observed shell structure in the 8 μm morphology is more consistent with the hypothesis of limb brightened shells rather than flattened rings.

In Chapter 3, we search for the powering stellar population of the most luminous SFC identified in Chapter 2, the Dragonfish Nebula. We use the 2MASS point source catalog to identify candidate O-type stars consistent with the distance and extinction of the Dragonfish Nebula, using colour cuts around the expected extinction to filter out most line-of-sight contaminating stars. Based on the size and demographics of the overdensity, we classify it as a candidate OB association. We find a significant overdensity of point sources with extinction between $0.96 < A_K < 1.2$ towards the centre of the SFC. Subtracting the contribution of field sources, we find 406 ± 102 sources in the candidate association appearing as O- and early B-type stars at the distance of the association, consistent with the expected population based on its total ionizing luminosity. Based on the ionizing luminosity and point source demographics, we find that the candidate OB association is likely the most luminous OB association known in the Galaxy.

In Chapter 4, we seek to confirm the existence of the Dragonfish Association, identified in Chapter 3. We take NIR spectroscopy of a sample of possible O-stars

in the candidate Dragonfish Association in the *H*- and *K*-bands using the SOFI spectrograph on the NTT 3.6m telescope in La Silla, Chile. With the identification of Brackett-series hydrogen and helium absorption lines, we find that 15 of the 50 stars identified are O-type stars. In addition, we identify a late-type WN star through hydrogen line emission, and two LBV candidates using helium and forbidden iron line emission. Based on the population statistics, we confirm the existence of the Dragonfish association and its estimated ionizing luminosity and stellar mass, inferring the existence of a low-mass association population from the stellar initial mass function. In addition to the confirmation of the association, the spectroscopy validates the method developed in Chapter 3 and adds evidence to the candidate associations/clusters identified through it.

In Chapter 5, we refine the method of Chapter 3 to apply to the remaining SFCs from Chapter 2. Including the Dragonfish association from Chapter 3, we find that 22 of the 40 SFCs host candidate clusters, either central to the SFC or on its periphery. We constrain the false positive rate of the candidates to be 3.0 ± 0.6, and we find that the candidates have a strong correlation between their measured extinction and the modeled extinction based on the distance of their host SFC. These two lines of evidence, added with the confirmation of the Dragonfish Association from Chapter 4, indicate the reality of the candidates identified. We estimate the masses and luminosity of the candidates, showing that the candidates can account for the observed WMAP free-free flux for most of the investigated sources. We, finally, produce the census of the Galactic OB associations and clusters with ages < 4 Myrs and masses $> 10^4$ M$_\odot$, showing that with this work, we have doubled the number of such known clusters. Based on extragalactic estimates, we estimate that the census is now within a factor of two to completion and we indicate the locations on the Galactic plane that may likely host the remaining young, massive OB associations and stellar clusters.

To summarize, in this thesis we have found some of the most luminous (and

massive) young OB associations and clusters in the Galaxy.

6.2 Future Work and Directions

With the identification and characterization of a large new sample of young, massive clusters and OB associations from this thesis, there is a plethora of different avenues of future work and investigation. We summarize a number of these directions and classify them into two overarching categories: characterizing the stellar populations themselves and characterizing their energetic feedback into the Galactic disk and halo.

6.2.1 Characterization of Stellar Populations

While the locations for a large number of new massive clusters and OB associations have been determined in this thesis, very little has been determined about their stellar population. Even their very reality requires independent confirmation with additional evidence beyond statistical stellar density arguments. We outline a number of alternative means to confirm the existence of the clusters and determine the composition and distribution of the stellar members.

Spectroscopic Follow-up

As was conducted in Chapter 4 for the Dragonfish Association, follow-up spectroscopy on individual candidate cluster members will enable precise spectroscopic typing of the stars. Since these clusters are located at large (> 2 kpc) distances within the Galactic disk, extinction becomes a substantial problem; while the spectroscopic typing of massive stars is best conducted in the optical bands, this is likely only possible for the nearest clusters/associations with relatively low extinction. For the most deeply-veiled clusters/associations, the line-of-sight extinction may only permit spectroscopy in the NIR bands, where the spectra of an O-type star is nearly featureless (Gray &

Corbally 2009). To further complicate matters, the spectral features due to interstellar absorption are similar to the depth of the features intrinsic to the spectra (Chapter 4).

While the advent of NIR multi-object spectrographs will enable greater numbers of stars to be tested at a time, direct spectroscopy of stars is inherently a low yield technique for highly confused clusters/associations. In many of the cases from Chapter 5, the ratio of cluster stars to confusing sources along the line of sight is worse than 1:1 after the colour-selection criteria are applied. Additionally, many of these candidates have $\sim 10^3$ OB stars identified in 2MASS, requiring substantial effort and telescope time to fully classify every identified cluster candidate.

However, despite these challenges, direct spectroscopic follow-up of candidate cluster stars provides a simple, robust determination of the reality of the candidate cluster/OB association. Spectroscopic observations also allow the identification of the exotic, evolved massive star phases, such as the Wolf-Rayet and luminous blue variable phases (Chapter 4). The identification of these short lived states and their population statistics may in the future lead to robust estimates of the age of the cluster or association.

Point Source X-ray Observations

Over the past decade, the *Chandra X-ray Observatory* has been beneficial for the characterization of young, massive stellar clusters and OB associations (Moffat et al. 2002; Wang et al. 2008). Recently, the detailed work of Townsley et al. (2011a) for the Carina region has highlighted the advantages of using the X-ray regime to characterize massive stellar populations through X-ray emitting OB stars and colliding-wind binaries. The relatively large ($\sim 1/3°$) field-of-view permits even some of the widest OB associations to be observed at once. In the case of the Carina region, this has lead to the discovery of a large, diffuse population of OB stars outside the dense clusters (Povich et al. 2011b).

In addition to the X-ray emitting OB stars, the high energy regime enables the detection of the flaring intermediate-mass pre-main sequence stellar population (Povich et al. 2011a). The detection of this population is unique to the X-ray regime as these sources would be too faint to observe in the optical or infrared wavelengths.

However, the challenge of X-ray observations include the extremely long exposure times required to obtain sufficient sensitivity to the X-ray emitting sources in the clusters with large distances and extinguishing columns ($\sim 10^2$ ks). Further, there is a limited number of facilities capable of making such observations (~ 1).

Astrometric Observations

Precision (near microarcsecond) astrometry enabled through space-based facilities such as the *Hubble Space Telescope* and ground-based multi-conjugate adaptive optics is allowing the separation of cluster and contaminating sources on the basis of relative proper motions. This process has been successfully conducted on NGC 3603 (Rochau et al. 2010). This technique provides an entirely unbiased sampling of all objects in the field, enabling the identification of cluster members that would be otherwise excluded by colour cuts or chance X-ray emission processes. However, the large distances to the clusters/associations require multi-year epochs of observation to provide sufficient proper motion sensitivity to separate cluster and contaminant sources.

6.2.2   Characterization of Feedback

Studying the energetic feedback processes of young, massive clusters and associations into their environment requires knowledge of both the powering stellar population and its energetic output. We have discussed avenues to characterize the stellar populations above. The energetic output can be measured through reprocessed emission, possibly coming from the winds or ionizing photons produced, or the kinematics and morphology of the region being acted upon. This new population

of young, massive clusters and associations is well suited for studies of energetic feedback; the complexes were initially identified through their reprocessed emission and morphology, meaning that their large scale structure beyond the position of individual stars is established. We outline possible directions for feedback studies using these associations.

Molecular Mapping

Mapping the SFCs and their surrounding natal clouds with a molecular tracer, such as ^{12}CO, will enable studies of the feedback of these clusters/associations into their natal GMCs. We are in the midst of conducting such a study of the Dragonfish Nebula currently, using data obtained with the Mopra Observatory in Australia. While CO surveys of the Galactic Plane do exist (Dame et al. 2001), they tend to have relatively low ($\sim 1/8°$) angular resolution, insufficient to resolve the structure caused by feedback effects. Sub-arcminute, wide field ($\gtrsim 1°$) CO surveys surrounding the SFCs will enable investigations into the driving of large scale structure into the GMC, the cascading of turbulence in the molecular gas, and the kinematics of GMC destruction. These observations will help connect the evolution of young, massive clusters to the life cycle of a GMC in a detailed manner.

Diffuse Emission X-ray Observations

Beyond characterizing stellar populations (as noted in §6.2.1), X-ray observations are uniquely capable of measuring the hot gas originating from stellar winds (Townsley et al. 2011b). The diffuse X-ray emission can be extracted using long (> 60 ks) exposures, binned over arcminute-sized zones, removing the coincident X-ray point sources. Measuring the diffuse hot gas through X-rays enables a direct measure of the cluster's wind feedback and energetics. From these measurements, we can determine the total pressure contributed by the hot winds into the bubble inflated by the central

cluster. This will enable the direct determination of the driving of energetic feedback into the ambient medium.

Bibliography

Allamandola, L. J., Tielens, A. G. G. M., & Barker, J. R. 1989, ApJS, 71, 733

Ambartsumian, V. A. 1947, Stellar Evolution and Astrophysics

—. 1954, Memoires of the Societe Royale des Sciences de Liege, 1, 293

Anantharamaiah, K. R. 1985a, Journal of Astrophysics and Astronomy, 6, 177

—. 1985b, Journal of Astrophysics and Astronomy, 6, 203

Andersen, J. 1991, A&A Rev., 3, 91

Ascenso, J., Alves, J., Beletsky, Y., & Lago, M. T. V. T. 2007, A&A, 466, 137

Avedisova, V. S. 1972, Soviet Ast., 15, 708

Bains, I., et al. 2006, MNRAS, 367, 1609

Barbosa, C. L., Damineli, A., Blum, R. D., & Conti, P. S. 2003, AJ, 126, 2411

Beaumont, C. N., & Williams, J. P. 2010, ApJ, 709, 791

Benjamin, R. A., et al. 2003, PASP, 115, 953

—. 2005, ApJ, 630, L149

Bennett, C. L., et al. 2003, ApJS, 148, 97

Bica, E., & Bonatto, C. 2011, A&A, 530, A32+

Bica, E., Dutra, C. M., Soares, J., & Barbuy, B. 2003, A&A, 404, 223

Binney, J., & Merrifield, M. 1998, Galactic astronomy, ed. Binney, J. & Merrifield, M.

Blaauw, A. 1964, ARA&A, 2, 213

Black, J. H., & Willner, S. P. 1984, ApJ, 279, 673

Blum, R. D., Conti, P. S., & Damineli, A. 2000, AJ, 119, 1860

Blum, R. D., Damineli, A., & Conti, P. S. 1999, AJ, 117, 1392

Bonatto, C., Santos, Jr., J. F. C., & Bica, E. 2006, A&A, 445, 567

Borissova, J., Ivanov, V. D., Minniti, D., Geisler, D., & Stephens, A. W. 2005, A&A, 435, 95

Brandner, W., Clark, J. S., Stolte, A., Waters, R., Negueruela, I., & Goodwin, S. P. 2008, A&A, 478, 137

Bressan, A., Fagotto, F., Bertelli, G., & Chiosi, C. 1993, A&AS, 100, 647

Bronfman, L., Nyman, L., & May, J. 1996, A&AS, 115, 81

Calzetti, D., et al. 2007, ApJ, 666, 870

Cardelli, J. A., Clayton, G. C., & Mathis, J. S. 1989, ApJ, 345, 245

Casertano, S., & Hut, P. 1985, ApJ, 298, 80

Castor, J., McCray, R., & Weaver, R. 1975, ApJ, 200, L107

Caswell, J. L. 1972, Australian Journal of Physics, 25, 443

Caswell, J. L., & Haynes, R. F. 1987, A&A, 171, 261

Caswell, J. L., Murray, J. D., Roger, R. S., Cole, D. J., & Cooke, D. J. 1975, A&A, 45, 239

Chabrier, G. 2003, PASP, 115, 763

Chandar, R., et al. 2010, ApJ, 719, 966

Chapin, S. L. 1957, Isis, 48, pp. 13

Chevalier, R. A. 1974, ApJ, 188, 501

Chomiuk, L., & Povich, M. S. 2011, AJ, 142, 197

Chu, Y.-H. 2008, in IAU Symposium, Vol. 250, IAU Symposium, ed. F. Bresolin, P. A. Crowther, & J. Puls, 341–354

Churchwell, E., Walmsley, C. M., & Cesaroni, R. 1990, A&AS, 83, 119

Churchwell, E., et al. 2006, ApJ, 649, 759

Clark, J. S., Negueruela, I., Crowther, P. A., & Goodwin, S. P. 2005, A&A, 434, 949

Clark, J. S., et al. 2009, A&A, 498, 109

Clemens, D. P. 1985, ApJ, 295, 422

Cohen, M., & Green, A. J. 2001, MNRAS, 325, 531

Comerón, F., & Pasquali, A. 2007, A&A, 467, L23

Comerón, F., Pasquali, A., Figueras, F., & Torra, J. 2008, A&A, 486, 453

Conti, P. S., & Blum, R. D. 2002, ApJ, 564, 827

Conti, P. S., & Crowther, P. A. 2004, MNRAS, 355, 899

Corbel, S., & Eikenberry, S. S. 2004, A&A, 419, 191

Corbel, S., Wallyn, P., Dame, T. M., Durouchoux, P., Mahoney, W. A., Vilhu, O., & Grindlay, J. E. 1997, ApJ, 478, 624

Dame, T. M., Hartmann, D., & Thaddeus, P. 2001, ApJ, 547, 792

Davies, B., Figer, D. F., Kudritzki, R., MacKenty, J., Najarro, F., & Herrero, A. 2007, ApJ, 671, 781

de Grijs, R., Anders, P., Bastian, N., Lynds, R., Lamers, H. J. G. L. M., & O'Neil, E. J. 2003, MNRAS, 343, 1285

Deharveng, L., & Maucherat, M. 1974, A&A, 34, 465

Dove, J. B., Shull, J. M., & Ferrara, A. 2000, ApJ, 531, 846

Downes, D., Wilson, T. L., Bieging, J., & Wink, J. 1980, A&AS, 40, 379

Dupree, A. K., & Goldberg, L. 1970, ARA&A, 8, 231

Dutra, C. M., Bica, E., Soares, J., & Barbuy, B. 2003, A&A, 400, 533

Dye, S., et al. 2006, MNRAS, 372, 1227

Eikenberry, S. S., et al. 2004, ApJ, 616, 506

Elias, F., Cabrera-Caño, J., & Alfaro, E. J. 2006, AJ, 131, 2700

Elmegreen, B. G. 1998, in Astronomical Society of the Pacific Conference Series, Vol. 148, Origins, ed. C. E. Woodward, J. M. Shull, & H. A. Thronson Jr., 150–+

Epchtein, N., et al. 1994, Ap&SS, 217, 3

Evans, C. J., et al. 2011, A&A, 530, A108

Fall, S. M., Chandar, R., & Whitmore, B. C. 2009, ApJ, 704, 453

Fall, S. M., Krumholz, M. R., & Matzner, C. D. 2010, ApJ, 710, L142

Figer, D. F. 2008, in IAU Symposium, Vol. 250, IAU Symposium, ed. F. Bresolin, P. A. Crowther, & J. Puls, 247–256

Figer, D. F., Kim, S. S., Morris, M., Serabyn, E., Rich, R. M., & McLean, I. S. 1999, ApJ, 525, 750

Figer, D. F., MacKenty, J. W., Robberto, M., Smith, K., Najarro, F., Kudritzki, R. P., & Herrero, A. 2006, ApJ, 643, 1166

Figuerêdo, E., Blum, R. D., Damineli, A., Conti, P. S., & Barbosa, C. L. 2008, AJ, 136, 221

Fodera-Serio, G., Indorato, L., & Nastasi, P. 1985, Journal for the History of Astronomy, 16, 1

Froebrich, D., Scholz, A., & Raftery, C. L. 2007, MNRAS, 374, 399

Galilei, G. 1610, Siderevs nvncivs,: magna longeqve admirabilia spectacula pandens ... quae a Galileo Galileo ... sunt obseruata in lunae facie ... apprime vero in qvatvor planetis circa Iovis stellam disparibus interuallis ... quos ... nouissime auctor deprehendit primus; atque medicea sidera nvncvpandos decrevit. (Francof[vrti]|bProstat in Paltheniano,|c1610.: Prostat in Paltheniano)

Gardner, F. F., & Whiteoak, J. B. 1978, MNRAS, 183, 711

Georgelin, Y. P., & Georgelin, Y. M. 1970, A&A, 7, 133

Gieles, M., & Portegies Zwart, S. F. 2011, MNRAS, 410, L6

Gold, B., et al. 2009, ApJS, 180, 265

Goldbaum, N. J., Krumholz, M. R., Matzner, C. D., & McKee, C. F. 2011, ApJ, 738, 101

Grabelsky, D. A., Cohen, R. S., Bronfman, L., & Thaddeus, P. 1988, ApJ, 331, 181

Gray, R. O., & Corbally, C. J. 2009, Stellar Spectral Classification, Princeton series in astrophysics (Princeton, NJ: Princeton Univ. Press)

Gvaramadze, V. V., Gualandris, A., & Portegies Zwart, S. 2008, MNRAS, 385, 929

Hanson, M. M., & Bubnick, B. F. 2008, PASP, 120, 150

Hanson, M. M., Kudritzki, R.-P., Kenworthy, M. A., Puls, J., & Tokunaga, A. T. 2005, ApJS, 161, 154

Hanson, M. M., & Popescu, B. 2008, in IAU Symposium, Vol. 250, IAU Symposium, ed. F. Bresolin, P. A. Crowther, & J. Puls, 307–312

Harayama, Y., Eisenhauer, F., & Martins, F. 2008, ApJ, 675, 1319

Harper-Clark, E., & Murray, N. 2009, ApJ, 693, 1696

Heiles, C. 1979, ApJ, 229, 533

Herschel, W. 1786, Royal Society of London Philosophical Transactions Series I, 76, 457

Ho, L. C. 1997, in Revista Mexicana de Astronomia y Astrofisica Conference Series, Vol. 6, Revista Mexicana de Astronomia y Astrofisica Conference Series, ed. J. Franco, R. Terlevich, & A. Serrano, 5–+

Hodierna, G. B. 1656, De admirandis phasibus in sole, et luna visis, ponderationes: opticae, physicae, et astronomicae : in quaestiones incidentes : inter obseruandum solis eclypsim Romae, anno domini M.DC.LVI. die XXVI. Ianuarij, ho: II. min. XXXV. p.m., seu, Dissertationum respontiones (Panormi: Typis Nicolai Bua)

Hoglund, B., & Mezger, P. G. 1965, Science, 150, 339

Hollenbach, D. J., & Tielens, A. G. G. M. 1997, ARA&A, 35, 179

Hunter, J. D. 2007, Computing In Science & Engineering, 9, 90

Ikeda, M., Ohishi, M., Nummelin, A., Dickens, J. E., Bergman, P., Hjalmarson, Å., & Irvine, W. M. 2001, ApJ, 560, 792

Indebetouw, R., et al. 2005, ApJ, 619, 931

Ivanov, V. D., Borissova, J., Bresolin, F., & Pessev, P. 2005, A&A, 435, 107

Ivanov, V. D., Messineo, M., Zhu, Q., Figer, D., Borissova, J., Kurtev, R., & Ivanov, G. R.
2010, in IAU Symposium, Vol. 266, IAU Symposium, ed. R. de Grijs & J. R. D. Lépine,
203–210

Kang, M., Bieging, J. H., Povich, M. S., & Lee, Y. 2009, ApJ, 706, 83

Kardashev, N. S. 1959, Soviet Ast., 3, 813

Kennicutt, Jr., R. C. 1998, ARA&A, 36, 189

Kennicutt, Jr., R. C., Edgar, B. K., & Hodge, P. W. 1989, ApJ, 337, 761

Kessler, M. F., et al. 1996, A&A, 315, L27

Kim, K., & Koo, B. 2001, ApJ, 549, 979

—. 2002, ApJ, 575, 327

Knödlseder, J. 2000, A&A, 360, 539

Kolpak, M. A., Jackson, J. M., Bania, T. M., Clemens, D. P., & Dickey, J. M. 2003, ApJ,
582, 756

Kroupa, P. 2001, MNRAS, 322, 231

Krumholz, M. R., & Matzner, C. D. 2009, ApJ, 703, 1352

Kuchar, T. A., & Bania, T. M. 1994, ApJ, 436, 117

Kulkarni, S. R., & Frail, D. A. 1993, Nature, 365, 33

Lacy, J. H., Knacke, R., Geballe, T. R., & Tokunaga, A. T. 1994, ApJ, 428, L69

Lada, C. J., & Lada, E. A. 2003, ARA&A, 41, 57

Lada, C. J., Lombardi, M., & Alves, J. F. 2010, ApJ, 724, 687

Lancon, A., & Rocca-Volmerange, B. 1992, A&AS, 96, 593

Langer, N., Hamann, W.-R., Lennon, M., Najarro, F., Pauldrach, A. W. A., & Puls, J. 1994, A&A, 290, 819

Larsen, S. S. 2009, A&A, 494, 539

Larsen, S. S., & Richtler, T. 2000, A&A, 354, 836

Leahy, D. A., & Tian, W. W. 2008, AJ, 135, 167

Lee, E. J., Murray, N., & Rahman, M. 2012, ArXiv e-prints

Lemiere, A., Slane, P., Gaensler, B. M., & Murray, S. 2009, ApJ, 706, 1269

Lester, D. F., Dinerstein, H. L., Werner, M. W., Harvey, P. M., Evans, II, N. J., & Brown, R. L. 1985, ApJ, 296, 565

Lockman, F. J. 1976, ApJ, 209, 429

—. 1989, ApJS, 71, 469

Lockman, F. J., Pisano, D. J., & Howard, G. J. 1996, ApJ, 472, 173

Lopez, L. A., Krumholz, M. R., Bolatto, A. D., Prochaska, J. X., & Ramirez-Ruiz, E. 2011, ApJ, 731, 91

López-Corredoira, M., Cabrera-Lavers, A., Garzón, F., & Hammersley, P. L. 2002, A&A, 394, 883

Mac Low, M., & Klessen, R. S. 2004, Reviews of Modern Physics, 76, 125

Mac Low, M., Klessen, R. S., Burkert, A., & Smith, M. D. 1998, Physical Review Letters, 80, 2754

Malhotra, S. 1994, ApJ, 433, 687

Marshall, D. J., Robin, A. C., Reylé, C., Schultheis, M., & Picaud, S. 2006, A&A, 453, 635

Martins, F., & Plez, B. 2006, A&A, 457, 637

Martins, F., Schaerer, D., & Hillier, D. J. 2005, A&A, 436, 1049

Matzner, C. D. 2002, ApJ, 566, 302

—. 2007, ApJ, 659, 1394

McKee, C. F., & Ostriker, J. P. 1977, ApJ, 218, 148

McKee, C. F., & Williams, J. P. 1997, ApJ, 476, 144

McKee, C. F., & Zweibel, E. G. 1992, ApJ, 399, 551

Melena, N. W., Massey, P., Morrell, N. I., & Zangari, A. M. 2008, AJ, 135, 878

Mercer, E. P., et al. 2005, ApJ, 635, 560

Messier, M. 1771, Mémoires de l'Académie Royale des Sciences, 435

Mezger, P. G., & Henderson, A. P. 1967, ApJ, 147, 471

Mezger, P. G., & Hoglund, B. 1967, ApJ, 147, 490

Michell, J. 1767, Royal Society of London Philosophical Transactions Series I, 57, 234

Miesch, M. S., & Bally, J. 1994, ApJ, 429, 645

Miller, G. E., & Scalo, J. M. 1978, PASP, 90, 506

Milne, D. K. 1979, Australian Journal of Physics, 32, 83

Minier, V., et al. 2009, A&A, 501, L1

Moffat, A. F. J., et al. 2002, ApJ, 573, 191

Morris, P. W., Eenens, P. R. J., Hanson, M. M., Conti, P. S., & Blum, R. D. 1996, ApJ, 470, 597

Motte, F., Schilke, P., & Lis, D. C. 2003, ApJ, 582, 277

Muench, A. A., Lada, E. A., Lada, C. J., & Alves, J. 2002, ApJ, 573, 366

Murray, N. 2011, ApJ, 729, 133

Murray, N., Quataert, E., & Thompson, T. A. 2010, ApJ, 709, 191

Murray, N., & Rahman, M. 2010, ApJ, 709, 424

Nakanishi, H., & Sofue, Y. 2006, PASJ, 58, 847

Neugebauer, G., & Leighton, R. B. 1969, Two-micron sky survey. A preliminary catalogue

Nishiyama, S., Nagata, T., Tamura, M., Kandori, R., Hatano, H., Sato, S., & Sugitani, K. 2008, ApJ, 680, 1174

Nishiyama, S., Tamura, M., Hatano, H., Kato, D., Tanabé, T., Sugitani, K., & Nagata, T. 2009, ApJ, 696, 1407

Norman, C., & Silk, J. 1980, ApJ, 238, 158

Noumeir, R. 1999, Pattern Recognition Letters, 20, 585

Olmi, L., Cesaroni, R., Hofner, P., Kurtz, S., Churchwell, E., & Walmsley, C. M. 2003, A&A, 407, 225

Oort, J. H. 1954, Bull. Astron. Inst. Netherlands, 12, 177

Palagi, F., Cesaroni, R., Comoretto, G., Felli, M., & Natale, V. 1993, A&AS, 101, 153

Parker, J. W., & Garmany, C. D. 1993, AJ, 106, 1471

Paumard, T., et al. 2006, ApJ, 643, 1011

Persi, P., Roth, M., Tapia, M., Ferrari-Toniolo, M., & Marenzi, A. R. 1994, A&A, 282, 474

Pestalozzi, M. R., Minier, V., & Booth, R. S. 2005, A&A, 432, 737

Pickles, A. J. 1998, PASP, 110, 863

Piskunov, A. E., Kharchenko, N. V., Schilbach, E., Röser, S., Scholz, R.-D., & Zinnecker, H. 2008, A&A, 487, 557

Portegies Zwart, S. F., McMillan, S. L. W., & Gieles, M. 2010, ARA&A, 48, 431

Povich, M. S., et al. 2007, ApJ, 660, 346

—. 2011a, ApJS, 194, 14

—. 2011b, ApJS, 194, 6

Pratap, P., Megeath, S. T., & Bergin, E. A. 1999, ApJ, 517, 799

Price, S. D., Egan, M. P., Carey, S. J., Mizuno, D. R., & Kuchar, T. A. 2001, AJ, 121, 2819

Puls, J., et al. 1996, A&A, 305, 171

Quireza, C., Rood, R. T., Balser, D. S., & Bania, T. M. 2006, ApJS, 165, 338

Rahman, M., Matzner, C., & Moon, D.-S. 2011a, ApJ, 728, L37

Rahman, M., Moon, D.-S., & Matzner, C. D. 2011b, ApJ, 743, L28

Rahman, M., & Murray, N. 2010, ApJ, 719, 1104

Rayner, J. T., Cushing, M. C., & Vacca, W. D. 2009, ApJS, 185, 289

Redfield, S., & Linsky, J. L. 2004, ApJ, 613, 1004

Reed, B. C. 2000, AJ, 120, 314

Reid, M. J., & Ho, P. T. P. 1985, ApJ, 288, L17

Roberts, M. S. 1957, PASP, 69, 59

Robin, A. C., Reylé, C., Derrière, S., & Picaud, S. 2003, A&A, 409, 523

—. 2004, A&A, 416, 157

Robitaille, T. P., & Whitney, B. A. 2010, ApJ, 710, L11

Rochau, B., Brandner, W., Stolte, A., Gennaro, M., Gouliermis, D., Da Rio, N., Dzyurke-vich, N., & Henning, T. 2010, ApJ, 716, L90

Rodríguez-Rico, C. A., Rodríguez, L. F., & Gómez, Y. 2002, Revista Mexicana de Astronomia y Astrofisica, 38, 3

Russeil, D. 2003, A&A, 397, 133

Russeil, D., Adami, C., Amram, P., Le Coarer, E., Georgelin, Y. M., Marcelin, M., & Parker, Q. 2005, A&A, 429, 497

Saito, R. K., et al. 2012, A&A, 537, A107

Salpeter, E. E. 1955, ApJ, 121, 161

Sewilo, M., Watson, C., Araya, E., Churchwell, E., Hofner, P., & Kurtz, S. 2004, ApJS, 154, 553

Skrutskie, M. F., et al. 2006, AJ, 131, 1163

Smith, L. F., Biermann, P., & Mezger, P. G. 1978, A&A, 66, 65

Smith, N., & Brooks, K. J. 2007, MNRAS, 379, 1279

Smith, T. R., & Kennicutt, Jr., R. C. 1989, PASP, 101, 649

Soares, J. B., Bica, E., Ahumada, A. V., & Clariá, J. J. 2008, A&A, 478, 419

Solomon, P. M., Rivolo, A. R., Barrett, J., & Yahil, A. 1987, ApJ, 319, 730

Stead, J. J., & Hoare, M. G. 2009, MNRAS, 400, 731

Stolte, A., Brandner, W., Brandl, B., Zinnecker, H., & Grebel, E. K. 2004, AJ, 128, 765

Strömgren, B. 1939, ApJ, 89, 526

Struve, O., & Elvey, C. T. 1938, ApJ, 88, 364

Townsley, L. K., et al. 2011a, ApJS, 194, 1

—. 2011b, ApJS, 194, 15

Tsujimoto, M., et al. 2007, ApJ, 665, 719

van den Bergh, S. 1978, ApJS, 38, 119

van Kerkwijk, M. H., Kulkarni, S. R., Matthews, K., & Neugebauer, G. 1995, ApJ, 444, L33

Vasisht, G., Frail, D. A., & Kulkarni, S. R. 1995, ApJ, 440, L65

Vázquez-Semadeni, E. 2011, in IAU Symposium, Vol. 270, Computational Star Formation, ed. J. Alves, B. G. Elmegreen, J. M. Girart, & V. Trimble, 275–282

Voit, G. M. 1992, MNRAS, 258, 841

Walsh, A. J., Hyland, A. R., Robinson, G., & Burton, M. G. 1997, MNRAS, 291, 261

Wang, J., Townsley, L. K., Feigelson, E. D., Broos, P. S., Getman, K. V., Román-Zúñiga, C. G., & Lada, E. 2008, ApJ, 675, 464

Weidner, C., Kroupa, P., & Bonnell, I. A. D. 2010, MNRAS, 401, 275

Westerhout, G. 1958, Bull. Astron. Inst. Netherlands, 14, 215

Whitmore, B. C., Chandar, R., & Fall, S. M. 2007, AJ, 133, 1067

Wilson, T. L., Mezger, P. G., Gardner, F. F., & Milne, D. K. 1970, A&A, 6, 364

Wink, J. E., Altenhoff, W. J., & Mezger, P. G. 1982, A&A, 108, 227

Wink, J. E., Wilson, T. L., & Bieging, J. H. 1983, A&A, 127, 211

Wolff, S. C., Strom, S. E., Dror, D., & Venn, K. 2007, AJ, 133, 1092

Wood, D. O. S., & Churchwell, E. 1989, ApJS, 69, 831

Wright, N. J., Drake, J. J., Drew, J. E., & Vink, J. S. 2010, ApJ, 713, 871

Wyrowski, F., Menten, K. M., Schilke, P., Thorwirth, S., Güsten, R., & Bergman, P. 2006, A&A, 454, L91

Xu, Y., Reid, M. J., Menten, K. M., Brunthaler, A., Zheng, X. W., & Moscadelli, L. 2009, ApJ, 693, 413

Zinnecker, H., & Yorke, H. W. 2007, ARA&A, 45, 481

Zuckerman, B., & Evans, II, N. J. 1974, ApJ, 192, L149